



**Electrochemical preparation of nano/micron structure
transition metal-based catalysts for the oxygen evolution
reaction**

Journal:	<i>Materials Horizons</i>
Manuscript ID	MH-REV-01-2022-000075.R1
Article Type:	Review Article
Date Submitted by the Author:	09-Mar-2022
Complete List of Authors:	Li, Huixi; China University of Geosciences Han, Xue; China University of Geosciences Zhao, Wen; China University of Geosciences Azhar , Alowasheer; NIMS Jeong, Seunghwan; Green Energy Institute, R&D Division Jeong, Deugyoung; Green Energy Institute, R&D Division Na, Jongbeom; University of Queensland, Australian Institute for Bioengineering and Nanotechnology; Green Energy Institute, R&D Division Wang, Shengping; China University of Geosciences, Faculty of Materials Science and Chemistry Yu, Jingxian; University of Adelaide, Yamauchi, Yusuke; University of Queensland, School of Chem Eng and AIBN

REVIEW

Electrochemical preparation of nano/micron structure transition metal-based catalysts for the oxygen evolution reaction

Received 00th January 20xx,
Accepted 00th January 20xx

DOI: 10.1039/x0xx00000x

Huixi Li,^{a†} Xue Han,^{a†} Wen Zhao,^a Alowasheer Azhar,^b Seunghwan Jeong,^c Deugyoung Jeong,^c Jongbeom Na,^{*c,d} Shengping Wang,^{*a} Jingxian Yu,^{*e} Yusuke Yamauchi^{b,d}

Electrochemical water splitting is a promising technology for hydrogen production and sustainable energy conversion, but the existing electrolytic cells lack a sufficient number of robust and highly active anodic electrodes for the oxygen evolution reaction (OER). Electrochemical synthesis technology provides a feasible route for the preparation of independent OER electrodes with high utilization of active sites, fast mass transfer, and a simple preparation process. A comprehensive review of the electrochemical synthesis of nano/microstructure transition metal-based OER materials is provided. First, some fundamentals of electrochemical synthesis are introduced, including electrochemical synthesis strategies, electrochemical synthesis substrates, the electrolyte used in electrochemical synthesis, and the combination of electrochemical synthesis and other synthesis methods. Second, the morphology and properties of electrochemical synthetic materials are summarized and introduced from the viewpoint of structural design. Then, the latest progress regarding the development of transition metal-based OER electrocatalysts is reviewed, including the classification of metals/alloys, oxides, hydroxides, sulfides, phosphides, selenides, and other transition metal compounds. In addition, the oxygen evolution mechanism and rate-determining steps of transition metal-based catalysts are also discussed. Finally, the advantages, challenges, and opportunities regarding the application of electrochemical techniques in the synthesis of transition metal-based OER electrocatalysts are summarized. This review can provide inspiration for researchers and promote the development of water splitting technology.

1. Introduction

With the increasing global energy demand and increasingly serious environmental problems, great attention has been given to the development of sustainable energy conversion and storage devices that attain high performance and environmental compatibility at a low cost. Hydrogen is considered a promising substitute for energy and fossil fuels because of its high mass specific energy density^{1–4}. Electrochemical water splitting provides a promising way for hydrogen production. At the same time, it stores intermittent energy in the form of chemical energy, such as solar and wind energy^{5,6}. This green route allows the production of high purity hydrogen with almost zero carbon emissions. However, the slow kinetics of the multielectron oxygen evolution reaction (OER) in water splitting is

the greatest obstacle to hydrogen production^{7–9}. The equilibrium potential of oxygen evolution is as high as 1.23 V (vs. that of a reversible hydrogen electrode (RHE)). Under the condition of a high overpotential of the OER, conductive carbon and most materials are easily oxidized and corroded, leading to serious deterioration of the electrode performance¹⁰. Another difficulty is that the rapid release of bubbles on the electrode surface will inevitably lead to serious bubble shielding and catalyst spalling under a high current density^{11,12}. Therefore, OER catalysts and electrodes are the main bottlenecks in the development of water splitting devices.

The successful application of water splitting technology depends, to a large extent, on the exploration of novel OER electrocatalytic materials and robust electrodes. A good OER electrode should not only assemble a highly active catalyst on its surface but should also have an open structure and excellent conductivity^{13,14}. This allows the rapid mass transfer of electrolytes and bubbles, as well as strong adhesion between the catalyst and the substrate. In addition, a manufacturing process with simple and scalable active electrodes using affordable equipment is also very conducive to mass production.

IrO₂ and RuO₂ are the most advanced OER electrocatalysts with low overpotentials and low Tafel slopes, especially under acidic conditions^{15–17}. However, these catalysts have the disadvantages of scarcity and high cost and cannot be used for industrial water splitting to obtain economic hydrogen energy resources¹⁸. However, excitingly, under alkaline conditions, some transition metal-based electrocatalysts have excellent catalytic performance when catalyzing the OER and often outperform precious metal-based

^a Faculty of Materials Science and Chemistry, China University of Geosciences, Wuhan 430074, China.

^b JST-ERATO Yamauchi Materials Space-Tectonics Project and International Center for Materials Nanoarchitectonics (WPI-MANA), National Institute for Materials Science (NIMS), 1-1 Namiki, Tsukuba, Ibaraki 305-0044, Japan.

^c Research and Development (R&D) Division, Green Energy Institute, Mokpo, Jeollanamdo 58656, Republic of Korea

^d Australian Institute for Bioengineering and Nanotechnology (AIBN) and School of Chemical Engineering, The University of Queensland, Brisbane, QLD 4072, Australia.

^e ARC Centre of Excellence for Nanoscale BioPhotonics (CNBP), School of Chemistry and Physics, The University of Adelaide, Adelaide, SA 5005, Australia.

† These authors equally contributed to this work.

Electronic Supplementary Information (ESI) available: [details of any supplementary information available should be included here]. See DOI: 10.1039/x0xx00000x

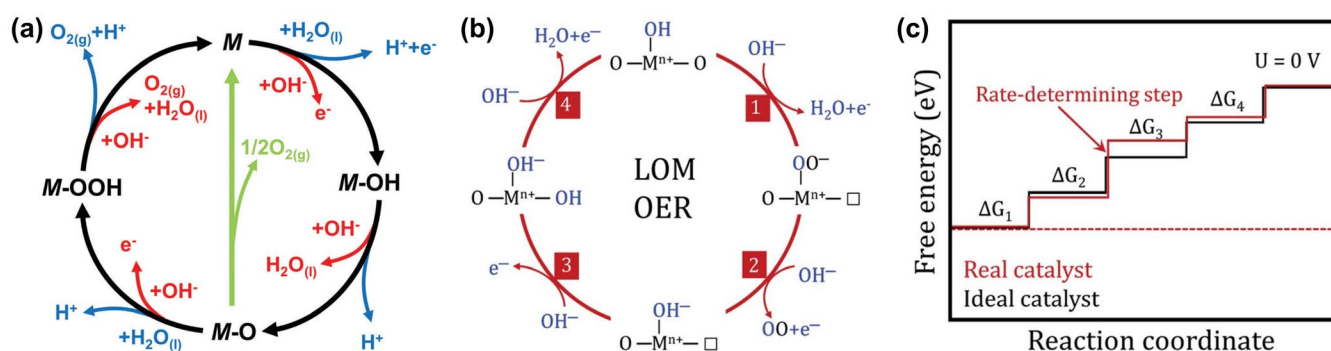


Fig. 1 (a) OER mechanism under acidic (blue line) and alkaline (red line) conditions. The black line indicates that the oxygen evolution involves the formation of a peroxide ($M-OOH$) intermediate (black line), while another route for the direct reaction of two adjacent oxo ($M-O$) intermediates (green) to produce oxygen is also possible⁴⁰. Copyright 2017, The Royal Society of Chemistry. (b) Reaction mechanism for the OER, including the participation of lattice oxygen in an alkaline environment. M represents the active site, and \square represents the oxygen vacancy. Copyright 2020, The Royal Society of Chemistry. (c) Plot of the Gibbs free energy of reactive species and intermediates (horizontal lines) of the OER versus the reaction coordinates¹³. Copyright 2020, The Royal Society of Chemistry.

electrocatalysts^{19–23}. Transition metal-based electrocatalysts are promising OER electrocatalysts due to their special electronic structure, stable chemical properties, and high intrinsic activity. To prepare such electrodes, typical synthesis strategies have been developed, including hydrothermal, solvothermal, vapor deposition, high-temperature solid-state reaction, and sol-gel methods^{24–28}. However, most synthesized products are powdered and need to be mixed with conductive carbon and polymer binders to form a slurry for further use. Such synthesis routes are relatively complex and have a low utilization rate of the active centers of the catalysts; thus, catalyst shedding problems can easily occur^{11,29}. In contrast, electrochemical synthesis is a unique technique for preparing electrode materials, which has the following advantages^{30–33}. i) Electrochemical synthesis is carried out in an electric double layer with a nanometer thickness, and the high potential gradient can reach 10^{-5} V cm^{-1} , and many materials that are difficult to obtain by chemical methods under general environmental conditions can be synthesized³¹. ii) Electrodeposition is mainly a surface-induced reaction, which can be used in interface engineering, especially in the application of electrocatalytic OERs. iii) The self-supporting electrode can be easily fabricated by electrodeposition, and the deposited coating is firmly attached to the substrate. Compared with traditional drop cast electrodes, self-supporting electrodes synthesized by electrochemistry have the advantages of high utilization of active centers and simple preparation processes^{20,34,35}. iv) The electrode composition can be easily adjusted by changing the type of precursor solution to prepare almost all metal-based materials³⁶. v) Electrochemical synthesis is a low-cost solution-based method that can be operated under ambient conditions and is suitable for practical industrial scale-up. Benefiting from the above advantages, many recent innovations in water splitting have been achieved through electrochemical synthesis; thus, there is currently unprecedented interest in electrochemical synthesis.

Although some excellent review articles on electrochemical synthesis have been published, they are mainly focused on photocatalysis^{16,30}, supercapacitors³², or batteries³⁶. Few studies have reviewed the latest progress in the development of transition metal-based OER

electrocatalysts prepared by electrochemical synthesis. In this article, we provide a comprehensive review of the electrochemical synthesis of nano/microstructure transition metal-based OER materials. First, some fundamentals of electrochemical synthesis are introduced, including common electrochemical synthesis strategies, common electrochemical synthesis substrates, the electrolyte used in electrochemical synthesis, and the combination of electrochemical synthesis and other synthesis methods. Second, the morphology and properties of electrochemical synthetic materials are summarized and introduced from the aspect of structural design. Then, the latest progress regarding the development of transition metal-based OER electrocatalysts is reviewed, including the classification of metals/alloys, oxides, hydroxides, sulfides, phosphides, selenides, and other transition metal compounds. In addition, the oxygen evolution mechanisms and rate-determining steps (RDSs) of transition metal-based catalysts are also discussed. Finally, the advantages, challenges, and opportunities regarding the application of electrochemical techniques in the synthesis of transition metal-based OER catalytic materials are summarized.

2. Oxygen evolution mechanism and rate-determining steps of transition metal-based catalysts

Electrochemical water splitting is a mature technology that was discovered as early as the 19th century. However, the anodic reaction of water oxidation remains a mystery. The exact reaction mechanism is not completely clear, and an ideal catalyst is still under development; many unsolved issues and great challenges remain in the field of OER. From the perspective of energy and environmental crises, there is an urgent need to develop highly active, stable, and inexpensive OER electrocatalysts^{8,37,38}. Generally, the optimization of the catalyst design requires a better understanding of the electrochemical reaction mechanism³⁹. Herein, based on the current fundamental understanding of the OER mechanism, we briefly

summarize the reaction pathway and the RDS of the OER related to transition metal-based catalysts.

2.1 OER mechanism

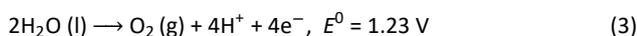
For the water splitting reaction, the process of the cathodic hydrogen evolution reaction is different from that of the anodic OER under acidic or alkaline conditions, as shown in Equations 3 and 10. Many research groups have proposed the reaction mechanism of oxygen evolution in an acidic electrolyte or alkaline electrolyte, but these understandings are inconsistent. Most people agree that there are two types of reaction intermediates, MOH and MO, while the major difference is probably due to the different steps used in oxygen generation. The intermediate MO is believed to undergo two different reaction paths during the formation of oxygen. One is the green route, as shown in Fig. 1a, where two MO intermediates are directly combined to produce O₂, such as the reaction in Equation 6. The other is to form MOOH intermediates (Equations 7 and 14), which subsequently decompose and release O₂, as illustrated in the black route in Fig. 1a and Equations 8 and 12. Although there are differences, researchers agree that the electrocatalysis of the OER is a heterogeneous reaction process, and the M-O bond energy state of the reaction intermediate plays a crucial role in the overall electrocatalytic ability⁴⁰.



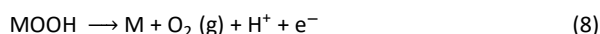
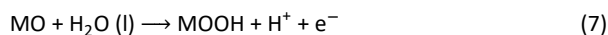
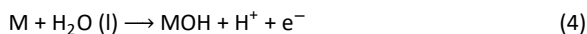
Cathodic reaction in an acid electrolyte,



And anodic reaction in an acid electrolyte,



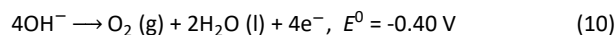
The proposed mechanism under acidic conditions is as follows:



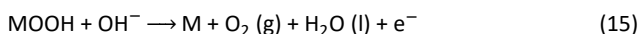
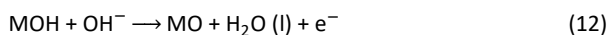
Cathodic reaction in an alkaline electrolyte,



And anodic reaction in an alkaline electrolyte,



The proposed mechanism under alkaline conditions is as follows:



In addition to the conventional mechanism, the one with lattice oxygen (O²⁻) catalyst participation has recently been extensively considered as an alternative reaction pathway in (hydro)oxides (Fig. 1b)¹³. The Sabatier principle is still valid in the lattice oxygen mechanism (LOM) process, while, It is worth noting that the active

sites are no longer limited to the metal centers. Dynamic catalyst active sites may also arise as a result of the oxidation of O²⁻ anions⁴¹. Despite the similarity in the form of these intermediates to those in the conventional mechanism, the LOM differs in the generation of a vacant oxygen site upon the evolution of a lattice oxygen-containing oxygen molecule, which is associated with the decoupling of a certain proton-electron transfer step⁴². The lattice oxygen evolved at the surface (which leaves behind a surface vacancy) will be quickly replenished by oxygen ions diffusing from the bulk of the electrocatalyst. Thus, increasing the oxygen ion diffusion rate will facilitate the refilling of the surface lattice oxygen as it is consumed, accordingly promoting the catalytic OER process. Undoubtedly, it becomes more complex to determine a single guiding parameter in the LOM to describe OER activity.

Electrocatalysts accelerate the OER through facilitating the required electron transfer, as well as the formation and rupture of chemical bonds^{43,44}. This involvement in fundamentally different processes leads to complex electrochemical kinetics, which can be challenging to understand, control, and usually depends exponentially on overpotential^{45,46}. This behavior occurs when the applied bias drives the reaction in line with the phenomenological Butler-Volmer theory, which focuses on electron transfer, enabling the use of Tafel analysis to gain mechanistic insight under quasi-equilibrium or steady-state assumptions^{47,48}. However, the charging of catalyst surfaces under bias also affects bond formation and rupture, and the effect on the electrocatalytic rate is not accounted for by the phenomenological Tafel analysis and is often unknown^{49,50}. While, Jones *et al.*⁵¹ reported that the applied bias does not act directly on the reaction coordinate, but affects the electrocatalytically generated current through charge accumulation in the catalyst. And they also find that the activation free energy decreases linearly with the amount of oxidative charge stored; that is, the high oxidation state of the active center metal is more in favor of accelerating OER.

2.2 Rate-determining steps of OER

As a complex reaction of multielectron transfer, the OER involves many reaction processes and reaction paths, including the adsorption of reactants, the adsorption and desorption of intermediates, the desorption of products, and the rapid transfer of electrons^{41,52,53}. Determining the RDS of the OER has important guiding significance for understanding and designing high-performance catalysts³⁹. The following is a brief introduction to the RDS of the OER from the perspective of the electrochemical Tafel slope and theoretical calculation of the intermediate state adsorption energy.

2.2.1 Experimental Tafel slope

The kinetic parameter is an important index to evaluate the performance of the electrocatalyst, and the Tafel slope can reflect the catalytic mechanism of the catalyst and the RDS of the catalytic reaction to a certain extent. In the reaction of a single electron transfer, the transfer coefficient (α) usually refers to the symmetry factor (β), namely, Equation 16⁴⁰. In most cases, since the overpotential η required is much smaller than the recombination energy (λ), the symmetry coefficient (β) is 0.5. If this assumption is valid, one can calculate the Tafel slope for a single electron reaction and yield a value of 120 mV dec⁻¹, indicating that the single electron transfer reaction is the RDS of this electrochemical system.

$$\alpha = \beta = 1/2 + \eta/\lambda \quad (16)$$

In fact, the processes involved in a variety of electrochemical systems are much more complex than the single-electron transfer processes mentioned above, which usually include a series of consecutive reaction steps. These processes include not only electron transfer steps but also chemical reaction steps, such as association reactions and dissociation reactions. Bockris and Reddy inferred the transfer coefficient of the multielectron transfer reaction, as shown in Equation 17⁵⁴, where n_b refers to the number of electrons transferred from the electrocatalyst to the electrode before the RDS, ν refers to the stoichiometric number which describes how many times the RDS takes place in one reaction cycle, and n_r refers to the number of electrons involved in the RDS reaction. Guidelli *et al.*⁵⁵ suggested that it is unlikely to have more than one electron transferred simultaneously; hence, n_r is either 1 or 0.

$$\alpha_a = n_b/\nu + n_r\beta \quad (17)$$

And the correlation between the anodic Tafel slope (b_a) and anodic transfer coefficient (α_a) is:

$$b_a = 2.303 R T / (\alpha_a F) \quad (18)$$

in which R is the universal gas constant ($R = 8.314 \text{ J mol}^{-1} \text{ K}^{-1}$), T is the temperature, and F is the Faraday constant ($F = 96485 \text{ C mol}^{-1}$). Thus, we can employ Equation 17 and 18 to speculate the RDS of the electrocatalytic reaction. If the first electron transfer reaction is the RDS (Equation 11), then the values of n_b and ν are 0 and 1, while the values of n_r and β are 1 and 0.5, respectively. In this case, the calculated transfer coefficient is 0.5, and the corresponding Tafel slope is 120 mV dec^{-1} , which is similar to the single-electron transfer reaction. While, in the situation of the existence of a surface chemical rearrangement step ($\text{MOH}_{\text{ads}} \rightarrow \text{MOH}_{\text{ads}}^*$)⁵⁶, if the RDS is the chemical reaction after the first electron transfer, then the values of n_b and ν are both equal to 1, while the value of n_r is 0. In this way, the transfer coefficient is consistent, and the Tafel slope is reduced to 60 mV dec^{-1} . On the other hand, if the second electron transfer (Equation 12) in the black route in Fig. 1 is the RDS, then the values of n_b and ν are both equal to 1, n_r and β are 1 and 0.5, respectively, the transfer coefficient is 1.5, and the Tafel slope is 40 mV dec^{-1} . For the OER (a four-single electron transfer is involved), assuming that the RDS is the third electron transfer step (Equation 14), n_b and ν are equal to 2 and 1, respectively, while n_r and β are 1 and 0.5, respectively. Thus, the transfer coefficient is 2.5, and the Tafel slope is 24 mV dec^{-1} ⁵².

2.2.2 Adsorption energy of the DFT intermediate state

Having a detailed understanding of the interaction between oxygen intermediates and the catalyst surface is of great significance to improve the overall OER performance of the catalyst. However, it is very difficult in practice to thoroughly understand each of the basic steps of the OER and the dynamic description it contains. Fortunately, density functional theory (DFT) calculations provide a simple route and an in-depth understanding of the reaction steps. The transition metal-based oxygen evolution catalyst is still (hydro)oxides, which play an important role in the catalytic process. The thermodynamic modeling of the electrochemical reaction of (hydro)oxides in the OER process has attracted wide attention. The pioneer of DFT, Norskov *et al.*, established a universal framework for

OER kinetics on the surface of metal (hydro)oxides⁵⁷. Typically, the theoretical OER overpotential (η) among different catalysts can be associated with a single descriptor that follows the Sabatier principle. In particular, the reaction energy of each basic step is determined by the difference in the adsorption energy between two intermediates (such as $\Delta G_{\text{O}^*} - \Delta G_{\text{OH}^*}$). As shown in Fig. 1c, reaction free energy diagrams are drawn to determine the thermodynamic RDS. Due to the irregular change in the adsorption energy of the intermediate species, the reaction energy of each step is different. The step with the maximum free energy is the RDS, which is responsible for the overpotential η of the OER. In an ideal catalyst, the free energy of every step is equal to the minimum overpotential. To minimize the overpotential, the binding energy of the intermediates can be adjusted according to the metal type, electronic structure, adsorption species, solvent interaction, *etc.*

3. Fundamentals of electrochemical synthesis technology

Electrochemical synthesis is a mature technology with a history of more than 200 years. In 1800, Volta developed the first volt reactor, which successfully converted chemical energy into electricity and achieved a continuous power supply. Davy first accurately applied electricity to discover new elements in 1807. The alkali metals sodium and potassium were the earliest products obtained by electrochemical synthesis. Since then, the scientific community has witnessed the rapid development of electrodeposition technology and its underlying mechanisms. At present, electrochemical synthesis is considered one of the most ideal methods for the preparation of OER electrocatalytic materials⁵⁸. These electrocatalytic materials usually have adjustable shapes, thicknesses, or sizes^{30,59,60}.

3.1 Common electrochemical synthesis methods

Cyclic voltammetry (CV), galvanostatic deposition, potentiostatic deposition, pulse deposition and electrophoretic deposition (EPD) are the most widely and extensively investigated and practiced electrochemical synthesis techniques for the application of nano/microstructured materials as oxygen evolution catalysis electrodes. These processes are usually implemented in an electrolytic cell powered by an electrochemical workstation (Fig. 2a). Electrochemical synthesis devices are divided into the following two types based on the number of electrodes involved: two-electrode and three-electrode devices. The two-electrode system consists of a positive electrode and a negative electrode, both of which are immersed in electrolytes. The electrochemical workstation or power source provides voltage between the electrodes. Therefore, the voltage measured in this case is the overall cell voltage. The three-electrode system consists of a working electrode (WE), a counter electrode (CE), and a reference electrode (RE). Ideally, the current flows only between the WE and CE, and the potential of the WE refers to the voltage between the WE and the RE. Saturated calomel electrodes (SCEs), Ag/AgCl electrodes, and Hg/HgO electrodes are common REs in three-electrode systems. The RE is placed near the WE to minimize the IR drop and voltage fluctuation caused by the electrolyte resistance.

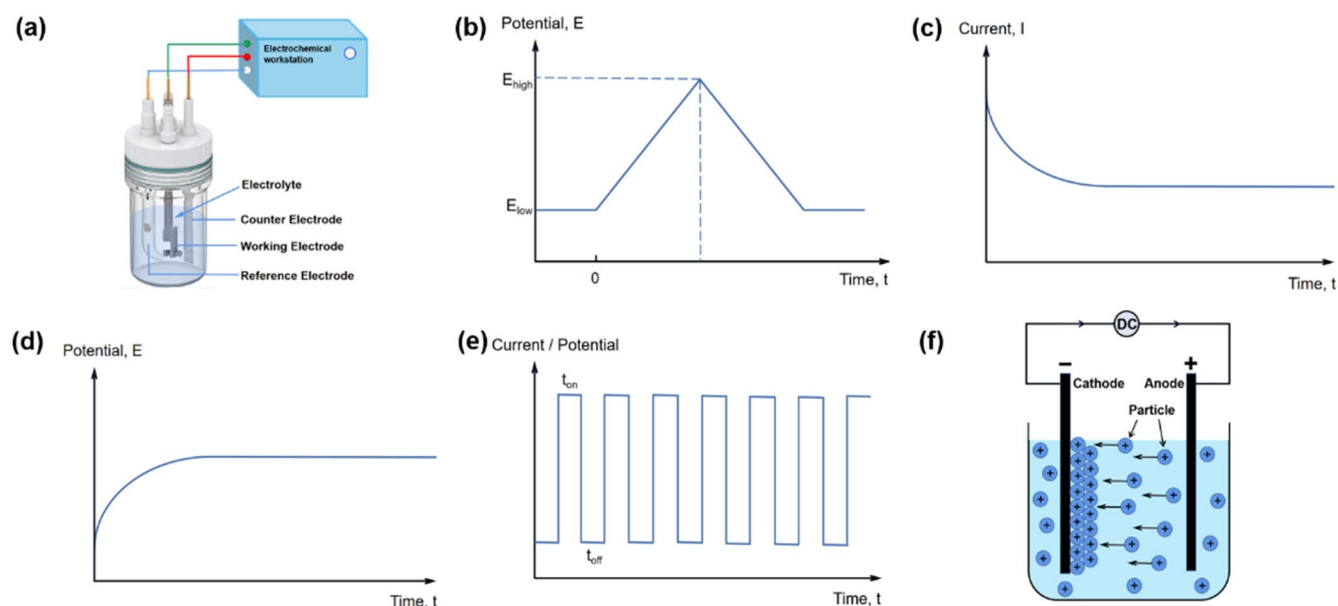


Fig. 2 (a) Schemes illustrating the experimental setups of three-electrode electrolytic cells for electrochemical syntheses. (b) Potential-time fluctuation curve of cyclic voltammetry electrodeposition. (c) Current-time curve of potentiostatic electrodeposition. (d) Potential-time curve of galvanostatic electrodeposition. (e) Current or potential signals applied in pulse electrodeposition. (f) Schematic diagram of the electrophoretic deposition cell⁶⁸. Copyright 1996, Wiley-VCH.

3.1.1 Cyclic voltammetric electrodeposition

In addition to the traditional electrochemical techniques used to detect electrochemical redox activity, CV can also be used as a synthetic method⁶¹. It linearly scans the potential in a range, called the potential window, and records the current as a response. Forward scanning increases the applied potential and oxidizes the species on the electrolyte or electrode to produce anodic current. In contrast, reverse scanning reduces the applied potential, reduces the active components, and produces a cathodic current. Fig. 2b shows the potential-time fluctuation curve of CV electrodeposition.

As a comprehensive approach, CV has three main advantages. First, it allows the determination of the initial potential of the electrodeposition reaction. The oxidation or reduction reactions involving charge transfer across the electrolyte-electrode interface will show a sharp increase or clear peak in the current. Since the initial potential is the minimum voltage required to initiate the electrodeposition reaction, CV is very useful for the formulation of experimental schemes. Second, the potential linear scanning of CV is beneficial to the growth of uniform and conformal thin films. This characteristic provides a gradient driving force for deposition; i.e., deposition begins only when the potential is scanned above the initial potential, and the deposition driving force increases linearly with increasing potential and gradually away from the initial potential. This CV gradient driving force adjusts the deposition rate to avoid persistent high deposition voltage, which can lead to overgrowth of materials, rapid blockage of pores and/or uneven film deposition. Third, CV is suitable for the synthesis of multivalent materials, such as transition metal oxides.

3.1.2 Potentiostatic electrodeposition

Potentiostatic deposition synthesizes the material by applying a constant voltage between the positive and the negative electrode

(two-electrode system) or a constant potential difference between the working and the reference electrode (three-electrode system). The deposition potential is kept constant by the electrochemical workstation, and the current is recorded as a function of time, as shown in Fig. 2c. According to the difference in the applied potential and thermodynamic equilibrium potential, the constant potential deposition can be divided into underpotential deposition (UPD) and overpotential deposition (OPD).

UPD occurs at a potential lower than the thermodynamic equilibrium potential. UPD includes the adsorption, nucleation, and growth processes determined by the surface properties of the substrates (such as chemical composition, crystal structure, morphology, and electrolyte wettability) and ion-substrate interactions. In addition, the types of cations in the electrolytes and anions greatly influence the structure, properties, and deposition kinetics of deposited materials⁶². OPD occurs at a potential higher than the thermodynamic equilibrium potential. The structure and properties of OPD coatings are highly dependent on a variety of factors, including overpotential (the difference between the applied potential and equilibrium potential), electrolyte concentration, growth mechanism, and deposition-substrate interactions. It is worth noting that diffusion-controlled nucleation is usually the RDS of OPD, while the RDS of UPD is the deposition lattice binding to the substrate⁶³.

3.1.3 Galvanostatic deposition

Galvanostatic deposition refers to the electrodeposition of constant current between the positive and negative electrodes of the two-electrode system or between the working electrode and the counter electrode of the three-electrode system. The recorded response is the time-dependent voltage of the electrolytic cell (two-electrode system), i.e. the potential of the working electrode (three-electrode

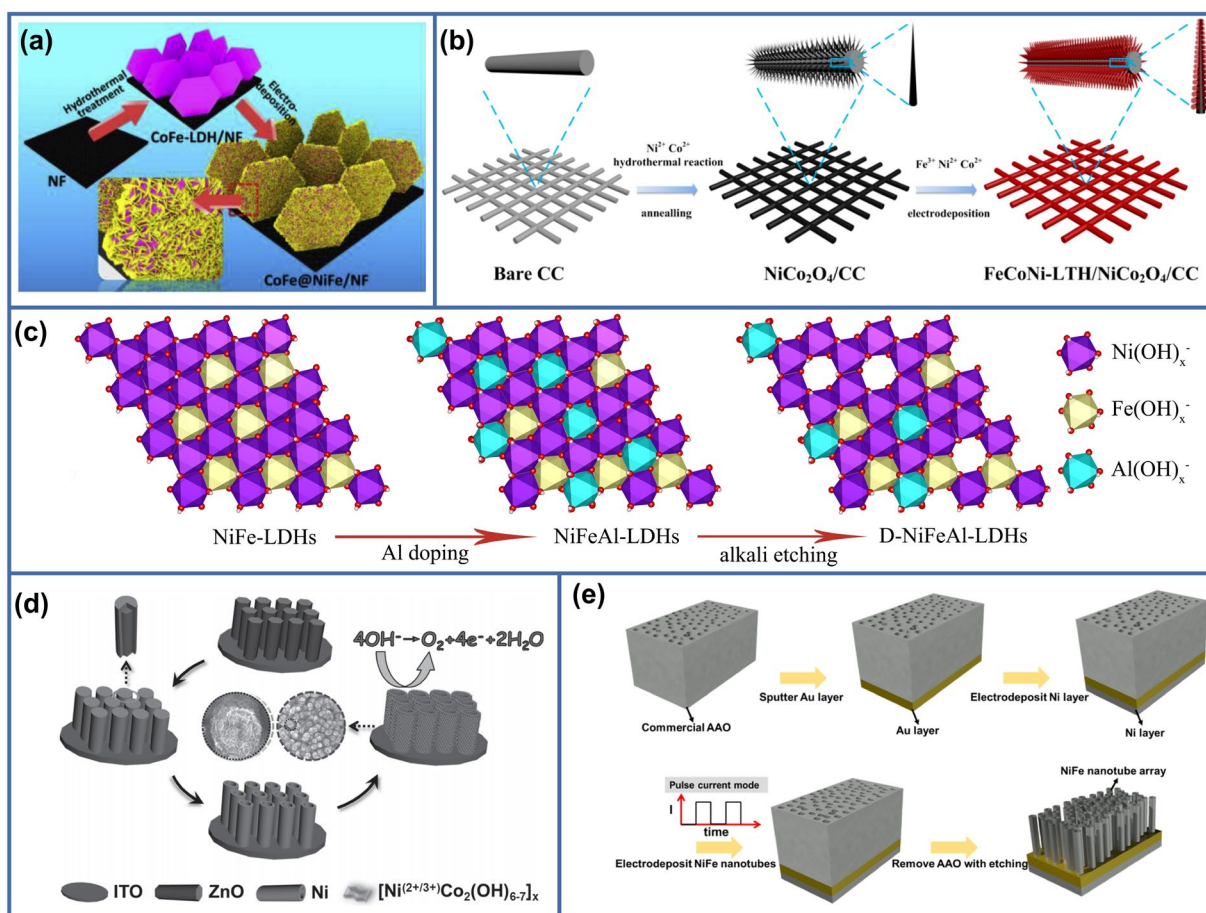


Fig. 3 (a) Schematic diagram for the fabrication of the CoFe@NiFe/NF architecture⁹⁰. Copyright 2019, Elsevier. (b) Preparation Procedure for FeCoNi-LTH/NiCo₂O₄/CC⁶⁹. Copyright 2017, American Chemical Society. (c) Schematic illustration of the preparation of D-NiFeAl-LDHs⁹¹. Copyright 2019, Elsevier. (d) Schematic illustration of the fabrication of the three-dimensional (3D) NNCNTA water oxidation electrode by means of electrodeposition⁷⁶. Copyright 2014, Wiley-VCH. (e) Schematic illustration of the fabrication process for the NiFe Nanotube Array⁹². Copyright 2019, American Chemical Society.

system). As shown in Fig. 2d, the V - t curve is sometimes called a galvanostatic curve. While potentiostatic deposition can begin at the moment the potential is applied, galvanostatic deposition takes a short time to begin⁶⁴. This is because some applied currents are needed to charge the double layer capacitor (C_{dl}) first. When the potential reaches a certain threshold (usually the equilibrium potential plus overpotential), an electrochemical reaction occurs. Therefore, the constant current (I) is contributed by two components, i.e., I_{dl} and I_{ct} , where I_{dl} is the capacitive current for charging C_{dl} and I_{ct} is the charge transfer current for electrodeposition. When electrodeposition starts, I_{dl} quickly approaches zero. The V - t curves of galvanostatic deposition contain essential information on electrodeposition chemistries. Since the charging time of C_{dl} is on the order of milliseconds, almost all the V - t curves collected on the time scale of minutes or hours are contributed by electrodeposition.

3.1.4 Pulse electrodeposition

Pulse electrodeposition refers to the rapid alternation of potential or current density between two different values. This is achieved by a series of pulses with equal amplitude, duration, and polarity, which are separated by periodic zero current or open-circuit potential⁶⁵.

Each pulse consists of an "ON" time for applying potential or current and an "OFF" time for applying open-circuit potential or zero current, as shown in Fig. 2e. During the "OFF" period, the ions in the electrolyte diffuse into the electric double layers along the surface of the deposited substrates, which is beneficial to uniform fine grain deposition during the "ON" period⁶⁶.

3.1.5 Electrophoretic deposition

Electrophoretic deposition is different from all the above techniques. First, the charge carriers in EPD are suspended charged colloidal particles, not ions. Second, EPD involves the electrostatic attraction between the particles and the substrate but does not involve charge transfer. Third, unlike electrodeposition, which requires electrolytes to conduct ions, EPD can operate in a medium with poor conductivity, such as water⁶⁷.

According to the charge carried by colloidal particles, EPD can be divided into cathodic EPD and anodic EPD. Cathodic EPD refers to the deposition of positively charged particles on a negatively charged substrate, while anodic EPD is performed in the opposite way, as shown in Fig. 2f. The structure of the deposits can be adjusted by changing the parameters of the applied voltage, particle

concentration, and deposition time. It is worth noting that the stoichiometric ratio of electroadsorbed particles directly determines the stoichiometric ratio of sediments⁶⁸.

3.2 Substrates for electrochemical synthesis catalysts

As an important part of electrochemical synthesis systems, substrates play the role of supporting catalysts and act as electronic conductors in the catalyst synthesis process^{10,37}. The electrochemical synthesis process is generally carried out in a two-electrode or three-electrode electrochemical cell, and the conductive substrate is selected as the working electrode. Under the action of an external electric field, the target material is deposited uniformly and rapidly on the surface of the substrate. Most transition metal-based materials, including metals/alloys, oxides, hydroxides, sulfides, phosphides, selenides, and polyanion compounds, can be electrodeposited on conductive substrates. The catalysts synthesized *via* electrochemical technologies can be deposited and grown in situ on the substrates, the catalysts are closely combined with the substrates, and the overall electrodes can be applied as water splitting catalysts, which can show excellent catalytic activity and stability.

Common substrates are mainly concentrated on carbon materials, metals and several other forms of conductive materials, including carbon fiber paper (CFP)⁶⁹, carbon cloth (CC)⁵⁹, graphite plates, metal foams (*e.g.* Ni/Cu foam)^{70,71}, metal mesh (*e.g.* Ti/Ni mesh)⁷², metal plates/foils (*e.g.* Ti plate and Ni/Cu foil)^{73–75} and fluorine-doped tin oxide (FTO)⁷⁶.

3.3 Electrolyte for electrochemical synthesis

The solution-based properties of electrochemical synthesis allow for the easy manipulation of various synthesis variables, including pH, temperature, additives, and soluble precursor concentrations, which significantly affect the morphologies of the catalysts (such as the surface area, nanostructure, and orientation). Additionally, uniform doping and solid solutions can be easily obtained by changing the composition of the plating solution. Therefore, a special morphology and composition control level can be achieved³⁰. It should be pointed out that the electrolytes involved in this paper are all aqueous electrolytes.

3.3.1 Salt component of electrolyte

When preparing transition metal-based catalysts *via* direct electrodeposition, different electrolyte salts should be selected for different electrosynthesis purposes. The composition and doping of the product can be controlled by adjusting or changing the concentration or composition of metal salts in the electrolyte. For example, in the synthesis of hydroxide catalysts, nitrates containing corresponding transition metal elements are generally selected^{11,20}. While synthesizing oxides, different transition metal salts will be selected according to the oxide types^{77,78}. In the electrosynthesis of sulfides, in addition to the corresponding metal salts, thiourea containing sulfur elements should be added as the sulfur source^{79,80}. Additionally, in the electrosynthesis of transition metals/alloys, the corresponding sulfates and chlorides should be selected as the main salts of the electrolyte, and a variety of secondary salts and additives also need to be added^{60,81}.

3.3.2 Additives of electrolyte

In addition to the main salt components, some secondary salts and additives will be added to the electrolyte to increase the conductivity of the electrolyte, accelerate the nucleation rate of the deposited products, improve the morphology of the electrosynthesis catalyst or enhance the binding force between the catalysts and the substrates. According to the different purposes of synthesis, electrolyte additives can be selectively added. For example, in the electrochemical synthesis of transition metal hydroxides, NH_4NO_3 is sometimes added to increase the conductivity of the electrolyte. Citric acid and L-ascorbic acid are added in the preparation of Ni-Fe alloys by electrodeposition⁸². Citric acid is used as a complexing agent in the Ni-Fe electrolyte, and the complexing effect of citrate ions shifts the reduction potential of the Ni-Fe alloy to a more negative potential and increases the diffusion-limited current. The other effect is an increase in the nucleation sites and nucleation rate. L-ascorbic acid can prevent the oxidation of $\text{Fe}^{2+}/\text{Fe}^{3+}$ during electrodeposition, and the presence of L-ascorbic acid in the electrolyte inhibits the formation of Fe hydroxide films⁸³. However, in the electrodeposition of the NiCuP catalyst, ethylenediamine will be added as the complexing agent to affect the deposition process of the products⁸⁴.

3.3.3 pH of electrolyte

The effect of the electrolyte pH on the electrodeposition products is also very obvious, and the corresponding deposition products will be formed in a specific pH range, but sometimes a variety of products will be codeposited. Therefore, it is particularly important to control the electrolyte pH in some cases, and the pH is generally adjusted by adding an acid-base or buffer solution. For example, in the electrodeposition process of Ni-Fe alloys, an electroplating solution with a pH of 2–3.5 is used. At higher pH values, the formation of hydroxides, especially Fe hydroxide, is possible. The results of previous studies suggest that a decrease in the pH value will reduce the current efficiency and iron content in the coating⁸⁵. In the electrochemical synthesis of the NiCuP catalyst, KOH or H_2SO_4 was added to adjust the pH to 10.4 to obtain the best NiCuP catalyst products⁸⁴. In the preparation of transition metal hydroxides, good deposition products can be obtained without adding an acid base or buffer solvent because the pH range of transition metal hydroxide deposition is generally wide.

3.3.4 Electrolyte temperature

In the process of electrodeposition, the electrolyte temperature can affect the migration rate of transition-metal ions, thus affecting the nucleation rate of the deposition products, changing the morphology and crystallinity of the products, and finally affecting the electrochemical performance^{86,87}. For example, when Oliveira *et al.*⁸⁸ electrodeposited the Ni-Co-W alloy, it was found that the bath temperature favored Ni deposition when the temperature was extrapolated to lower values, *i.e.*, 21.48 °C. Co deposition was favored when the bath temperature was extrapolated to high values, *i.e.*, 63.52 °C. As the temperature increases, the ion mobility increases, which is beneficial to the reduction of Co in the coating. Poizot *et al.*⁸⁹ electrodeposited Fe_3O_4 on a copper substrate and found that the X-ray diffraction (XRD) pattern of the Fe_3O_4 coating changed with the growth temperature (40–60 °C) during a fixed electrodeposition time of 180 s. That is, a copper substrate with good Fe_3O_4 coverage could not be obtained at a lower temperature.

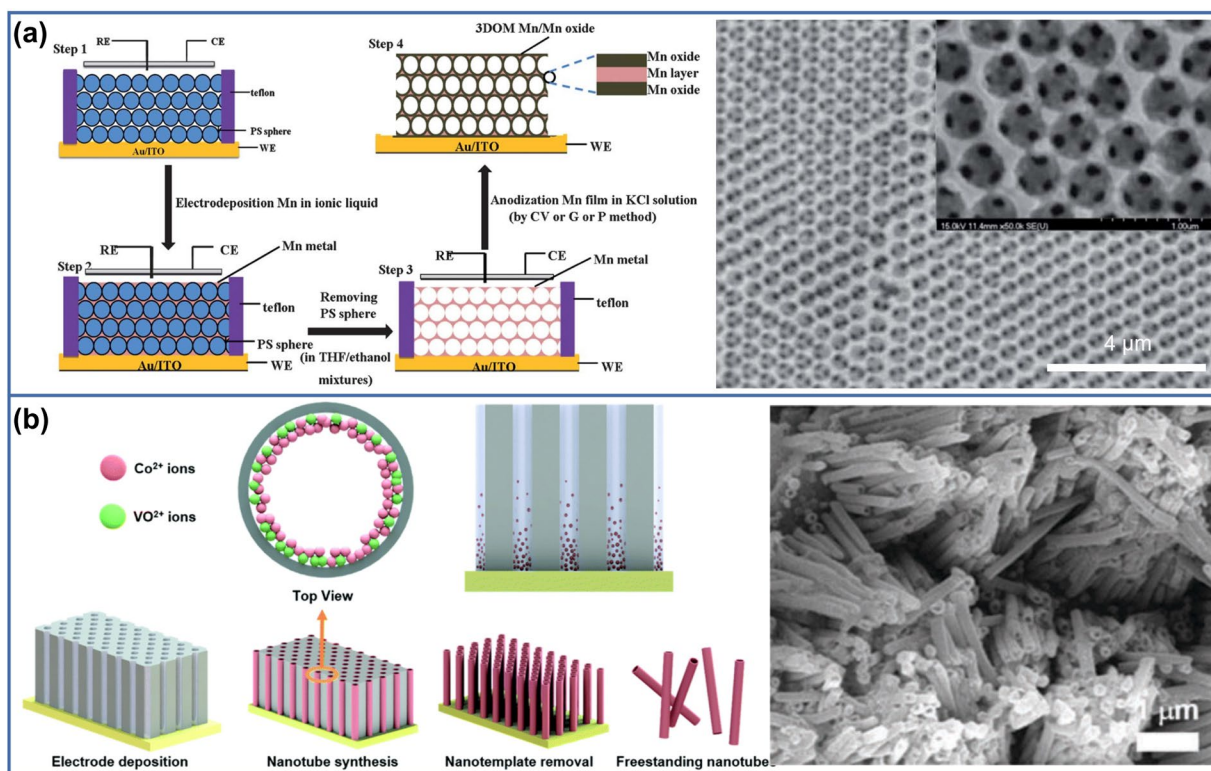


Fig. 4 (a) Scheme for preparing a high-porosity 3DOM Mn/Mn oxide electrode and its related SEM image⁹³. Copyright 2013, The Royal Society of Chemistry. (b) Schematic representation of the Co NT fabrication process. The top and side scheme images show the formation of NTs attaching to the AAO wall under the application of an electrical field in the early stage and its related SEM image⁹⁴. Copyright 2017, The Royal Society of Chemistry.

Regardless of the growth temperature, the XRD spectrum confirms the deposition of Fe_3O_4 , and the scanning electron microscopy (SEM) images show that there are uniform coatings on all the samples. As expected, the morphology showed shapeless particles even after 180 s of electrolysis at lower temperatures. With decreasing deposition temperature, the position of the Bragg peak of Fe_3O_4 moves to a higher 2θ value, which may be due to the formation of a more strained structure at a lower temperature.

3.4 Combination of electrochemical synthesis technology and other synthetic methods

As a simple, convenient, and fast method for the preparation of electrocatalysts, electrochemical synthesis has been widely used in the field of catalyst preparation and has gradually developed from a single electrodeposition method to a composite catalyst preparation method combined with a variety of preparation methods. Catalysts prepared *via* electrodeposition are generally amorphous and have small structures, so they are easily further attached to substrates or precatalysts with larger structures, which provides a basis for the combination of electrochemical synthesis technology and other synthesis methods. Several common methods for preparing materials combined with electrochemical synthesis are introduced below.

3.4.1 Electrochemical synthesis and the hydrothermal method

The hydrothermal method is a common catalyst preparation strategy. The catalysts obtained by this method generally have good crystallinity and outstanding morphology (such as large nanosheets

and nanowire array structures). Catalysts prepared via hydrothermal and electrochemical synthesis methods will show the morphological characteristics of multiple loads. For example, Yuan's group⁹⁰ first hydrothermally prepared CoFe-layered double hydroxide (LDH) catalysts with larger nanosheet arrays on Ni foam (NF) and then electrodeposited smaller NiFe-LDH nanosheets with amorphous forms on the precursor of CoFe-LDH/NF to obtain a multiloaded hierarchical core-shell CoFe-LDH@NiFe-LDH/NF catalyst, as shown in Fig. 3a. The catalyst showed high electrocatalytic activity and stability for oxygen evolution. Sun *et al.*⁶⁹ prepared a multiloaded FeCoNi-LTH/ NiCo_2O_4 /CC catalyst on carbon cloth *via* hydrothermal calcination and electrosynthesis; the preparation process is shown in Fig. 3b. The catalyst exhibits a hierarchical structure of nanowire arrays supported by small nanosheets and shows efficient oxygen evolution performance.

3.4.2 Electrochemical synthesis and etching method

The etching method is a common auxiliary strategy for the preparation of porous catalysts, removal of templates, dealloying, and manufacture of catalyst defects. The principle is based on the amphoteric characteristics of some specific metals (such as Zn and Al) and their oxides/hydroxides, which can be selectively dissolved in strong alkali (or low concentration strong acid) solutions. This method is often combined with electrochemical synthesis for the rapid preparation of porous or defective catalysts. As illustrated in Fig. 3c, our research group adopted this method to electrodeposit a NiFeAl-LDH catalyst on NF first; then, a type of high-efficiency D-

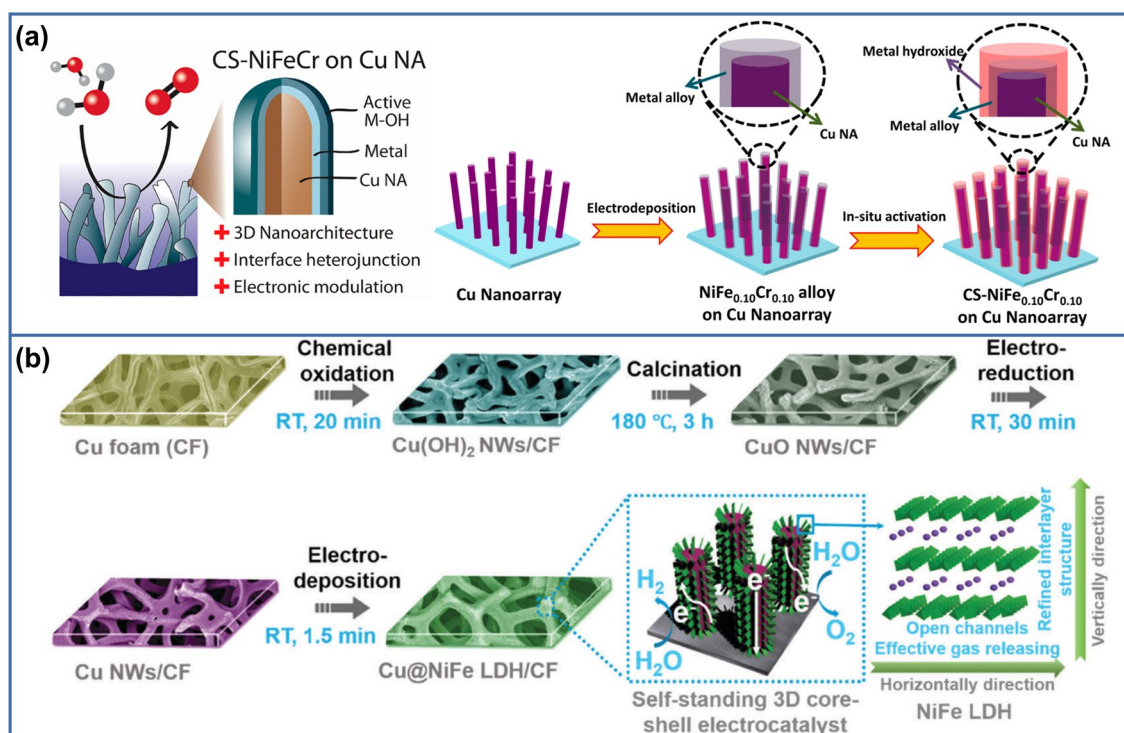


Fig. 5 (a) Schematic Process for the synthesis of CS-NiFe_{0.10}Cr_{0.10}.⁹⁷ Copyright 2018, American Chemical Society. (b) Schematic illustration of the fabrication procedures of the self-standing 3D core-shell Cu@NiFe LDH electrocatalysts.⁹⁸ Copyright 2017, The Royal Society of Chemistry.

NiFeAl-LDH/NF oxygen evolution catalyst with a metal deficiency was prepared by a strong alkali etching method⁹¹. Jin *et al.*⁷⁶ used a two-step electrodeposition method to prepare a Ni@ZnO nanoarray structure on ITO, and then 2 mM H₂SO₄ was employed to etch ZnO to obtain hollow Ni nanotube arrays. On this basis, a highly efficient oxygen evolution catalyst with amorphous NiCo-LDH nanosheet-coated hollow nanotube arrays was prepared by further electrodeposition, as shown in Fig. 3d. Lu *et al.*⁹² first prepared a NiFe alloy precursor by pulse electrodeposition on an alumina porous membrane template; then, the template was etched to obtain a NiFe alloy nanotube array for water splitting. Fig. 3e shows the preparation process.

3.4.3 Electrochemical synthesis and template method

The template synthesis method involves depositing the related materials into the holes or onto the surface of the templates and then obtaining nanomaterials with the standard morphology and size of the templates by removing the templates by physical or chemical methods. The substances with the following characteristics are used as templates: nanostructure, easy to control, and non-precious. The template method is an important method for the synthesis of nanocomposites and is also the most widely used method in the research of nanomaterials, especially in the preparation of nanomaterials with specific properties. With the template method, the material and structure of the template can be designed according to the performance requirements and morphology of the synthetic materials to meet the actual needs. The template method is often employed in conjunction with electrochemical synthesis to prepare composite oxygen evolution catalysts with special or specific nanostructures. As shown in Fig. 4a, Deng *et al.*⁹³ prepared three-

dimensionally ordered macroporous (3DOM) metallic Mn films with ordered polystyrene (PS) templates by electrodeposition from an ionic liquid. Then, a 3DOM Mn core-Mn oxide shell film was prepared by anodizing a 3DOM Mn film in KCl aqueous solution. Kim *et al.*⁹⁴ prepared Co nanotubes *via* galvanostatic electrodeposition in a Co precursor electrolyte containing VO²⁺ ions and sulfate ions using nanoalumina as templates (Fig. 4b). Because VO²⁺ ions tend to attach to the template wall, they were used to attract Co ions to form Co nanotubes rather than nanowires. The experimental results confirmed that the growth of nanotubes is a function of the current density and synthesis time, and the thickness and length of a nanotube film can be controlled by varying the applied current density and deposition time.

3.4.4 Electrochemical synthesis and heat treatment

The heat treatment applied in the preparation of catalyst materials includes calcination, thermal annealing, sulfuration, and phosphorization. After heat treatment, the materials maintain the morphological characteristics of the raw materials, while the electrical conductivity and catalytic performance will be significantly improved. Heat treatment is usually combined with electrochemical synthesis to prepare efficient oxygen evolution catalysts quickly. There are generally two routes for combining heat treatment and electrochemical synthesis; the first is the electrochemical synthesis of catalyst precursors on substrates, and then heat treatment is applied to obtain the final catalysts; the second involves first applying the heat treatment to the catalyst precursors, and then using electrochemical synthesis of the supported catalysts to obtain composite catalysts with core-shell structures. By means of hydrothermal and then heat treatment combined with

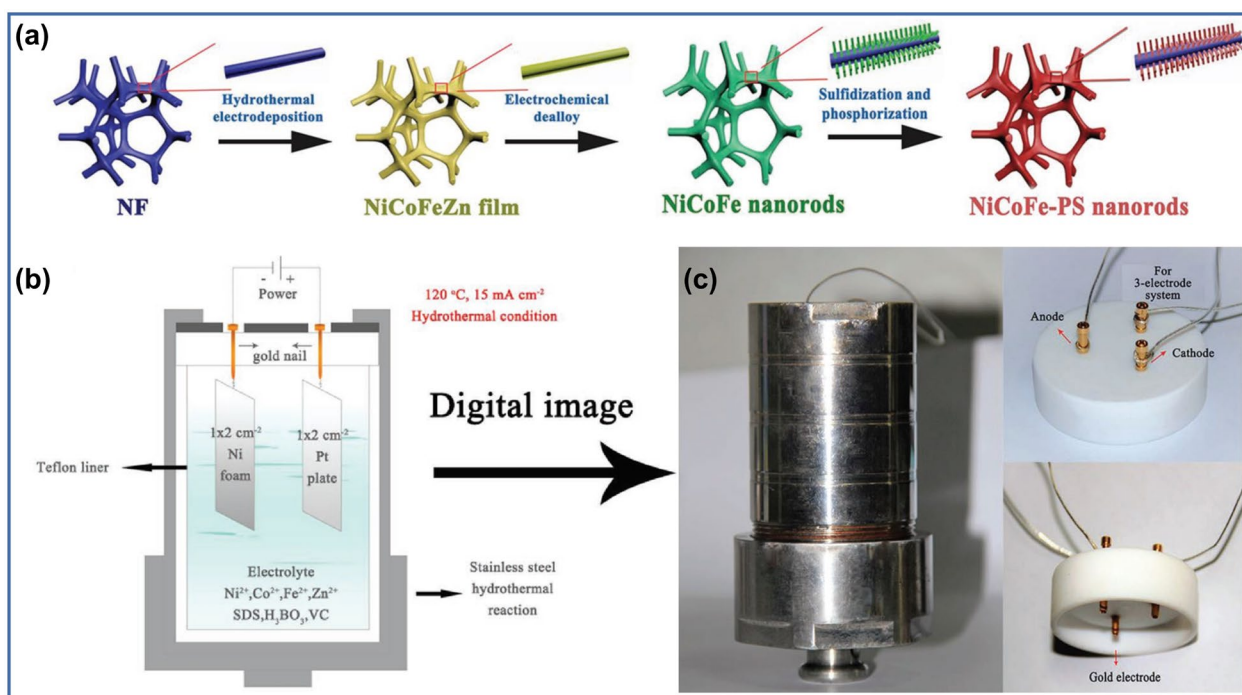


Fig. 6 (a) Schematic illustration of the growth of NiCoFe-PS nanorods/NF. The (b) diagram and (c) digital images of the hydrothermal electrodeposition device⁹⁹. Copyright 2019, Wiley-VCH.

electrodeposition, Zhao *et al.*⁹⁵ prepared a composite high efficiency overall water splitting catalyst NiFe-LDH/NiCo₂O₄/NF with a core-shell structure. Lou *et al.*⁹⁶ first coelectrodeposited bimetallic (Ni, Co) hydroxide precursors on an NF substrate and then thermally converted them into spinel mesoporous NiCo₂O₄. The prepared NiCo₂O₄ ultrathin nanosheets with particle sizes between 2–5 nm supported on NF have fast electron and ion transport, a large electroactive surface area, and excellent structural stability.

3.4.5 Electrochemical synthesis and electrochemical treatment

Electrochemical treatment usually employs electrochemical methods to oxidize, reduce, and redox the material surface, which is a strong and fast material surface treatment method, and the treatment intensity can be controlled by adjusting the voltage, current, and treatment time. The commonly used electrochemical methods are galvanostatic methods, potentiostatic methods, and cyclic voltammetry, including constant current/potential oxidation, constant current/potential reduction, and cyclic voltammetry redox. The electrochemical treatment method is often combined with electrochemical synthesis to prepare nanoscale core-shell catalysts in situ on conductive metal substrates (such as NF, Cu foam, and Cu plates). As illustrated in Fig. 5a, Sun's group successfully obtained the high-efficiency oxygen evolution catalyst CS-NiFe_{0.10}Cr_{0.10} with core-shell structures by adopting the constant current oxidation, heat treatment, constant potential reduction, and electrodeposition methods⁹⁷. Ren *et al.*⁹⁸ chemically oxidized Cu foam and then calcinated and reduced it at the constant potential to obtain Cu nanowires supported by Cu foam. Finally, a Cu@NiFe LDH bifunctional catalyst with a core-shell structure was obtained *via* electrodeposition (Fig. 5b).

3.4.6 Hydrothermal-electrosynthesis

Hydrothermal electrosynthesis is a new type of catalyst synthesis strategy that has been developed in recent years, in which hydrothermal reactions and electrosynthesis reactions are performed at the same time. Compared with traditional electrosynthesis at normal pressure and temperature, materials prepared by hydrothermal electrosynthesis have much better crystallinity and stronger bonds between the catalyst and substrate. Additionally, composites prepared by this method show a rough surface with a large surface area. Hydrothermal electrodeposition was reported by Komarneni *et al.*⁹⁹ for the first time to synthesize quaternary alloy films. They fabricated a NiCoFe-PS nanorod/NF catalyst by hydrothermal electrodeposition and in situ electrochemical dealloying followed by a process for P/S cotreatment, and the growth of the NiCoFe-PS nanorod/NF is illustrated in Fig. 6a. Fig. 6b is a schematic of the designed hydrothermal-electrodeposition device, while Fig. 6c shows the corresponding digital images of the hydrothermal-electrodeposition device. The NiCoFe-PS nanorod/NF can reach 10 mA cm⁻² at a small overpotential of 195 mV with a Tafel slope of 40.3 mV dec⁻¹ for the OER and 97.8 mV with 51.8 mV dec⁻¹ for the HER. Thus, this bifunctional catalyst shows the low potentials of 1.52 and 1.76 V at 10 and 50 mA cm⁻² toward overall water splitting with excellent stability for over 200 h, which are results superior to most recent nonnoble metal-based bifunctional electrocatalysts. The Komarneni group also fabricated 3D mesoporous Ni₃S₂ nanosheet/NF catalysts *via* hydrothermal electrodeposition and in situ electrochemical dealloying followed by sulfuration¹⁰⁰. The mesoporous Ni₃S₂ nanosheets/NF exhibited a highly mesoporous structure with a specific surface area of 60.1 m² g⁻¹ and showed a low overpotential of 223 mV at 10 mA cm⁻² with a small Tafel slope of 60.5 mV dec⁻¹. The superior catalytic property could be ascribed to the rational

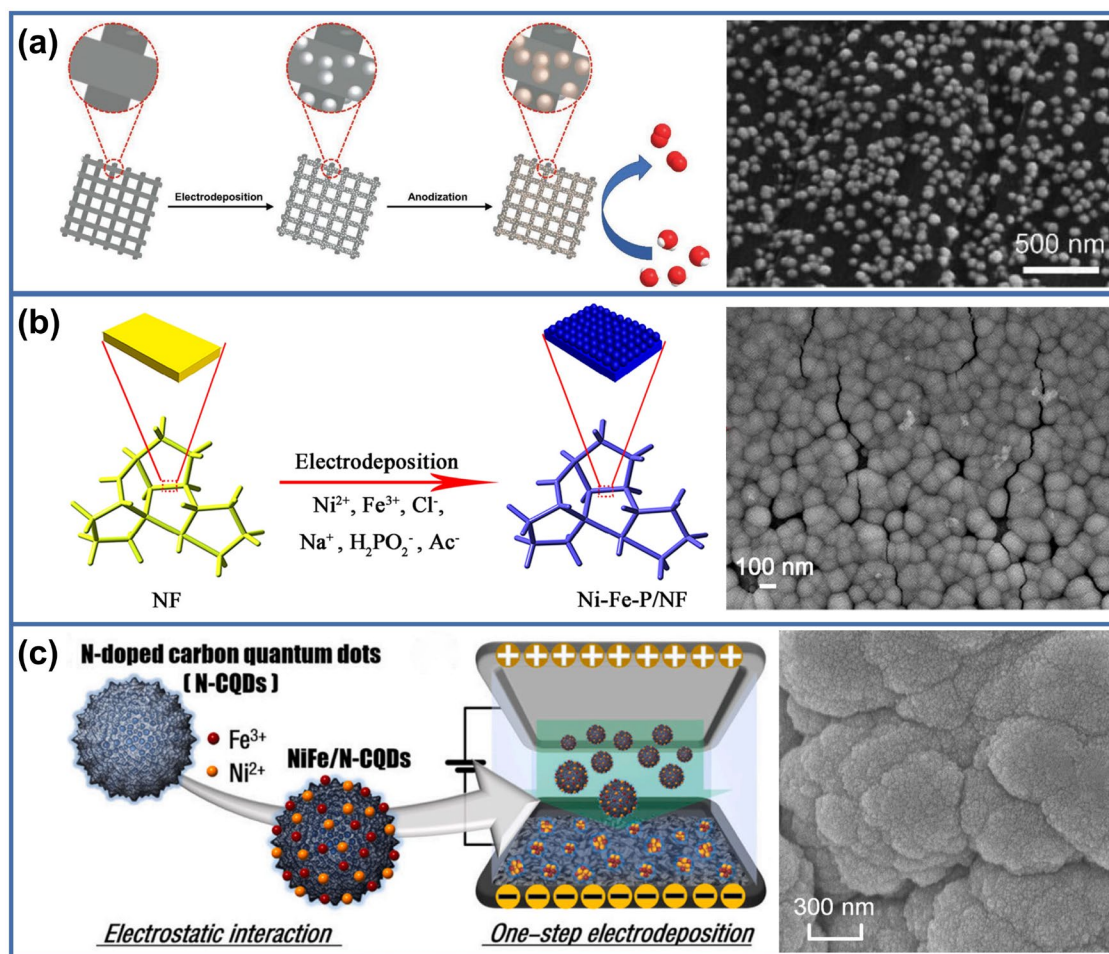


Fig. 7 Electrochemical synthesis of low-dimensional nanoparticles. (a) Schematic illustration of the electrochemical strategy to fabricate the core-shell nanospheres and the OER catalytic function¹⁰⁷. Copyright 2020, Wiley-VCH. (b) Schematic illustration of the fabrication process of Ni-Fe-P/NF¹⁰⁸. Copyright 2019, Elsevier. (c) Illustration of the one-step cathodic electrodeposition process for preparing the NiFeOx@NC hybrid¹¹⁰. Copyright 2020, Elsevier.

synthetic process, morphology-controlled mesoporous structure, and highly exposed active sites. The hydrothermally driven electrodeposition method showed significant advantages toward the OER, as follows: (1) due to the high temperature, the gas generated on the cathode overflows faster; both the gas generated on the cathode and the hydrothermal conditions impacted the coating surface; hence, the film possessed more active sites to improve the OER properties; and (2) the hydrothermal conditions improved the crystallization of the coating, leading to excellent electrode stability under the OER test¹⁰¹.

4. Structural design of transition metal-based catalysts for electrochemical synthesis

In recent years, nanostructured transition metal-based electrocatalysts have attracted increasing attention because of their remarkable electrocatalytic performance. In addition to the chemical composition, the catalytic efficiency and selectivity also depend on the shape, size, and even separation distance of the particles. As a mature and scalable technology, electrodeposition can provide tailor-made shapes or components for industrial needs.

Electrodeposition plays an important role in the preparation of various nanostructured catalysts^{102,103}. In this section, we will focus on the advantages of electrodeposition technology in morphology design. Compared with other strategies, the comprehensive electrodeposition variable is easy to operate. In addition, electrodeposition is not only able to accurately control the size, shape, composition, and structure of the electrode, but it can also improve the stability of the electrode through interface modulation. Therefore, various types of nanostructure transition metal-based catalysts with different morphologies have been prepared *via* electrodeposition, including low-dimensional nanoparticles, nanosheets, and nanofilm structures, 3D pores, nanowires, nanotube array structures, and hierarchical composite nanostructures.

4.1 Low-dimensional nanoparticles

Reducing the catalyst material size can significantly increase the ratio of surface atoms to bulk atoms, thus providing a relatively higher number of active sites. Therefore, compared with bulk materials, nanomaterials often show excellent electrocatalytic performance. In principle, a synthesis method that can produce fine grains can be

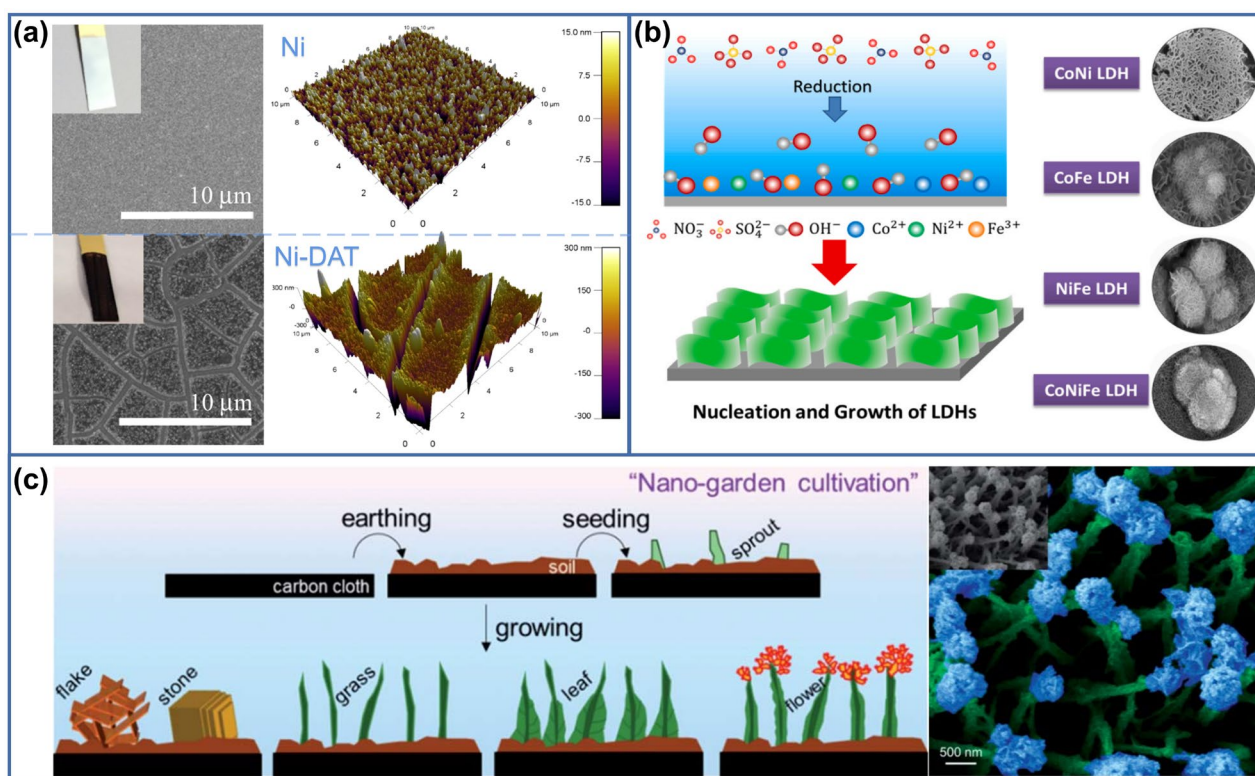


Fig. 8 (a) SEM and AFM images of Ni and Ni-DAT films electrodeposited on Au substrates ¹¹⁴. Copyright 2016, American Chemical Society. (b) Schematic of the preparation of LDHs nanosheets ¹¹⁶. Copyright 2021, Elsevier. (c) A schematic illustration of the steps of nanogarden cultivation process on carbon cloth and a false color SEM image of CoP nanoflowers ¹²⁰. Copyright 2020, The Royal Society of Chemistry.

used in the production of nanomaterials. In the past few years, some important progress has been made in the electrodeposition of transition metal-based catalyst nanoparticles, such as NiO ⁷⁵, Co₃O₄ ¹⁰⁴, CoFeS ⁸⁰, Ni₂P ¹⁰⁵, and CoSe ¹⁰⁶.

4.1.1 Nanospheres and nanoparticles

Small-sized nanosphere and nanoparticle catalysts have relatively high numbers of active sites and can show outstanding turnover frequency at low catalyst loading, which greatly improves the material utilization. However, the synthesis processes of nanosphere and nanoparticle materials are complicated, and electrochemical synthesis is a simple and effective method for the preparation of nanoparticle materials developed in recent years. Luo *et al.* ¹⁰⁷ obtained NiFe_xSn@NiFe (oxy)hydroxide nanospheres with core-shell structures *via* a facile electrochemical strategy, including electrodeposition of NiFe_xSn alloy nanospheres on carbon cloth, followed by anodization (Fig. 7a). The alloy core of NiFe_xSn could promote charge transfer, and the amorphous shell of NiFe (oxy)hydroxide is defect-rich and nanoporous due to the selective electrochemical etching of Sn in the alkaline media. The optimized catalyst of NiFe_{0.5}Sn-A exhibits a remarkable OER performance with a low overpotential of 260 mV at 10 mA cm⁻², a small Tafel slope of 50 mV dec⁻¹, a high turnover frequency of 0.194 s⁻¹ at an overpotential of 300 mV, and robust durability. Lei's group successfully prepared amorphous Ni-Fe-P holey nanospheres on a 3D porous NF substrate by one-step electrodeposition (Fig. 7b) ¹⁰⁸. The as-prepared Ni-Fe-P/NF has the following features: a bimetallic (Ni and Fe) phosphide composition, amorphous holey structure, surface

superaerophobicity, and self-supportive configuration. Benefiting from these features, Ni-Fe-P/NF exhibits advanced OER catalytic performance with a low overpotential of 156 mV at 10 mA cm⁻², a small Tafel slope of 69 mV dec⁻¹, and prominent stability (>4000 cycles and 36 h), which are superior to other well-performing metal-phosphide catalysts reported and the commercial catalyst IrO₂.

4.1.2 Nanoclusters

Nanoparticle clusters have been proven to be excellent electrocatalysts due to the high number of active sites present on the surface. However, it has been reported thus far that the preparation of such nanoparticle-modified electrodes is highly challenging, usually requiring multistep chemical synthesis, purification, and embedding on the electrode surface; additionally, it is often performed at very high temperatures. Renjith *et al.* ¹⁰⁹ reported for the first time that cobalt nanoparticles were prepared by a one-step electrochemical method and deposited *in situ* on the surface of the electrode. The nanoparticle clusters are uneven in thickness, which varies between 20 and 90 nm. Although the loading of the catalyst was very low, the cobalt nanoparticles on dense graphite sheets exhibited a very low overpotential of 350 mV at 10 mA cm⁻². The turnover frequency of 0.78 s⁻¹ and activation energy of 21 kJ mol⁻¹ for the OER indicate that they are potential anodic catalysts for the OER in alkaline media. A NiFeOx cluster strongly coupled with N-doped carbon (NiFeOx@NC) was reported by Zhang *et al.* ¹¹⁰ *via* a one-step electrodeposition process in an aqueous solution containing Ni²⁺, Fe³⁺, and carbon quantum dots (Fig. 7c). The highly coupled interface between the subnano NiFeOx clusters and N-

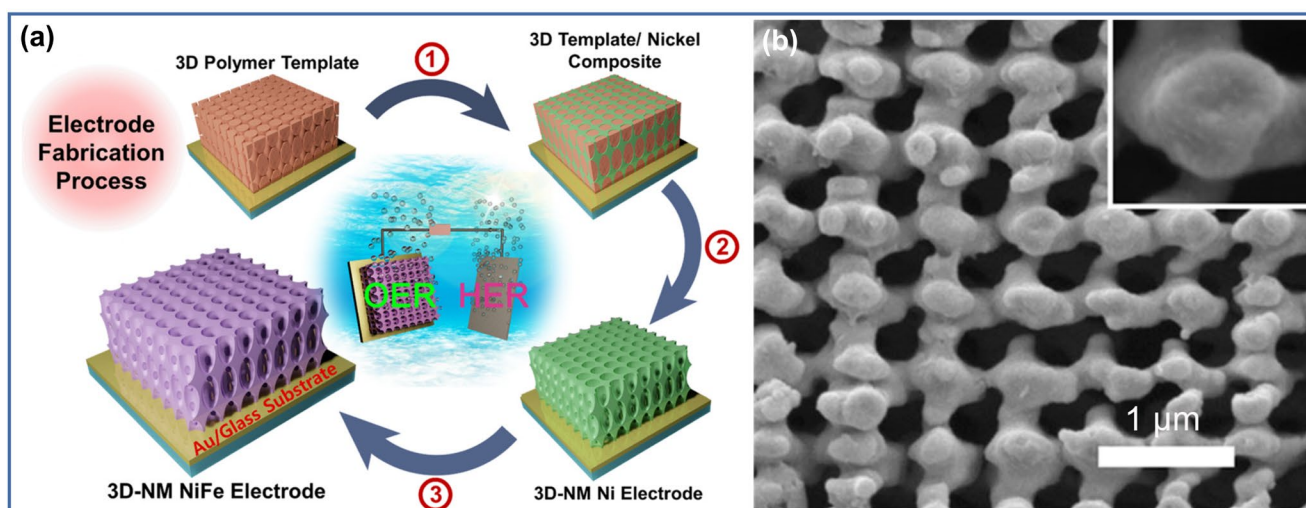


Fig. 9 (a) Illustration of the fabrication process for the Ni/Fe-decorated 3D-nanomesh nickel electrode. First, the 3D polymer template, which was made by the PnP method on a substrate of Au/glass, was filled with nickel by electrodeposition (1). Second, the 3D template was selectively removed, and a 3D nanomesh-like nickel (3D-NM Ni) electrode was obtained (2). Finally, NiFe hydroxide was further electrodeposited on the 3D-NM Ni electrode to produce the 3D-NM NiFe electrode (3). (b) SEM image and enlarged view of the 3D-NM Ni electrode¹²¹. Copyright 2018, Elsevier.

doped carbon resulted in an enhanced OER performance superior to that of commercial RuO₂ and IrO₂, as evidenced by its lower overpotential of 195 mV at 10 mA cm⁻² and faster kinetics (Tafel slope of 33 mV dec⁻¹), along with its excellent long-term durability, rate capability, and environmental adaptability.

4.2 Two-dimensional nanostructure

Benefiting from their large specific surface area and rich edges, two-dimensional (2D) nanostructures have rich electrochemically active sites. Inorganic compounds with 2D nanostructures (*e.g.*, single atom layers¹¹¹, nanosheets¹¹², and thin films^{7,113}) are key materials for various energy conversion devices. The preparation of high purity 2D compounds mainly relies on gas phase methods such as chemical vapor deposition, vacuum evaporation, and sputtering. However, these routes often require expensive equipment and complex energy-intensive processes. In contrast, bottom-up electrodeposition has obvious advantages in the preparation of thin film materials. Since the interdiffusion is minimized by the lower processing temperature, uniform thin films can be deposited on diverse substrates with various shapes. By simply changing the charge transport, the thickness of the film and the nanosheets can be accurately controlled.

4.2.1 Nanofilms

The nanofilm structures are closely attached to the conductive substrate and can show excellent OER catalytic activity with low loading. The thickness and roughness of nanofilms can be controlled by adjusting the electrodeposition time and electrolyte composition. Gewirth *et al.*¹¹⁴ developed a simple method that makes Ni, Co, and NiFe films exhibit fractal-like behavior with nanosized clusters by using 3,5-diamino-1,2,4-triazole (DAT) as an additive in the metal electrodeposition processes (Fig. 8a). The NiFe-DAT electrodeposited by this method exhibited very high activity for the OER, that is, high current densities (100 mA cm⁻²), high mass activity (~1200 A g⁻¹ of catalyst), high stability (>72 h), and low overpotential (~300 mV). Equally important, they found that they could partially tune this

activity by changing the amount of metal electrodeposited. The effect was essentially independent of the substrate. The origin of this high activity is fractal-like behavior, *i.e.*, film roughness, that is caused by inhibition of electrodeposition by the DAT additive. Peng and coworkers employed a two-step electrodeposition method to prepare a series of nanofilm electrodes containing Ni, Co, P, and Se on carbon cloth¹¹⁵. After a suitable electrochemical activation process through cyclic voltammetry, the resultant binder-free NiCoP-NiCoSe₂ nanobilm films were transformed from compact layer(s) to porous nanoparticle films composed of NiCo hydroxides and a small amount of NiCo oxyhydroxides and, thus, exhibited striking electrocatalytic activity (the overpotential of 243 mV at 10 mA cm⁻²) and excellent stability (80 h) for the OER. The rougher surface, well-suited electronic structure originating from Ni/Co cooping, and the rational integration of NiCoP and NiCoSe₂ are important factors contributing to the excellent OER performance of the NiCoP-NiCoSe₂ film after the electrochemical activation process.

4.2.2 Nanosheets

2D nanosheet arrays can provide a high electrochemically active surface area and good mechanical strength, and the gas products can be easily diffused in the catalytic process. The construction of nanosheet arrays on conductive substrates is an effective way to obtain catalysts with high OER performance because of their high specific surface area, enhanced mass diffusion, and low interfacial resistance between catalysts and collectors. Wen *et al.*⁵⁹ directly grew nanosheet arrays of single-phase Co₃O₄, NiO, and Co₃O₄/NiO nanocomposites on carbon cloth *via* electrodeposition. The composition can be finely tuned by changing the Ni²⁺/Co²⁺ ratio in the electrodeposition solution. The thickness and plane size of the nanosheets can also be well controlled. The effects of size, composition, and phase on the OER activity were investigated in detail. The results indicated that the optimized Co₃O₄ nanosheet arrays further coated with a NiO layer achieved an enhanced OER activity. Shinde's group developed hierarchical nanosheet-based

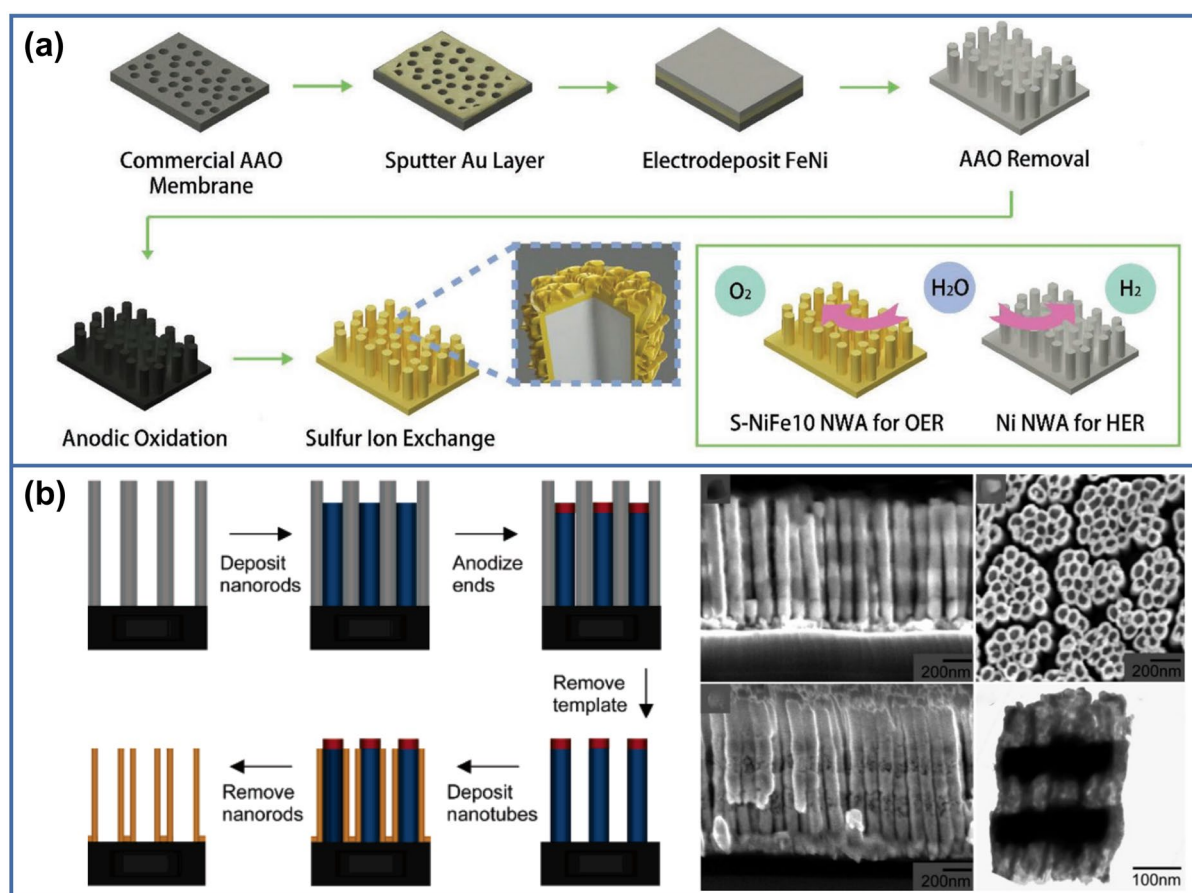


Fig. 10 (a) Schematic illustration of the fabrication process for NiFe nanowire arrays and surface sulfurized NiFe nanowire arrays¹²⁵. Copyright 2019, Wiley-VCH. (b) Schematic illustration of the method used to fabricate nanotube arrays on substrates and SEM images of segmented nanostructures¹²⁷. Copyright 2005, American Chemical Society.

ternary CoNiFe LDH thin films *via* an inexpensive and facile electrodeposition method (Fig. 8b)¹¹⁶. As an electrocatalyst, CoNiFe LDH demonstrated excellent performance in the OER, affording an overpotential of 196 mV at 10 mA cm⁻² with a Tafel slope of 49 mV dec⁻¹. Additionally, it exhibited excellent catalytic stability with stable operation for over 10 h at 10 mA cm⁻². He *et al.*¹¹⁷ reported a template-free and annealing-free one-step electrodeposition approach for the in situ fabrication of composition- and morphology-controllable Ni_xFe_{3-x}O₄/Ni hybrid and Ni_xFe_{3-x}O₄ nanosheet arrays (NSAs) on different conducting substrates as highly active and robust oxygen-evolving electrocatalysts. Benefiting from the 2D/3D hierarchical NSA morphology with a high ECSA, the regulated Fermi energy of Ni_xFe_{3-x}O₄ toward the O₂ production potential by Ni incorporation, and the low resistance and good contact at the catalyst/substrate interfaces, the obtained Ni_xFe_{3-x}O₄/Ni hybrid NSAs exhibited excellent catalytic performance toward the OER.

4.2.3 Nanoflower

The nanoflower structure has a larger specific surface area, which is beneficial to the adsorption of intermediate products and the desorption of oxygen, and the petal-like morphology can expose more edge defects and greatly increase the active sites of the catalyst¹¹⁸. Kuila *et al.* electrodeposited iron sulfide on a conductive NF substrate by changing the electrodeposition time, electrolyte pH value, and deposition potential¹¹⁹. The obtained coating with a

nanoflower structure was Ni-doped O-doped O-incorporated iron sulfide with FeS₂ lattice domains, which exhibited outstanding OER performance. The superior electrocatalytic activity of the electrodeposits could be attributed to the (i) morphological openness of the electrodeposits, which provided better accessibility of the active species to the active site and (ii) better charge transfer efficiency across the electrode-electrolyte interface. By simply manipulating (electro)chemical gradients using a combined hydrothermal and electrodeposition strategy, Yan *et al.*¹²⁰ showed the controlled growth of Co(OH)₂ nanostructures, mimicking the process of garden cultivation (Fig. 8c). The resulting “nano garden” can produce different patterns, all of which can be fully phosphidated into CoP without the loss of structural integrity. Remarkably, these CoP nanostructures showed distinct catalytic performance in oxygen evolution and hydrogen evolution reactions. Under universal pH conditions, the CoP “soil+flower-with-stem” structure showed a much more “effective” surface area for gas-evolving reactions with lower activation and concentration overpotentials.

4.3 Three-dimensional nanocomposite structure

Traditional powder electrocatalysts must be combined with conductive and binding agents to maintain good adhesion and establish a channel for charge transfer. By combining a variety of low-dimensional materials, continuous interconnected conductive 3D

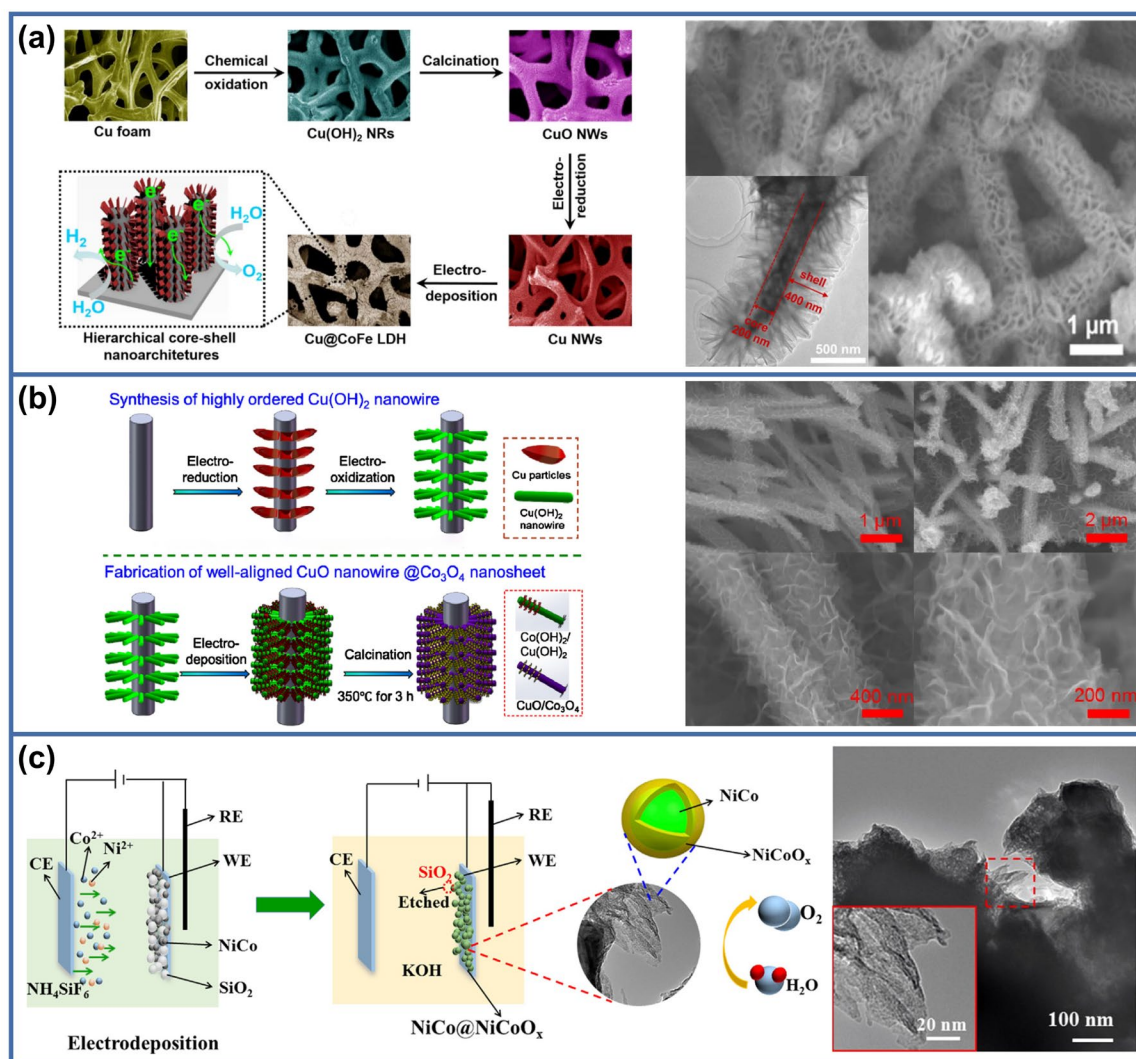


Fig. 11 (a) The fabrication process of Cu@CoFe LDH core-shell nanostructure electrocatalysts, and SEM images of Cu@CoFe LDH (the inset is the transmission electron microscope (TEM) image) ⁷¹. Copyright 2017, Elsevier. (b) Schematic diagram illustrating the formation mechanisms of Cu(OH)₂ nanowires and CuO@Co₃O₄ core-shell heterostructures and SEM images of CuO nanowire@Co₃O₄ nanosheet composites at different magnifications ⁷⁴. Copyright 2017, Elsevier. (c) Schematic illustration of the preparation of the nanostructured NiCo@NiCoO_x core-shell layer for the OER, and TEM images of the as-prepared nanostructured NiCo@NiCoO_x core-shell layer ¹²⁹. Copyright 2017, Elsevier.

electrodes can be constructed. In particular, hollow 3D structures have attracted great attention because of their rich internal space and large surface area, which are conducive to rapid diffusion and enhance the dynamics of the OER. Electrodeposition is one of the most suitable methods for the preparation of 3D electrode materials. The nanostructures of 3D transition metal-based catalysts synthesized by electrochemical strategies can be divided into the following types: hierarchical porous structures, nanowire arrays, nanotube arrays, and core-shell composite structures. Most of these materials can be electrodeposited by the template method.

4.3.1 Hierarchical nanoporous structure

A 3D porous structure without a binder can be used to improve the electrocatalytic activity by increasing the accessible area and electrochemically active sites. In addition, the cross-linked structure provides richer and shorter transfer channels for electron transport and ion diffusion, thus improving the conductivity of the catalyst.

Electrodeposition is a powerful alternative to the preparation of catalysts. The catalyst electrodeposited on the substrate can be used as an electrode, and its composition and pore structure can be designed by controlling the electrodeposition conditions, such as the current density and solution composition. As shown in Fig. 9a, Park's group reported a 3D ordered nanoporous nickel electrode synthesized with a thickness of 5 μm by using a templating method composed of proximity field nanopatterning (PnP) and electrodeposition followed by the introduction of NiFe(OH)₂ on the nickel electrode to increase the OER activity ¹²¹. The unique nanopore array structure of the electrode had the advantages of not only an enlarged active surface area but also the fast removal of oxygen bubbles by the spatial confinement effect (Fig. 9b). Consequently, the NiFe-decorated 3D ordered nanoporous nickel electrode exhibited a highly efficient oxygen-evolving ability with a turnover frequency of 2.9 s⁻¹ and an ultralong durability of 300 h. Tu

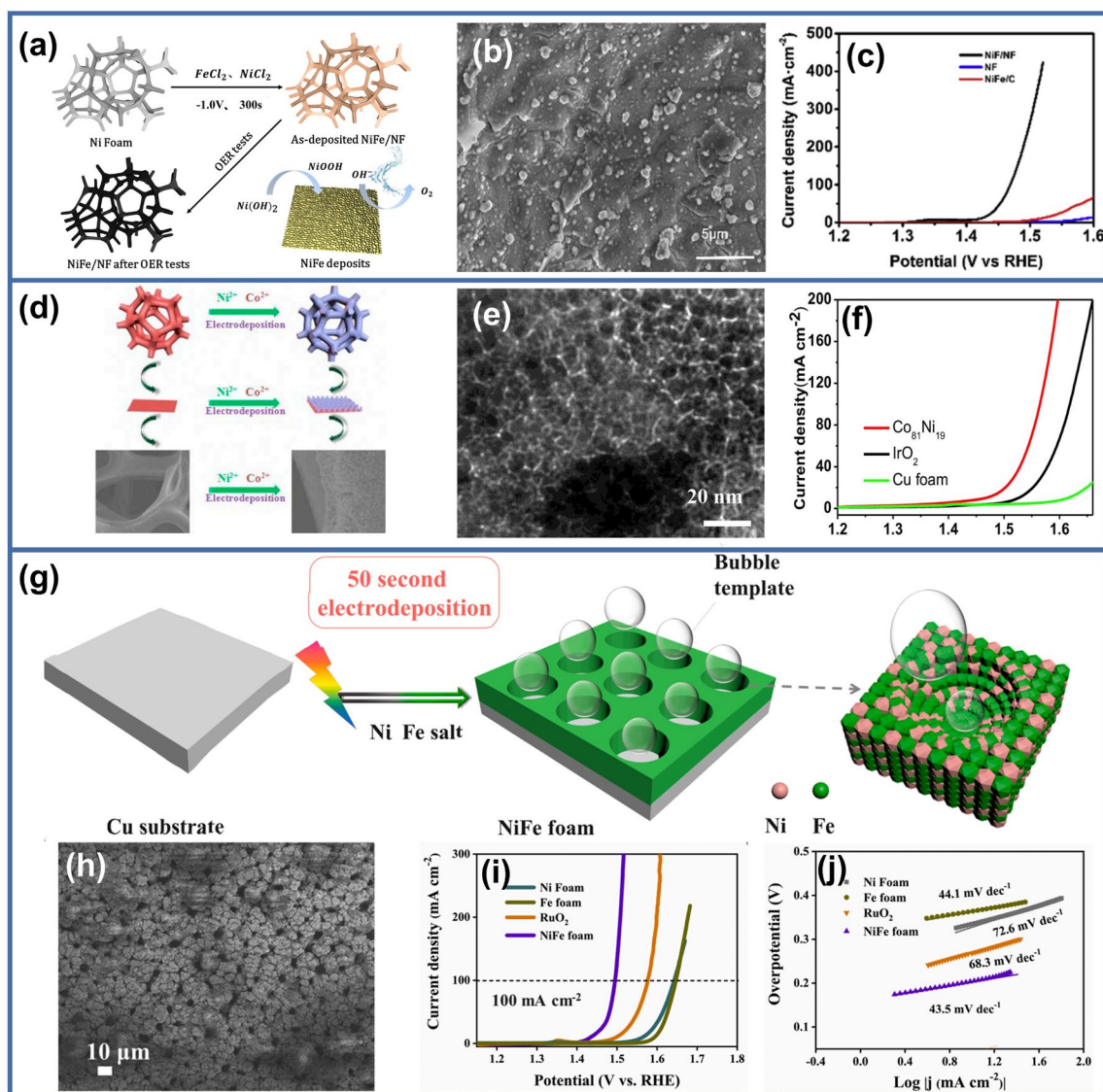


Fig. 12 (a) Scheme for the synthesis of the NiFe/NF hierarchical electrocatalyst for oxygen evolution measurements. (b) SEM image of as-deposited NiFe/NF. (c) Linear sweep voltammetry at a scan rate of 2 mV s^{-1} with 90% iR compensation in 1 M KOH of as-deposited NiFe¹³¹. Copyright 2019, Elsevier. (d) An illustration of the synthetic process for the preparation of 3D freestanding porous Cu foam in situ armored CoNi alloy nanosheet arrays through the electrodeposition process. (e) HRTEM image of CoNi@CF. (f) LSV plots obtained from Co₈₁Ni₁₉@CF, IrO₂ and Cu foam for the OER in 1.0 M KOH at 5 mV s^{-1} ¹³². Copyright 2019, Elsevier. (g) Schematic diagram of the synthetic route of NiCo and NiFe foams by an ultrafast electrodeposition method. (h) SEM images of NiFe foam. LSV curves (i) and the corresponding Tafel plots (j) of the transition metal foams¹³³. Copyright 2021, Elsevier.

*et al.*¹²² developed free-standing 3D nickel arrays with a cross-linked porous structure as high-performance electrocatalysts for the OER *via* a facile one-step electrodeposition strategy. The 3D nickel arrays were strongly anchored on the substrate, forming self-supported electrocatalysts with reinforced structural stability and high electrical conductivity. Benefitting from their increased active surface area, abundant channels for electron/ion transportation, and enhanced electronic conductivity, the designed 3D nickel arrays exhibited remarkable electrocatalytic OER performance.

4.3.2 Nanowires and nanotubes arrays

Nanowire array catalysts have open fiber space structures, which facilitate electrolyte penetration and ion diffusion, favor the

adsorption and desorption of oxygen evolution intermediates, minimize the dead volume and increase the active surface area of the catalysts^{123,124}. As illustrated in Fig. 10a, Lu *et al.* fabricated NiFe/(Ni,Fe)₃S₂ core/shell nanowire arrays *via* anodic aluminum oxide membrane templated electrodeposition followed by sulfur ion exchange, which was an outstanding catalyst for electrolytic water splitting¹²⁵. Nanowire array-based electrodes, which offer extended reaction surface areas and 1D guided charge transport and mass transfer, proved to be a promising new catalyst architecture design for electrocatalytic processes.

In different nanostructures, nanotube array catalysts have the advantages of low series resistance, high stability, easy diffusion of

reactants, and exposure to rich active centers, and they show great potential in catalytic OERs¹²⁶. Sander's group designed a double-templating approach using simple electrochemical methods to create aligned arrays of nanotubes on substrates, as shown schematically in Fig. 10b¹²⁷. First, nanoporous templates were constructed by anodizing aluminum films that had been evaporated onto silicon substrates. Parameters such as the pore diameter, spacing, height, and ordering were tuned by varying the anodization conditions. Next, nickel nanorods were electrodeposited into the pores of the alumina. After deposition, the exposed ends of the nanorods were modified *via* anodization in a dilute KOH solution to prevent further deposition. Then, through selective chemical etching, the alumina template was removed, resulting in an array of nickel nanorods with anodized tips remaining. The nanotube material deposited uniformly across the entire surface of the nanorod arrays, except at the anodized tips of the nanorods, finally, through the selective removal of the nickel nanorod array template, an array of open-ended nanotubes formed on the substrate.

4.3.3 Core-shell composite nanostructure

Regardless of the nanostructure or local electronic structure, nanostructural regulation can significantly affect the catalytic activity of the catalyst. The construction of catalysts with core-shell composite nanostructures has been proven to be an effective way to expose and improve active sites¹²⁸. A well-designed internal catalyst interface can promote the charge transfer process in the catalytic reaction. As shown in Fig. 11a, Chen and coworkers combined 1D Cu nanowires (NWs) and 2D CoFe LDH nanosheets (NSs) to fabricate a novel hierarchical core-shell nanoarchitecture on Cu foams (Cu@CoFe LDH) for efficient water splitting⁷¹. The rational design of the hierarchical core-shell nanostructure endows the composite with a large surface area and accessibility to active sites, which are beneficial for the adsorption of water molecules and catalytic reactions. Additionally, the unique layered structure of CoFe-LDH NSs is favorable for the diffusion of water molecules and release of gas products, ensuring intimate contact between the catalyst and electroactive species. In addition, the Cu NW cores provide highways for electron transport, decreasing the electron transport distance and barrier and facilitating the reaction kinetics. Benefiting from these superiorities, the Cu@CoFe LDH core-shell catalysts exhibit remarkable performance for overall water splitting in alkaline media. Guan *et al.*⁷⁴ successfully fabricated well-aligned CuO nanowire@Co₃O₄ nanosheets on carbon fibers *via* multistep electrodeposition combined with thermal treatment and applied them as binder- and conductive-agent-free anodes for the OER in a water electrolysis process (Fig. 11b). Such an anode reveals an overpotential of 258 mV at 10 mA cm⁻² in a 1.0 M KOH solution, which is much lower than that of pure CuO nanowire- or Co₃O₄ nanosheet-based electrodes. This is attributed to the smart hybridization of CuO nanowires and Co₃O₄ nanosheets into a hierarchical core/shell array configuration, which could largely increase the contact areas between the electrolyte and active sites. In addition, the Cu²⁺ in the CuO/Co₃O₄ composite was oxidized to Cu³⁺ components during the OER process, which should serve as new catalytic active sites for the OER. Zheng's group successfully constructed a nanostructured NiCo@NiCoO_x core-shell layer on a stainless steel disk for the OER in an alkaline solution¹²⁹. First, a NiCo-

SiO₂ composite film was electrocodeposited from a solution containing (NH₄)₂SiF₆, NiSO₄, and CoSO₄. Then, the as-prepared composite film was scanned continuously by CV in a concentrated alkaline solution. The SiO₂ template was etched, and the NiCo component was activated during this process, resulting in the generation of a NiCoO_x shell (Fig. 11c). The results indicated that this nanostructured NiCo@NiCoO_x core-shell layer can provide a current density of 100 mA cm⁻² in 1.0 M KOH at a low overpotential of 337 mV and exhibits good stability toward water oxidation. The outstanding OER performance is attributed to the unique metal-oxide/hydroxide core-shell structure, which allows high electrical conductivity in the core and high catalytic activity on the shell.

5. Classification of transition metal-based OER electrocatalysts for electrochemical synthesis

In the past few decades, transition metal-based OER electrocatalysts have aroused great research interest, and great scientific progress has been made¹⁴. We will focus on the latest progress in the electrochemical synthesis of transition metal-based (mainly Fe, Co, and Ni) OER electrocatalysts, which are divided into metals/alloys, oxides, hydroxides, sulfides, phosphides, selenides, and other transition metal compounds in this section. The electrocatalytic mechanism, electrocatalytic performance, structure characterization, and catalytic mechanism are discussed in detail.

5.1 Metals/alloys

Transition metal-based electrocatalysts in the pure metal state cannot survive directly in harsh electrolytes such as acidic and alkaline media because of the strong corrosion effect. Therefore, whether in monometal or alloy states, they are usually embedded in or decorated with relatively stable substrates (such as carbon materials, NF, and Cu foam)¹³⁰. As shown in Fig. 12a, Hang *et al.*¹³¹ prepared a highly efficient NiFe alloy OER electrocatalyst using NF as the substrate *via* one-step electrodeposition. To obtain NiFe with high roughness and a large specific surface area, chlorides of Ni and Fe were employed to replace commonly used Ni and Fe sulfate. The deposited NiFe/NF can be directly used in the OER without further treatment, such as adding a binder or conductive film (Fig. 12b). Furthermore, the transition from NiFe alloy to NiFe hydroxide was observed during the catalytic reaction and showed high OER efficiency (Fig. 12c). The NiFe alloy ensures its electrical conductivity and connection with the NF substrate. The deposited NiFe/NF has a lower initial potential and overpotential with a smaller Tafel slope and charge transfer resistance. Chen's group fabricated 3D freestanding porous Cu foam in situ armored CoNi alloy nanosheet arrays with tunable compositions *via* a facile and cost-efficient electrodeposition strategy (Fig. 12d)¹³². And the HRTEM image (Fig. 12e) shows the CoNi alloy nanosheet is highly porous and is composed of numerous small nanoparticles. The electrochemical measurements demonstrated that the catalytic activity of CoNi@CF was strongly dependent on the atomic ratio of Co/Ni. The optimized Co₈₁Ni₁₉ catalyst showed excellent electrocatalytic performance with an overpotential of 240 mV at 10 mA cm⁻² in an alkaline medium, which exceeded that of the IrO₂ catalyst (Fig. 12f). This could benefit from the ordered nanosheet array and interconnected porous structure, the high specific surface area, and the synergistic effect of the CoNi alloys. Yu *et al.*¹³³ reported an ultrafast one-step

electrodeposition method to prepare a series of transition metal foams within one minute for electrocatalytic water splitting (Fig. 12g). Porous metal foams not only possess unique 3D channels for

Most metals can be electrodeposited directly on the cathode, and when the current passes through the metal salt solution, metal oxides tend to be produced on the anode. In electrochemical

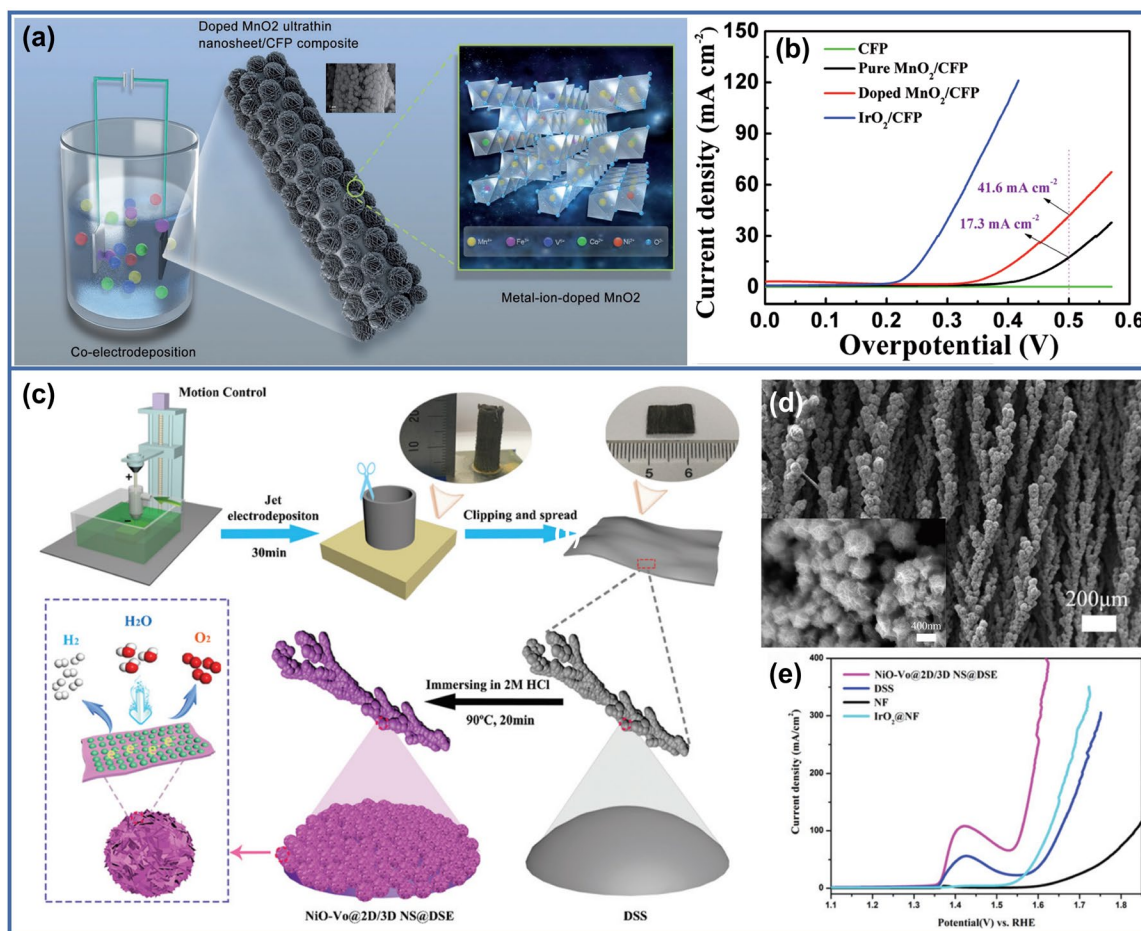


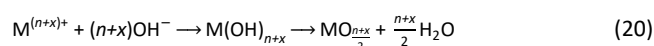
Fig. 13 (a) Schematic representation of the preparation of the metal-ion (Fe, V, Co, and Ni)-doped MnO₂ ultrathin nanosheet/CFP composite. (b) LSV curves of the CFP, metal-ion-doped MnO₂ ultrathin nanosheet/CFP and IrO₂/CFP composite electrodes measured in 1 M KOH with a scan rate of 5 mV s⁻¹.¹⁴⁴ Copyright 2017, Wiley-VCH. (c) Schematic illustration of the DSS and in situ growth of 2D/3D NiO nanospheres on the DSS surface. (d) Scanning electron microscopy (SEM) image of NiO-Vo@2D/3D NS@DSE. (e) Polarization curve for the OER.⁷⁵ Copyright 2019, The Royal Society of Chemistry.

rapid electrolyte diffusion and gas release but also have robust integrated structures with enhanced conductivity for efficient charge transport (Fig. 12h). Consequently, NiFe foams exhibit excellent catalytic performance, i.e., only 206 mV to output 10 mA cm⁻² for the OER in 1 M KOH (Fig. 12i, j).

5.2 Transition metal-oxides

Transition metal-based oxides have attracted great attention in the field of electrocatalysis because of their advantages, which include affordable prices, strong reversibility, adjustable structures, and stable performance.^{3,21,134} By controlling the morphology and composition, tuning the electronic structure via external metal doping, and integrating hybrid structures into composites, efficient oxide-based OER electrocatalysts can be effectively fabricated.^{135,136} In this section, we will briefly introduce some recently reported transition metal-based oxide OER electrocatalysts, which include single metal oxides (mainly Co, Ni, and Mn oxides), spinel oxides, and perovskite oxides.

oxidation, metal ions in a lower oxidation state can be oxidized to a higher oxidation state on the anode. The higher oxidation state is prone to hydrolysis to form metal oxides or hydroxides¹³.



These routes have been used to synthesize oxides such as Co₃O₄,¹³⁷ ZnMn₂O₄,¹³⁸ PbO₂,¹³⁹ MnO₂,¹⁴⁰ and V₂O₅.¹⁴¹

5.2.1 Single metal oxide

The OER activities of single transition-metal-based oxide electrocatalysts rely on the metal types, metal oxidation states, morphologies, and substrates.¹⁴² Additionally, their applications in OERs are greatly hindered by poor conductivity. To solve the problem of poor conductivity, several strategies have been developed, including manipulating the structure and composition of oxides by doping heteroatoms, introducing oxygen vacancies, and forming polymetallic oxides.¹⁴³

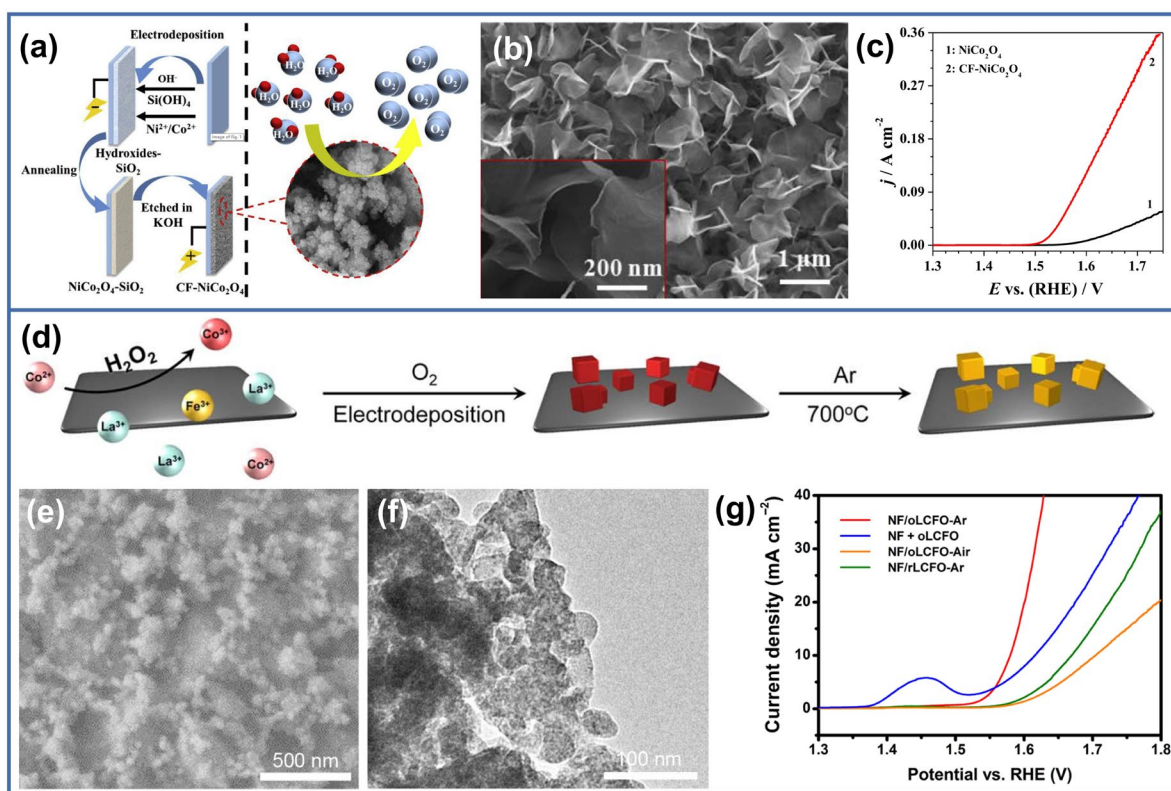


Fig. 14 (a) Schematic illustration of the preparation procedure for the CF-NiCo₂O₄ film. (b) SEM images of CF-NiCo₂O₄. (c) Quasi-steady state polarization of the NiCo₂O₄ and CF-NiCo₂O₄ films¹⁴⁶. Copyright 2017, Elsevier. (d) In situ fabrication of the NF/oLCFO-Ar hybrid through electrodeposition coupled with the oxygen reduction reaction and cobalt Fenton process, followed by calcination under Ar protection. (e) SEM image of NF/oLCFO-Ar. (f) TEM image of NF/oLCFO-Ar. (g) LSV profiles of NF/oLCFO-Ar, NF+oLCFO, NF/oLCFO-Air, and NF/rLCFO-Ar¹⁵¹. Copyright 2016, American Association for the Advancement of Science.

Transition single metal oxides such as Co₃O₄ and NiO are promising candidates for OER catalysts because of their high intrinsic activity and good stability. The construction of nanoarrays on conductive substrates is an effective way to obtain high OER performance because they have high specific surface areas, enhanced mass diffusion, and low interfacial resistance between catalysts and collectors. To achieve these advantages, it is necessary to effectively control the composition, phase structure, and size of the nanoarray. Wen *et al.*⁵⁹ directly grew nanosheet arrays of single-phase Co₃O₄, NiO, and Co₃O₄/NiO nanocomposites on carbon cloth *via* electrodeposition. By changing the proportion of Ni²⁺/Co²⁺ in the bath, the composition, thickness, and plane size of the nanosheets can be well controlled. The optimized Co₃O₄ nanosheet arrays were further coated with a NiO layer to achieve higher OER activity. Ye's group fabricated metal-ion (Fe, V, Co, and Ni)-doped MnO₂ ultrathin nanosheets on carbon fiber paper by employing a facile anodic coelectrodeposition strategy (Fig. 13a)¹⁴⁴. A high density of nanoclusters is observed on the surface of the carbon fibers consisting of doped MnO₂ ultrathin nanosheets with a thickness of ~5 nm, confirming that the metal ions (Fe, V, Co, and Ni) are doped into MnO₂, thus improving the conductivity of MnO₂. The overpotential of the doped MnO₂ composite electrode at 10 mA cm⁻² is much lower than that of the pure electrode, exhibiting better catalytic performance for the OER (Fig. 13b). As illustrated in Fig. 13c, Zhang *et al.*⁷⁵ reported a novel and simple synthesis route for a

dendritic self-supported electrode consisting of oxygen vacancy-rich NiO embedded within ultrathin 2D/3D nanostructures (NiO-Vo@2D/3D NS@DSE) for overall water splitting for the first time. Based on simple compound synthesis *via* jet electrodeposition and in situ acid etching, 2D nanosheets adhering uniformly to 3D nanospheres were successfully obtained on a dendritic self-supported skeleton surface (Fig. 13d). The results of the experiments and DFT indicate that this electrode integrates the following advantages: numerous active sites, intrinsic catalytic activity, good electrical conductivity, and outstanding reaction kinetic performance. Furthermore, this electrode exhibits an outstanding overpotential of 230 mV to deliver a current density of 10 mA cm⁻² for the OER (Fig. 13e).

5.2.2 Spinel oxides

Spinel oxide series have attracted much attention due to their excellent catalytic performance, high charge transfer efficiency and high stability in harsh alkaline media, and high anodic potential²⁶. Spinel oxides have a general formula of AB₂O₄, where cationic A²⁺ occupies the center of a tetrahedral unit, and B³⁺ is located in the octahedral position. As bimetallic oxides for the OER, the most studied spinel oxides, including MCo₂O₄ and MFe₂O₄ (M represents other transition metals), tend to exhibit better OER electrochemical performance than single metal oxide catalysts. The introduction of oxygen vacancies into OER electrocatalysts is an effective route to promote their catalytic performance.

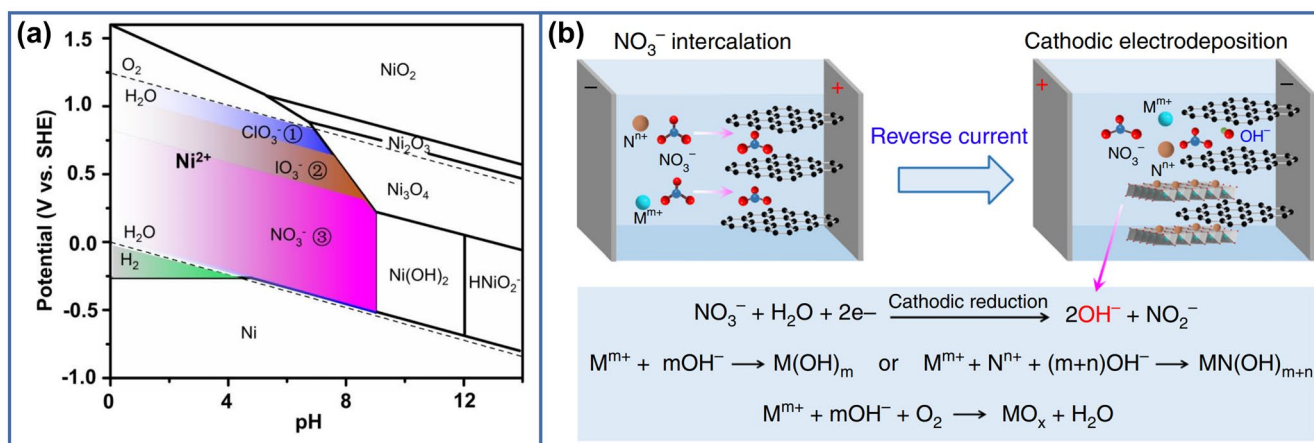


Fig. 15 (a) Pourbaix diagram of Ni-based species. The colored regions correspond to the oxoanion reactions that can be applied for the synthesis of nickel hydroxides. (b) Schematic illustration of the reaction mechanisms of the cathodic electrodeposition of metal (hydro)oxides, as well as the interface engineering process. M^{m+} and N^{n+} are metal cations¹². Copyright 2018, Springer Nature.

Li *et al.* employed an electrophoretic deposition (EPD) method to deposit $ZnCo_2O_4$ on a Ni substrate as an electrocatalyst for the OER, and the effects of electrophoresis variables, including the deposition time and the applied voltages, were investigated¹⁴⁵. A longer deposition time will prepare a compact and homogeneous surface at a low applied potential (10 V), and it will also lead to better electrocatalytic properties. The $ZnCo_2O_4$ electrode prepared at 10 V for 5 min has the best electrocatalytic properties, with an overpotential of 203 mV at 100 mA cm^{-2} . As shown in Fig. 14a, b, Zheng *et al.*¹⁴⁶ reported a new type of cauliflower-like $NiCo_2O_4$ (CF- $NiCo_2O_4$) film that was coelectrodeposited with silica for the OER. Benefiting from the improved intrinsic catalytic activity and increased surface area, this CF- $NiCo_2O_4$ film is Co enriched at the top surface and not only has low onset OER potential and large current density but also possesses excellent durability (Fig. 14c). Gupta *et al.*¹⁴⁷ synthesized a type of multifunctional $CoFe_2O_4$ spinel by ultrafast one-step electrodeposition on foamed nickel and carbon cloth and used it as a water splitting catalyst and supercapacitor, respectively. Electrodeposited $CoFe_2O_4$ on NF shows a low overpotential of 270 mV and a Tafel slope of 31 mV dec^{-1} , indicating a higher conductivity for electrodeposition compared to dip-coated $CoFe_2O_4$ with enhanced device performance.

5.2.3 Perovskite oxides

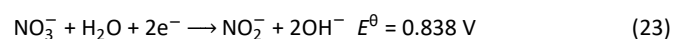
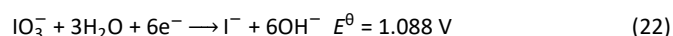
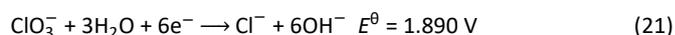
The general formula for perovskite oxides can be described as ABO_3 , where A is a rare-earth or alkaline-earth metal and B is a transition metal. They have been widely investigated as promising transition metal-based electrocatalysts for energy conversion and storage¹⁴⁸. In principle, perovskite oxides can be expressed as $A^2+B^4+O_3$, $A^3+B^3+O_3$, or other types. Benefiting from their highly tunable metal combination and composition, unique 3d electronic structures and high stability, perovskite oxides show outstanding catalytic activities for the OER¹⁴⁹. Zeng's group fabricated an adhesive $LaCrO_3$ perovskite coating on stainless steel by cathodic electrodeposition of a La-rich La-Cr coating composed of external La/Cr oxides or hydroxides and inner La-Cr from an aqueous citrate solution, followed by heat treatment in air¹⁵⁰. With the optimized pH value of 2.7 at the optimized current density of 1 mA cm^{-2} , a more uniform and compact La-Cr coating was obtained in the solution. The La and

Cr deposits changed from their metallic states to hydroxides during electrodeposition. During heat treatment, the Cr from the substrate diffused outward to react with the as-prepared La-Cr layer to form $LaCrO_3$. As illustrated in Fig. 14d, Zhang and coworkers proposed a preoxidation coupled electrodeposition strategy in which Co^{2+} was preoxidized to Co^{3+} through the cobalt Fenton reaction in an aqueous solution, whereas the reductive Ni framework was well maintained during the sequential annealing under a nonoxidative atmosphere¹⁵¹. The in situ-generated Co^{3+} was inherited into oxidized perovskites deposited on 3D NF (Fig. 14e, f), rendering monolithic perovskite electrocatalysts. The as-synthesized NF/oLCFO-Ar exhibited remarkable OER performance with an ultralow overpotential of 350 mV at 10 mA cm^{-2} (Fig. 14g), a very small Tafel slope of 59 mV dec^{-1} , and superb stability in 0.10 M KOH. They inaugurated a unique strategy for in situ hybridizations of the oxidative active phase with a reductive framework, affording superb reactivity of perovskite electrocatalysts for efficient water oxidation.

5.3 Transition-metal hydroxides

The transition metal-based hydroxide electrocatalysts dominated by the first transition metals (Fe, Co, Ni, *etc.*) are a group of important OER electrocatalysts that have aroused great interest in recent years^{22,152,153}. In this section, we briefly classify and introduce transition metal hydroxide electrocatalysts according to the following three representative groups: hydroxide, LDH, and oxyhydroxide.

Different from the direct electrodeposition of metals and metal oxides, metal hydroxides can be deposited on the cathode by two-step electroplating. First, due to the reduction of solute, numerous OH^- ions are generated near the surface of the cathode. Then, under the action of an electric field force, the metal ions in the solution move to the cathode and precipitate with OH^- in the form of hydroxide. The key is to improve the surface pH value of the working electrode. The following oxygen-containing anion reduction reactions are usually accepted to form hydroxide ions³¹.



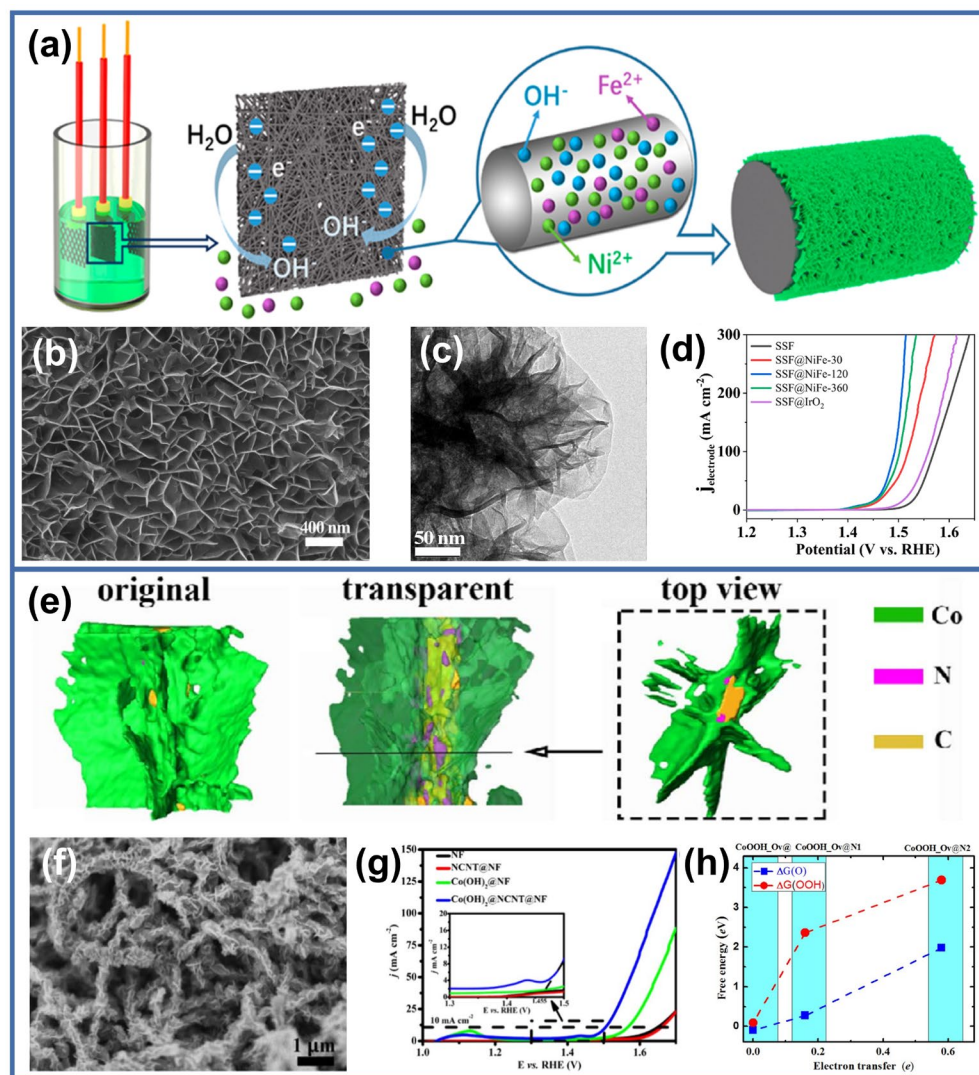


Fig. 16 (a) Schematic diagram of the electrodeposition process, (b) SEM and (c) TEM images of SSF@NiFe-120. (d) Geometric LSV curves of SSF, SSF@NiFe-30, SSF@NiFe-120, SSF@NiFe-360, and SSF@IrO₂ for O₂ evolution in 1 M KOH at a scan rate of 5 mV s⁻¹ with 85% iR compensation¹⁵⁴. Copyright 2020, American Chemical Society. (e) 3D reconstruction characterization of the Co(OH)₂ nanosheets on N-doped CNTs. (f) SEM image of Co(OH)₂ nanosheets on NCNTs. (g) Linear sweep voltammetry curves of the Co(OH)₂@NCNTs@NF electrode and their counterparts for the OER in 1 M KOH solution at 2 mV s⁻¹. (h) The relationship between an electron transfer in the heterostructure and $\Delta G(O)$ (blue square) and $\Delta G(OOH)$ (red round) for CoOOH@, CoOOH@N, and CoOOH@N₂¹⁵⁵. Copyright 2018, Elsevier.

For most metals, the standard potentials of the above three reactions are higher than those of metal cationic reduction. According to the Pourbaix diagram of nickel shown in Fig. 15a, the appropriate applied potential and pH of the electrolyte can be selected to control the deposition type¹². When an aqueous solution of chlorate is used as the deposition electrolyte, hydroxyl groups are generated by reducing chlorate and then increasing the pH near the surface of the cathode. Nickel hydroxide is formed in the potential range of 0–1.23 V, which effectively avoids the negative effect of oxygen evolution (hydroxyl consumption) and Ni²⁺ reduction to metal form. Similarly, for electrolytes containing iodate or nitrate, nickel hydroxide will be formed in the applied potential ranges of 0–1.09 V and 0–0.84 V, respectively. Therefore, cathodic reduction increases the local pH value near the electrode and drives the deposition of metal hydroxide in a kinetic way. In some cases, metal

oxides will be formed when hydroxides are further dehydrated or oxidized in air (Fig. 15b). It is worth noting that cathodic electrosynthesis is also beneficial to the coprecipitation of bimetallic or polymetallic hydroxides. Cathodic electrodeposition is a general and effective method for preparing different metal hydroxides on various conductive substrates.

5.3.1 Hydroxides

The typical transition metal hydroxides used as OER electrocatalysts are Ni(OH)₂, Co(OH)₂, and Ni_xFe_{1-x}(OH)₂. Sun *et al.*¹⁵⁴ reported the synthesis of an efficient bifunctional electrocatalytic electrode of nanoporous nickel-iron hydroxides coupled with a small amount of Ni/Fe metal based on stainless steel fiber felt (SSF) *via* a simple electrodeposition method (Fig. 16a). The as-prepared catalysis electrode can significantly improve the overall water splitting

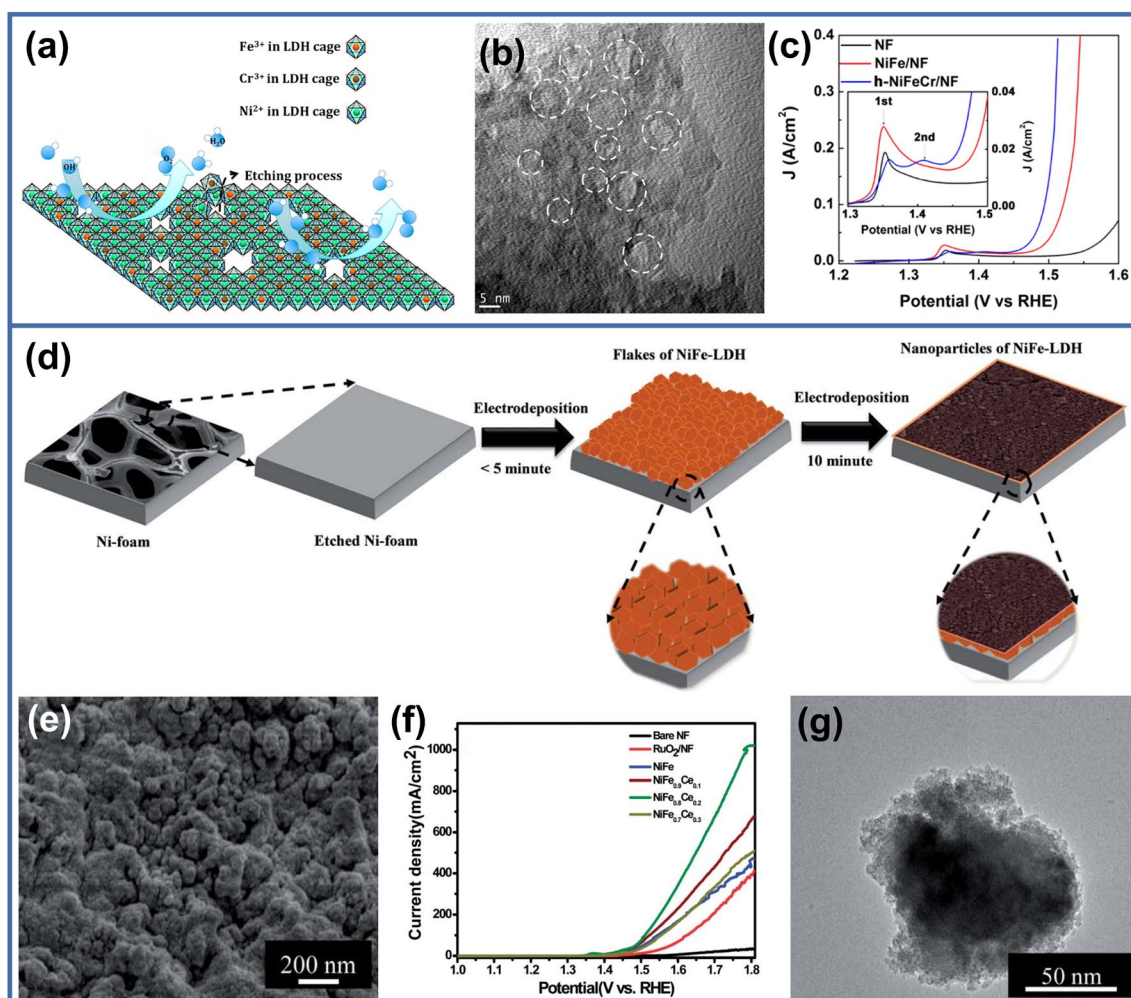


Fig. 17 (a) Schematic diagram of NiFeCr hydroxide nanosheets with holes. (b) HRTEM of h-NiFeCr/NF. Many holes with diameters of approximately 5 nm were formed on the nanosheets. (c) LSV curves of h-NiFeCr/NF, benchmark NiFe/NF, and NF at 5 mV s^{-1} with 95% iR compensation¹⁶⁰. Copyright 2017, American Chemical Society. (d) Schematic illustration of the electrodeposition of NiFe-based electrocatalysts on NF. (e) FE-SEM images of NiFe_{0.8}Ce_{0.2}. (f) Polarization curves of NiFeCe with various element ratios. (g) TEM images of NiFe_{0.8}Ce_{0.2}³⁵. Copyright 2020, The Royal Society of Chemistry.

performance. The SSF gaps are filled with Ni-Fe-OH composites, and the conductivity is improved by simultaneously generating Ni/Fe metal through electrodeposition (Fig. 16b, c). The as-synthesized electrode exhibits excellent electrocatalytic performance toward the OER, requiring an overpotential of only 210 mV at 10 mA cm^{-2} in 1 M KOH (Fig. 16d). Electrocatalysis studies show that the enhancement of water splitting activity may be caused by the synergistic action between the NiFe(OH)_x nanosheets and SSF substrate, which benefits the chemisorption of oxygen- and hydrogen-containing intermediates. Liu's group developed a two-step method to prepare a 3D Co(OH)₂@NCNTs@NF porous material through chemical vapor deposition and electrodeposition combined with the first-principles calculations (Fig. 16e, f)¹⁵⁵. Benefiting from the characteristics of ultrathin, microporous α -Co(OH)₂ and its derivatives, 3D Co(OH)₂@NCNTs@NF exhibits remarkable OER performance with an overpotential of 270 mV at 10 mA cm^{-2} in 1 M KOH for the OER (Fig. 16g). The first-principles calculations reveal that N doping is not only able to effectively enhance the interaction between the substrate and active material (CoOOH) but can also modulate the electronic

structure of CoOOH to speed up O₂ release during the OER (Fig. 16h). Zhang *et al.*¹⁵⁶ reported a strategy for the direct electrodeposition of cerium-doped nickel hydroxide nanosheets on carbon fiber paper. X-ray photoelectron spectroscopy analysis showed a strong electronic interaction between Ni(OH)₂ and CeO₂, which makes a great contribution to the OER enhancement.

5.3.2 Layered double hydroxide

Co/Ni-based LDH catalysts are a group of promising OER electrocatalysts due to their highly adjustable structures and compositions, unique physical-chemical properties, and excellent catalytic performance^{157,158}. Increasing the number of active sites is the most direct and effective strategy to improve the catalytic activity of a series of reactions, including OER^{38,159}.

As shown in Fig. 17a, by introducing chromium into a nickel-iron LDH, Zhao's group fabricated a nickel iron chromium hydroxide nanomesh catalyst on an NF substrate via electrodeposition followed by partial etching of chromium¹⁶⁰. The electrodeposited chromium acts as a sacrificial template to introduce holes in the LDH to enhance the

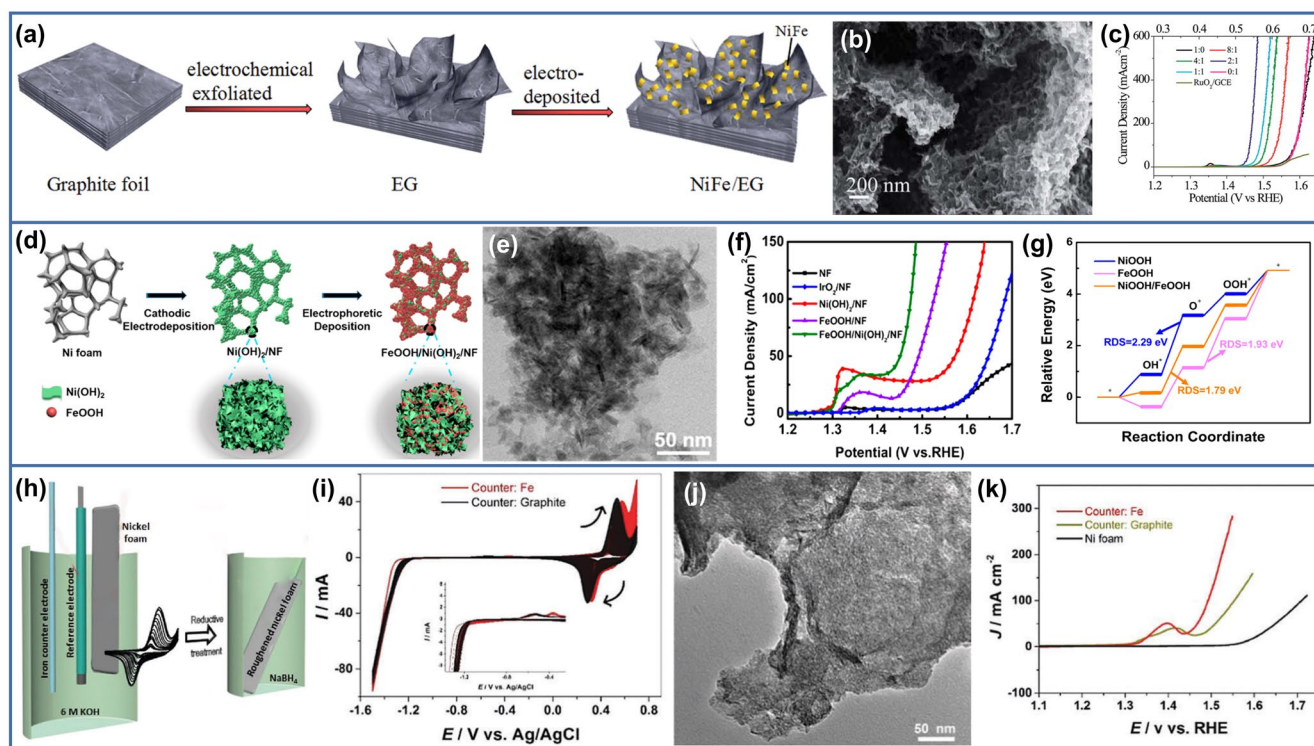


Fig. 18 (a) The fabrication process of the NiFe/EG electrode. (b) SEM image of NiFe(oxy)hydroxide on an EG substrate. (c) iR-corrected LSV curves of the NiFe/EG-1.2 V electrodes prepared from mixed nitrate precursors with different Ni/Fe ratios¹⁶³. Copyright 2017, The Royal Society of Chemistry. (d) Schematic illustration of the construction of FeOOH/Ni(OH)₂ on NF through cathodic electrodeposition of Ni(OH)₂ and subsequent electrophoretic deposition of FeOOH. (e) TEM image of FeOOH/Ni(OH)₂ composites. (f) Polarization curves after iR correction in comparison to pure NF and IrO₂/NF. (g) Calculated free energy diagram of the OER process on the surfaces of NiOOH (001), FeOOH (001), and NiOOH/FeOOH (001)¹⁶⁴. Copyright 2019, American Chemical Society. (h) Schematic of the preparation steps of oxygen vacancy-rich NiFe-OOH on an NF substrate. (i) Voltammograms of Ni in 6 M KOH at 25 °C and a scan rate of 200 mV s⁻¹ with a graphite and Fe counter electrode, respectively. (j) TEM images of the nanostructured Ni-Fe oxyhydroxide formed on NF roughened by an iron counter electrode. (k) Polarization curves of the different electrodes at a scan rate of 5 mV s⁻¹ and 90% iR compensation in 1 M KOH¹⁶⁵. Copyright 2017, The Royal Society of Chemistry.

electrochemically active surface area, and the remaining chromium synergistically tunes the electronic structure of the composite (Fig. 17b). The obtained electrode shows extraordinary performance for the OER with an overpotential of 255 mV to achieve a high current density of 100 mA cm⁻², outperforming the benchmark NiFe hydroxide composite electrode in alkaline media (Fig. 17c). Seo *et al.*³⁵ synthesized an efficient Ce-doped NiFe-LDH electrocatalyst directly on an NF substrate at room temperature *via* electrodeposition (Fig. 17d). A well-connected nanosheet array forming a 3D network on the substrate provided a large electrochemical surface area with abundant catalytically active sites (Fig. 17e). Ce doping in the NiFe-LDH electrocatalyst was vital to promoting its catalytic performance for the OER, and the optimized cerium-doped NiFe-LDH catalyst needs only 175 mV overpotential at 10 mA cm⁻² in 1 M KOH (Fig. 17f). The enhanced electrochemical performance of Ce-doped NiFe-LDH is mainly attributed to its unique 3D network, which increases the electrochemical specific surface area (Fig. 17g) and the abundant catalytic active sites produced by Ce doping. Our group fabricated an amorphous D-NiFeAl-LDH electrocatalyst with defect sites on NF *via* electrodeposition followed by alkali etching⁹¹. The D-NiFeAl-LDH electrocatalyst exhibited remarkable OER catalytic activity with a small overpotential of 262

mV at 10 mA cm⁻² and a low Tafel slope of 41.67 mV dec⁻¹ in 1 M KOH, which is even better than most of the reported NiFe-LDH electrocatalysts. The accelerated OER kinetics was mainly due to the introduction of iron and nickel defects in the D-NiFeAl-LDH nanosheets, which effectively adjusted the surface electronic structure and improved the electrocatalytic performance of the OER.

5.3.3 Oxyhydroxides

Numerous studies have reported that the structures of hydroxides and oxides are transformed into oxyhydroxides during the OER process¹⁶¹. Therefore, the synthesis and application of earth-rich hydroxide electrocatalysts have aroused great interest. The active sites of the OER are usually related to high valence (or oxidized) cations, such as Fe³⁺, Fe⁴⁺, Co³⁺, Co⁴⁺, and Mn³⁺, rather than their divalent cations. High valence cations can serve as electron acceptors to digest the generated electrons, thus promoting the reaction to the product site (Mⁿ⁺¹⁺ + e⁻ → Mⁿ⁺).

Low-cost transition metals, such as NiFe oxides/hydroxides, are considered one of the most efficient catalysts for the OER in alkaline media, but due to the lack of direct evidence for the proposed active sites during the catalytic processes, the detailed mechanisms are still unclear. Zhao *et al.*¹⁶² showed a NiFe (oxy)hydroxide catalyst doped with a third metal Cr prepared by facile electrodeposition to achieve

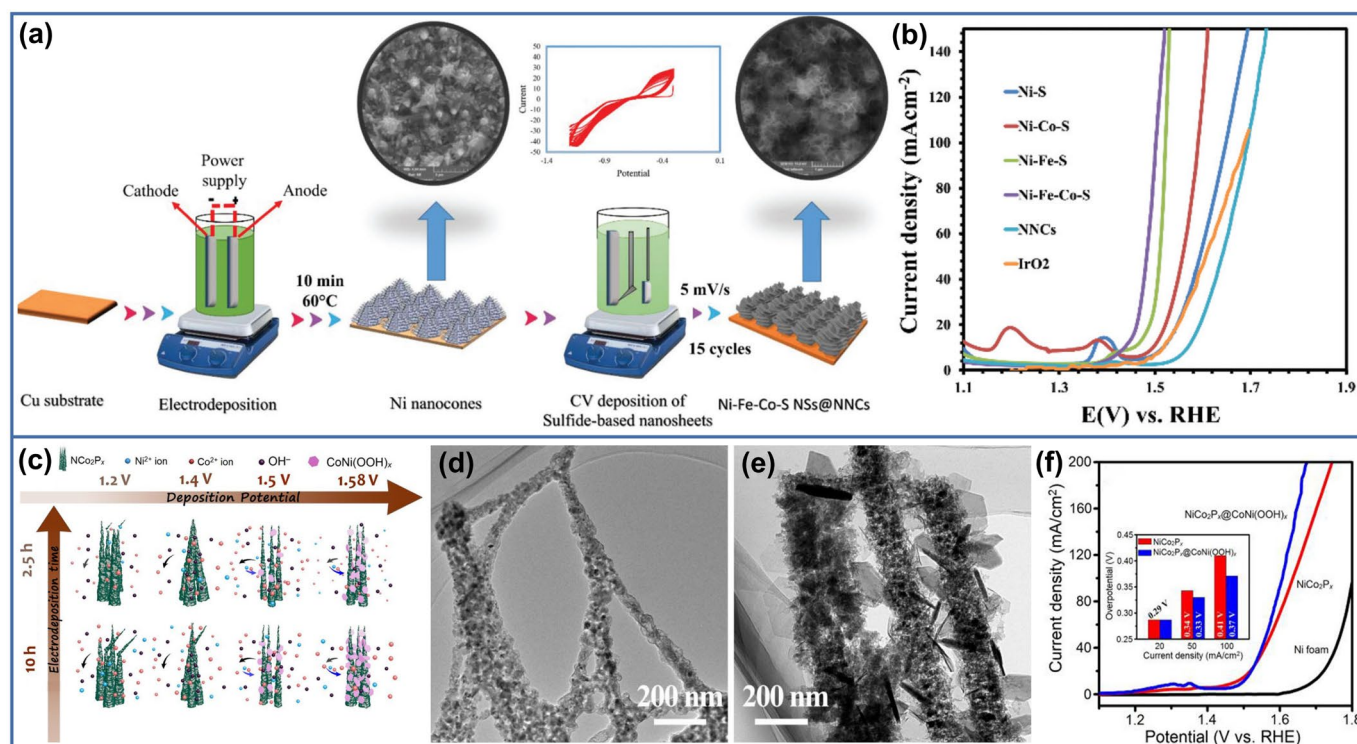


Fig. 19 (a) Schematic illustration showing the sulfide-based nanosheet fabrication stage. (b) LSV curves of different sulfide-based electrodes in 1.0 M KOH solution with a scan rate of 1 mV s⁻¹.³⁴ Copyright 2019, The Royal Society of Chemistry. (c) Schematic illustration of the proposed evolution process for the structural reconstitution of NiCo₂P_x NWs during anodic oxidation. Typical TEM images of (d) NiCo₂P_x NWs and (e) hierarchical NiCo₂P_x@CoNi(OOH)_x NWs. (f) 95% iR-compensated OER LSV curves for NiCo₂P_x NWs, hierarchical NiCo₂P_x@CoNi(OOH)_x NWs and NF in 1.0 M KOH (at a scan rate of 2 mV s⁻¹).¹⁷⁵ Copyright 2017, Elsevier.

further enhanced activity for the OER. They employed Operando Raman and X-ray absorption spectroscopy (XAS) characterization to investigate the formation of active intermediates and M-O bonds on active sites during the OER process. The shorter Fe-O in the Fe-substituted- β -NiOOH intermediate is observed as OER active sites for the NiFe (oxy)hydroxide host catalyst. A Cr, Fe-substituted- β -NiOOH intermediate is detected in the enhanced NiFeCr (oxy)hydroxide catalyst where Cr is oxidized into the 6+ valence state with optimal Cr-O bonds, adding new active sites to boost the OER. DFT calculations support the operando spectroscopic observations and reveal that the overpotential is lower at the Cr⁶⁺ sites in the NiFeCr oxyhydroxide intermediate than at the Fe³⁺ sites in the NiFe oxyhydroxide intermediate. Their study demonstrates a strategy for designing highly active OER catalysts by introducing high valence metals into oxides/hydroxides to further enhance the kinetics of water oxidation.

As shown in Fig. 18a, Liu's group developed a scalable electrodeposition route to fabricate amorphous nickel-iron (oxy)hydroxide nanosheets directly onto a 3D partially exfoliated graphite foil electrode¹⁶³. The integrated electrode combines the high OER catalytic activity of NiFe-based materials and the excellent electric conductivity of the carbon substrate, while its hierarchical structure guarantees facile ion transport and gaseous product (O₂) diffusion (Fig. 18b). The electronic structure of the Ni catalytic center, which is critical in determining the catalytic activity, can be controlled through Fe incorporation and/or tuning the electrodeposition

potential window. The optimal electrode exhibits outstanding OER catalytic performance with a low overpotential of 214 mV at 10 mA cm⁻² in 1 M KOH and a Tafel slope of 21 mV dec⁻¹. Xu and coworkers demonstrated a stepwise electrochemical construction of a crystalline α -FeOOH/ β -Ni(OH)₂ composite structure supported on NF through cathodic electrodeposition of β -Ni(OH)₂ nanosheets followed by electrophoretic deposition of α -FeOOH nanoparticles (Fig. 18d)¹⁶⁴. Taking advantage of the synergistic effect of Ni and Fe as well as the formed interface (Fig. 18e), this composite structure exhibits high activity for the OER process in 1 M KOH and provides an extremely low overpotential of 207 mV at 40 mA cm⁻² and a Tafel slope of 70 mV dec⁻¹, which is superior to most reported (oxy)hydroxide-based OER electrocatalysts (Fig. 18f). Moreover, the DFT calculations verify that the synergistic interface effect between the real active sites NiOOH and FeOOH can facilitate the OER process (Fig. 18g). Zhao *et al.*¹⁶⁵ reported a facile cyclic voltammetry strategy for attaining the autologous growth of a highly integrated and efficient NiFe-OOH catalyst for the OER *via* electrochemical roughening of NF substrates in 6 M KOH by employing an iron rod counter electrode (Fig. 18h, i). Benefiting from the electrochemical roughening accompanied by in situ doping of Fe, a nanostructured Ni surface with low interfacial electrical resistance and surface area that is 25 times larger was obtained (Fig. 18j). Electrochemical characterization illustrated that the fabricated NiFe-OOH catalysts exhibit an extremely low OER onset overpotential of 190 mV and a Tafel slope of merely 48.1 mV dec⁻¹ in 1 M KOH (Fig. 18k).

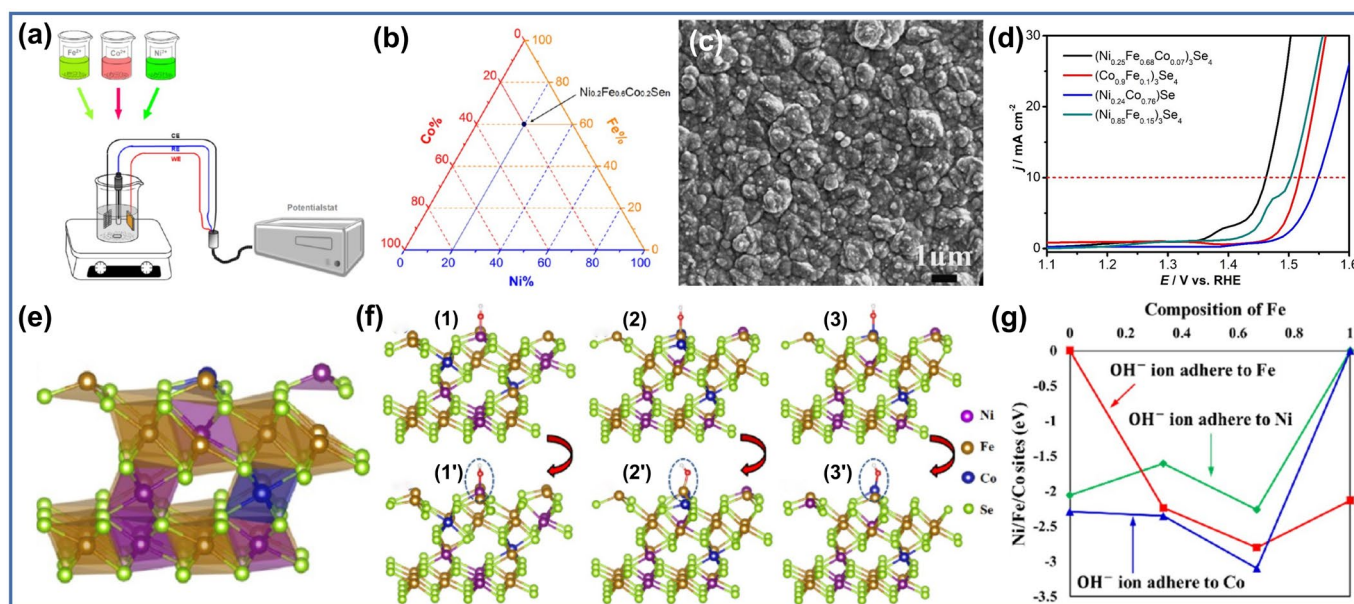


Fig. 20 (a) Schematic illustration of combinatorial electrodeposition. (b) Ternary phase diagram for exploring the compositions of the mixed-metal selenide films. (c) SEM image of the $(\text{Ni}_{0.25}\text{Fe}_{0.68}\text{Co}_{0.07})_3\text{Se}_4$ film. (d) Linear sweep voltammetry (LSV) measurements for selected catalysts in an N_2 -saturated 0.3 M KOH solution at a scan rate of 0.01 V s^{-1} . (e) Crystal structures of $2 \times 2 \times 2$ supercells of $(\text{Ni}_{0.25}\text{Fe}_{0.68}\text{Co}_{0.07})_3\text{Se}_4$. (f) Representatives of the original (1–3) and the corresponding relaxed (1'–3') crystal structures of $(\text{Ni}_{0.25}\text{Fe}_{0.68}\text{Co}_{0.07})_3\text{Se}_4$ supercells with OH^- placed above the active Ni, Fe, and Co sites on the (001) free surfaces. (g) Adsorption energy of OH^- ions to different active sites of Ni, Fe, and Co as a function of the composition of Fe¹⁸⁰. Copyright 2018, American Chemical Society.

Furthermore, a NaBH_4 reductive treatment was also used to create more surface defects on NiFe-OOH, resulting in further enhanced catalyst conductivity and a further decrease in the Tafel slope to 34.7 mV dec^{-1} . The electrode even demonstrated prolonged electrochemical and mechanical stability at high current densities in industrial 30 wt% KOH solutions.

5.4 Sulfides

Metal sulfides are considered excellent electrocatalysts because of their higher electrocatalytic activity, good electrical conductivity, convenient preparation, and low cost^{166–168}. Metal sulfides tend to have better catalytic properties than oxides or hydroxides since most sulfides have excellent electronic conductivity^{169,170}.

Chai's group synthesized ternary mixed metal Ni-Co-Fe sulfides based on 3D NF ($\text{NiCoFeS}/\text{NF}$) via a facile electrodeposition-solvothermal process¹⁶⁶. First, a uniform film of Co-Fe oxides was electrodeposited on the surface of the 3D skeleton of NF (CoFe/NF). Second, ethanol solvothermal sulfurization was employed to convert CoFe/NF to ternary mixed metal sulfides ($\text{NiCoFeS}/\text{NF}$). The XRD analysis confirms that ternary NiCoFeS is composed of mixed phases, including NiS, Ni_3S_2 , and Co_3S_4 phases, but no Fe sulfide phase, implying an amorphous state of Fe sulfides. The OER measurements indicate the excellent performance of $\text{NiCoFeS}/\text{NF}$, providing low overpotentials of 40 and 160 mV to drive 10 and 100 mA cm^{-2} in 1.0 M KOH, respectively. As shown in Fig. 19a, Shanmugam *et al.* fabricated Ni-Co-Fe-S ultrathin nanosheets through two-step electrodeposition³⁴. First, nickel nanocones (NNCs) were formed using electrochemical deposition; then, Ni-Co-Fe-S was obtained by directly depositing on the surface of the nanocones using the CV method. Due to the hierarchical structure of Ni-Fe-Co-S nanosheets,

not only was a highly active surface area formed, but the electron transfer and mass transfer were also enhanced. This structure also led to the faster release of oxygen bubbles from the surface. Thus, Ni-Co-Fe-S exhibits remarkable OER performance with an overpotential of 207 mV at 10 mA cm^{-2} in 1 M KOH (Fig. 19b).

5.5 Phosphides

Phosphides have been widely developed as advanced OER catalysts owing to their good electrical conductivity and inherent metal properties^{171,172}. It is worth noting that the real catalytic species of transition metal phosphide is the loose amorphous oxide layer produced during oxidation^{173,174}. Furthermore, the internal metal phosphide also plays the role of charge collection, resulting in the rapid diffusion/transfer of the charge⁷³.

Gaining insight into the structural evolution of transition-metal phosphides during anodic oxidation is important to understand their OER mechanism and then design high-efficiency transition metal-based catalysts. Zhao *et al.*¹⁷⁵ employed NiCo_2P_x nanowires (NWs) vertically grown on NF as the target to explore the in situ morphology and chemical component reconstitution during anodic oxidation. The major factors leading to the transformation from NiCo_2P_x to hierarchical $\text{NiCo}_2\text{P}_x@\text{CoNi}(\text{OOH})_x$ NWs are the following two competitive reactions: the dissolution of NiCo_2P_x NWs and the oxidative redeposition of dissolved Co^{2+} and Ni^{2+} ions, which is based primarily on the anodic bias applied to NiCo_2P_x NWs (Fig. 19c). The anodic deposition and rearrangement of metal ions on the surface of the NiCo_2P_x NW can be controlled by modulating the balance of the pH value on the surface of the NiCo_2P_x NW and the competitive reactions mentioned above, which can be immediately converted into $\text{CoNi}(\text{OH})_x$. Consequently, regular hexagonal $\text{CoNi}(\text{OOH})_x$

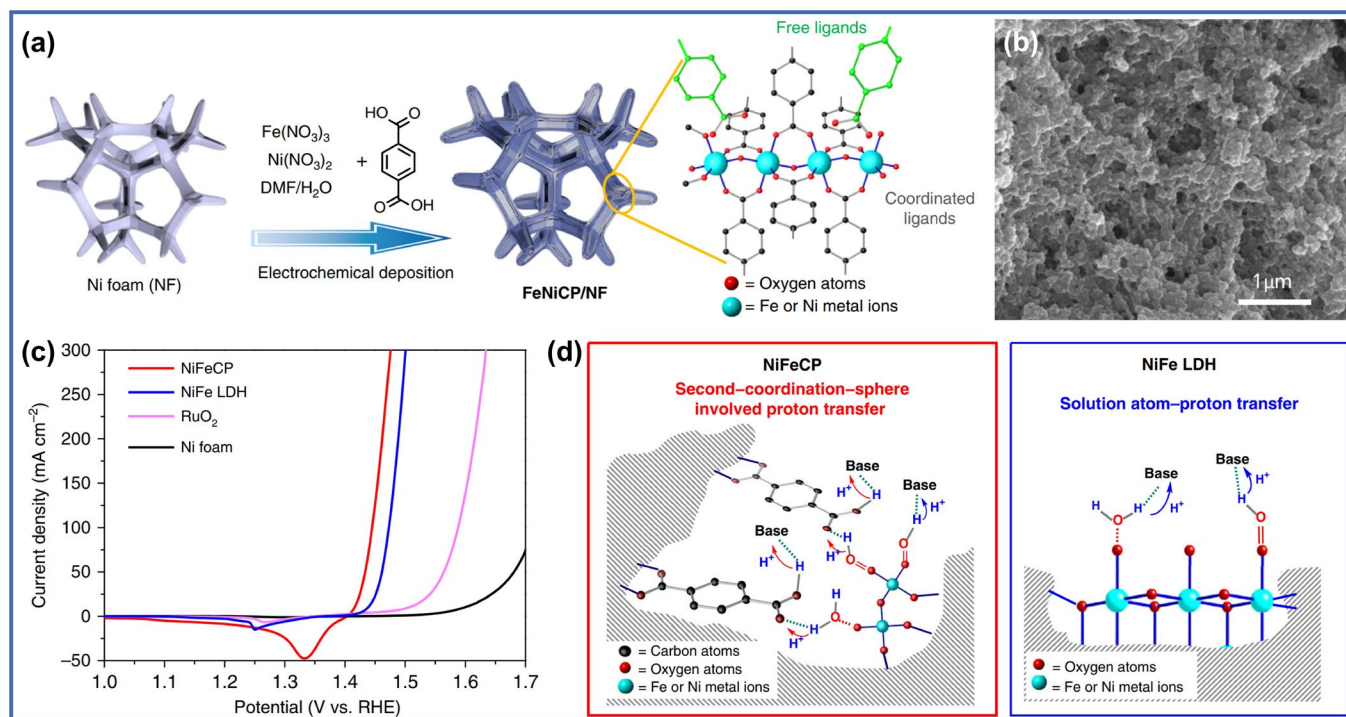


Fig. 21 (a) Schematic illustration of the fabrication procedure of the Ni-Fe coordination polymer prepared via an in situ electrochemical deposition method on an NF as a working electrode (NiFeCP/NF). (b) SEM images of NiFeCP/NF. (c) Linear sweep voltammetry (LSV) curves of NiFeCP/NF, NiFe LDH/NF, RuO_2 /NF, and NF. (d) Schematic illustration of the proposed proton transfer processes: second coordination sphere-involved proton transfer for NiFeCP (left) and APT for NiFe LDH (right)¹⁸³. Copyright 2019, Springer Nature.

nanosheets grew around the NiCo_2P_x NW (Fig. 19d, e). Owing to the active catalytic sites on the surface of $\text{NiCo}_2\text{P}_x@x\text{CoNi}(\text{OOH})_x$ and sufficient electrical conductivity, the obtained $\text{NiCo}_2\text{P}_x@x\text{CoNi}(\text{OOH})_x$ arrays exhibit good OER activity, rapid kinetic processes, high energy conversion efficiency, and especially excellent durability (Fig. 19f). Li *et al.*¹⁷² constructed CoP on a porous carbon membrane with different P contents modified in the presence of various NaH_2PO_2 concentrations in the electrolyte *via* electrodeposition. When the NaH_2PO_2 concentration is approximately 0.6 M, CoP-0.6/C presents malformed octahedral particles decorated on the nanofibers of a carbon membrane coated with CoP films. Benefiting from the large electrochemically active surface area and strong coupling between CoP films and the carbon membrane, CoP-0.6/C requires an overpotential of 250 mV for the OER to deliver 10 mA cm^{-2} with relatively stable durability. Hu's group prepared Janus Ni_2P nanoparticles *via* electrodeposition, and the experimental results indicate that the nanoparticles have high OER activity, which is attributed to the core-shell structure of $\text{Ni}_2\text{P}/\text{NiO}_x$ that the material adopts under catalytic conditions¹⁰⁵. Phosphorus introduces a part of the positive charge into the active metal centers, which leads to an increase in catalytic activity. In addition, the P in Ni_2P chemically supports the outermost active $\text{Ni}(\text{OH})_x$ layer and improves the stability of the catalyst.

5.6 Selenides

In various transition-metal selenides, selenium has highly metallic properties, a large relative radius, and low ionization energy; thus, the catalysts formed by metal selenides have unique intrinsic catalytic activity^{106,176,177}. Transition metal selenides show better

catalytic efficiency than oxides, which is due to their lower anion electronegativity and higher covalency in the lattice¹⁷⁸.

Shahrahi *et al.*¹⁷⁸ report a pulse potential electrodeposition method (PPE) as a fast and one-step route for the production of effective and binder-free NiSe nanostructures on NF. By controlling the pulse frequency, the electrocatalytic activity of prepared electrodes with various structures for the OER in alkaline solution was investigated. The results revealed that increasing the pulse frequency created an electrode with a lower surface area, followed by decreasing the electrocatalytic performance. The superior electrocatalytic activity and stability of S-0.01 compared to those of NiSe catalysts prepared by constant potential deposition and other synthesis methods are attributed to its 3D dual structure, large active surface area, no binder, and high adhesion between the coating and substrate. Chun's group reported the growth of nickel-cobalt-selenide (NiCoSe_2) nanosheets over 3D NF *via* a facile and scalable electrodeposition method¹⁷⁹. Benefiting from the presence of multiple catalytically active centers, a high electrochemically active surface area, and synergistic coupling effects between the NiCoSe_2 nanoparticles and NF support, the resulting NiCoSe_2 /NF electrode exhibits enhanced electrocatalytic performance for the OER with excellent stability. Element doping is an important route in electronic structure engineering that can highly enhance the conductivity of materials and the number of active sites. As illustrated in Fig. 20a, b, Nath *et al.*¹⁶⁹ investigated quaternary mixed-metal selenide compositions incorporating Ni-Fe-Co through combinatorial electrodeposition by exploring the ternary phase diagram of Ni-Fe-Co systems. The OER electrocatalytic activities of quaternary and ternary mixed metal

selenides were measured, and the variation trend of catalytic activities with the composition of the catalysts was systematically investigated. Specifically, increasing the Co and Fe concentrations in the Ni selenide matrix progressively improves the catalytic efficiency. Through this phase-space exploration, a very promising composition of $(\text{Ni}_{0.25}\text{Fe}_{0.68}\text{Co}_{0.07})_3\text{Se}_4$ as an OER electrocatalyst was found (Fig. 20c), which shows a low onset overpotential of 180 mV and an overpotential of 230 mV to reach a current density of 10 mA cm^{-2} in N_2 -saturated 0.3 M KOH (Fig. 20d). Electrochemical studies, along with the estimation of the hydroxyl adsorption energy of the surface revealed that the enhancement in catalytic activity can be partially due to the facilitated charge transfer at the electrode-electrolyte interface, as well as the charge transfer within the catalyst film (Fig. 20e–g). This research opens up a new avenue for investigating other mixed-metal selenide combinations and provides opportunities to understand the effect of each transition-metal ion (along with the d electron occupancy) on the catalyst's performance¹⁸⁰.

5.7 Other transition-metal compounds

Electrodeposition has occasionally been employed to synthesize polyanionic compounds. These materials typically exhibit higher OER catalytic activities than their corresponding oxides due to the different chemical environments created by substituting oxygen near the redox sites, which enhanced the electrical conductivity or led to crystal structures favorable for fast ion diffusion. Zhou's group used a simple electrodeposition strategy to fabricate amorphous cobalt phosphosulfide electrocatalysts on NF as efficient bifunctional electrodes for water splitting¹⁸¹. Benefiting from the introduction of phosphorus and sulfur, the quantities of precursor sites are increased, and the electronic state around cobalt is reconstructed, providing more active phases and increasing the electron transport efficiency. The electrochemical measurement results reveal that the as-prepared Co-P-S electrodes require overpotentials as low as 283 mV to achieve 10 mA cm^{-2} for the OER in 1.0 M KOH. Tafel slopes and electrochemical impedance spectroscopy further illustrate favorable kinetics during electrolysis. Kim *et al.*¹⁸² synthesized porous iron-nickel hydroxyphosphate and iron-cobalt hydroxyphosphate electrodes as bifunctional electrocatalysts for water splitting *via* a one-step electrodeposition method. The measurement results indicate that the as-prepared $\text{FeNi}(\text{PO}_4)(\text{OH})/\text{NF}$ and $\text{FeCo}(\text{PO}_4)(\text{OH})/\text{NF}$ electrodes have porous morphologies, high electrical conductivity, and high specific surface areas, which promote the efficient electrocatalytic ability of the OER and HER in alkaline media.

Electrodeposition can also be used to prepare transition metal-based coordination polymers. Sun *et al.*¹⁸³ reported a binder-free Ni-Fe coordination polymer (NiFeCP) prepared *via* an in situ electrochemical deposition method on NF as a catalyst (NiFeCP/NF) for the OER (Fig. 21a). Negatively charged carboxylate ligands were simultaneously introduced into the NiFeCP composites in both coordinated and uncoordinated forms, with the former expected to stabilize the high valence states of the metal centers and the latter expected to serve as proton transfer relays in the second coordination sphere of the active site. Various characterization techniques showed that the coordinated and uncoordinated carboxylic acid groups in the membrane remained unchanged after electrolysis. As shown in Fig. 21b, the prepared NiFeCP/NF is a 3D

macroscopic film that uniformly covers the surface of the NF skeleton. NiFeCP/NF exhibits remarkable electrocatalytic OER activity with a low overpotential of 188 mV at 10 mA cm^{-2} in 1.0 KOH, with a small Tafel slope of 29 mV dec^{-1} and excellent stability (Fig. 21c). They also carried out a comprehensive study on the mechanism of NiFeCP and NiFe LDH benchmark OER catalysts. NiFeCP and NiFe LDH show pH-independent OER activities on the RHE scale, indicating that synergistic proton-coupled electron transfer (c-PET) plays an important catalytic role in the OER for both catalysts. APT measurements show a smaller external base impact from the electrolyte on NiFeCP than that of NiFe LDH (Fig. 21d). All the experimental results reveal that the uncoordinated carboxylates can be used as proton transfer relays near the catalytic centers of NiFeCP. Such proton transfer relays can significantly improve the OER activity of the catalyst *via* the c-PET pathway. This interesting discovery may provide a new perspective for the design and synthesis of more advanced heterogeneous catalysts, further improve the catalytic activity through second-coordination sphere

Table 1 OER performance of transition-metal-based electrocatalysts.

Catalysts	Electrolytes	Substrates	Electrochemical synthesis technology	Structural design	Overpotential@10 mA cm ⁻² (mV)	Tafel slope (mV dec ⁻¹)	Stability time@10 mA cm ⁻²
CoNP cluster ¹⁰¹	1 M NaOH	Graphite sheet	Electrodeposition	Nano-clusters	350	76	12 h
NiFe NNA ⁹²	1 M KOH	Ni sheet	Electrodeposition, template	Nanotube arrays	236	45	24 h
Ni _{0.8} Fe _{0.2} ¹⁰¹	1 M KOH	Stainless steel mesh	Hydrothermal-electrodeposition	Mesoporous film of nanosheets	206	64	55 h
Doped MnO ₂ ¹⁴⁴	1 M KOH	Carbon fiber paper	Electrodeposition	Nanosheets	390	104	27.8 h
Ni _x Fe _{3-x} O ₄ /Ni ¹¹⁷	1 M KOH	Ni foam	Electrodeposition	Nanosheet arrays	218	45	200 h
CoFeWO _x ¹⁸⁴	1 M KOH	Ni foam	Electrodeposition	Nanoplates	231	32	120 h
CuO@Co ₃ O ₄ ⁷⁴	1 M KOH	Carbon paper	Electrochemical treatment, calcination, Electrodeposition	Nanowire@ nanosheets	258	72	12 h
NF/oLCFO-Ar ¹⁵¹	0.1 M KOH	Ni foam	Electrodeposition, calcination	Cubic nanoparticles	350	59	10000 s
h-NiFeCr/NF ¹⁶⁰	1 M KOH	Ni foam	Electrodeposition, CV-treatment	Holey nanosheets	255	29	40000 s
CoFe@NiFe/NF ⁹⁰	1 M KOH	Ni foam	Hydrothermal, electrodeposition	Nanosheet arrays	190	46	30 h
CoFe/NF ²⁰	1 M KOH	Ni foam	Electrodeposition	Nanosheets	220	40	50 h
NiFe/NF ¹¹	1 M KOH	Ni foam	Electrodeposition	Nanosheets	200	28	>100 h
NiFe/EG ¹⁶³	1 M KOH	Graphite foil	Electrodeposition	Nanofilm	214	21	100 h
CoNi/CoFe ₂ O ₄ /NF ¹¹⁸	1 M KOH	Ni foam	Hydrothermal, pyrolysis, electrodeposition	Nanosheets@ flowers	230	45	48 h
Ni:FeOOH/NGF ¹	1 M KOH	N-doped graphite foam	Electrodeposition	Nanosheets	214	36	60 h
CoNi-OOH ¹⁸⁵	1 M KOH	Ti sheet	Electrodeposition	Nanosheets	279	62	60 h
NiFe-OOH ¹⁶⁵	1 M KOH	Ni foam	CV-treatment	Nanofilm	190	48	24 h
Co(OH) ₂ @NCNTs@NF ¹⁵⁵	1 M KOH	Ni foam	Chemical vapor deposition, electrodeposition	Nanosheets@ nanotubes	270	72	600 h
Ni ₃ S ₂ NSs/NF ¹⁰⁰	1 M KOH	Ni foam	Hydrothermal-electrodeposition	Nanosheets with mesoporous	223	61	240 h
NiCoFe-S NSs@NNCs ³⁴	1 M KOH	Cu substrate	Electrodeposition, CV-deposition	Nanosheets@ nanocones	207	63	10 h
NiFe/(Ni,Fe) ₃ S ₂ ¹²⁵	1 M KOH	NiFe layer	Electrodeposition, template, sulfuration	Nanowires arrays	264@50 mA cm ⁻²	41	–
NiCoFe-S/NF ¹⁶⁶	1 M KOH	Ni foam	Electrodeposition-solvothermal	Nano-clusters	40	128	–
HP Ni-P ¹⁸⁶	1 M KOH	Ni plate	Electrodeposition, H ₂ template	Porous film	323@100 mA cm ⁻²	44	10 h

NiCuP ⁸⁴	1 M KOH	Cu foil	Electrodeposition	Porous nanofilm	307	43	30 h
Ni-Fe-P/NF ¹⁰⁸	1 M KOH	Ni foam	Electrodeposition	Holey nanospheres	156	69	>36 h
CuO-FR@CoP ¹⁸⁷	1 M KOH	Cu foam	Etching, calcination, Electrodeposition	Nanosheets and nanorods	290@50 mA cm ⁻²	56	>30 h
NiSe ¹⁷⁸	1 M KOH	Ni foam	Electrodeposition	Nanosheets	306@100 mA cm ⁻²	61	–
Fe-CoSe ₂ NF ¹⁷⁶	1 M KOH	Ni foam	Electrodeposition	Nanosheets	220	36	20 h
NiCoSe ₂ /NF ¹⁷⁹	1 M KOH	Ni foam	Electrodeposition	Nanoparticles	183	88	50 h
(Co _{0.21} Ni _{0.25} Cu _{0.54}) ₃ Se ₂ ¹⁰⁶	1 M KOH	Au-coated glass	Electrodeposition	Nanofilm	272	53	12 h
Co-S-P ¹⁸¹	1 M KOH	Ni foam	Electrodeposition	Stacked microspheres.	283	61	10 h
FeNi(PO ₄)(OH)/NF ¹⁸²	1 M KOH	Ni foam	Electrodeposition	Nanosheets	220	43	24 h
NiCoFe-PS/NF ⁹⁹	1 M KOH	Ni foam	Hydrothermal-electrodeposition	Mesoporous nanorods	195	40	200 h
NiFeCP/NF ¹⁸³	1 M KOH	Ni foam	Electrodeposition	Nanofilm	188	29	17 h
NiFe-60/Co ₃ O ₄ @NF ¹⁸⁸	1 M KOH	Ni foam	Hydrothermal, pyrolysis, electrodeposition	Core-shell nanowire array	221@100 mA cm ⁻²	35	24 h
NiFeOOH ¹⁸⁹	1 M KOH	Stainless steel paper	Electrodeposition	Nanoparticle	308@50 mA cm ⁻²	50	>500 h
LC-CoOOH Nas ¹⁹⁰	1 M KOH	Carbon fiber cloth	Electrodeposition, in-situ anodic oxidation	Nanosheet arrays	294	71	24 h
Fe-Doped β-Ni(OH) ₂ ¹⁹¹	1 M KOH	Ni foam	Hydrothermal, CV-activation	Nanosheets	219	53	–
Ni ₂ P–CuP ₂ ¹⁹²	1 M KOH	Ni foam	Electrodeposition, phosphorization	Nanoflower	140@20 mA cm ⁻²	42	240 h@500 mA cm ⁻²
NiFe-OOH@Ni ₃ Nb ¹⁹³	1 M KOH	3D-printed Inconel 718	3D plating, electrochemical activation	Porous nanosheets	159	28	>50 h@1500 mA cm ⁻²
NiFe LDH/NiS ¹⁹⁴	1 M KOH	Ni foam	Chemical-corrosion, electrodeposition	Nanosheet arrays	325@1000 mA cm ⁻²	60	>24 h@400 mA cm ⁻²
Ce-m-Ni(OH) ₂ @NiSe ₂ ¹⁹⁵	1 M KOH	Ni foam	Electrodeposition, solvent thermal	Nanoflowers@nanoparticles	158	27	20 h@50 mA cm ⁻²
EO Mo-/Co-N-C/ Cu ¹⁹⁶	1 M KOH	Nanoporous Cu	Electrodeposition, coordination, pyrolysis	Nanosheets	261	58	–
Co ₄ N-CeO ₂ /GP ¹⁹⁷	1 M KOH	Graphite plate	Electrodeposition, nitridation	Porous nanosheet	239	37	50 h@500 mA cm ⁻²
V-CoP@a-CeO ₂ NRA ¹⁹⁸	1 M KOH	Carbon cloth	Hydrothermal, phosphorization, electrodeposition	Nanorod arrays	225	58	40 h@20 mA cm ⁻²
Fe-CoP/Ni(OH) ₂ ¹⁹⁹	1 M KOH	Ni foam	Hydrothermal, phosphorization, electrodeposition	Nanosheets@nanowires	206	32	–
Co(OH) ₂ /NiMo CA@CC ²⁰⁰	1 M KOH	Carbon cloth	Electrodeposition, template	Macroporous array	259	72	–

V-Ni ₂ P/NF-AC ²⁰¹	1 M KOH	Ni foam	Hydrothermal, phosphorization, CV-treatment	Nanosheet arrays	221	66	20 h@50 mA cm ⁻²
CoCuFeMoOOH@Cu ₂₀₂	1 M KOH	Cu foil	Hydrothermal, electrochemical reconstruction	Cross-linked nanosheets	199	49	72
FeNi-LDH/CoP ²⁰³	1 M KOH	Carbon cloth	Electrodeposition, phosphorization	Nanosheet arrays	231@20 mA cm ⁻²	34	~18.5 h
NiCe@NiFe ²⁰⁴	1 M KOH	Ni foam	Electrodeposition	Nanoparticles@nanolayer	254@100 mA cm ⁻²	60	20h@1000 mA cm ⁻²
NiFe-LDH/Ni(OH) ₂ ²⁰⁵	1 M KOH	Ni foam	Electrodeposition	Nanoparticles@nanosheets	370@700 mA cm ⁻²	126	–
Ni@NiFe LDH ²⁰⁶	1 M KOH	Ni foam	Chemical reduction, Electrodeposition	Nanochains@nanosheets	218	66	24 h
δ-FeOOH/Ni ₃ S ₂ ²⁰⁷	1 M KOH	Ni foam	Electrodeposition, solvent thermal	Nanosheets	187	66	24 h@20 mA cm ⁻²
CLDH/CP/CF ²⁰⁸	1 M KOH	Cu foil	Anodication, electrodeposition, phosphorization	Nanosheets@nanowire arrays	220	34	–

engineering, and form a foundation for further research in the field of OER.

To date, various transition metal-based OER electrocatalysts for electrochemical synthesis have been evaluated with different OER performances (Table 1)

1,11,20,34,74,84,90,92,99-101,106,108,117,118,125,144,151,155,160,163,165,166,176,178,179,181-208. Since transition metal-based metals and alloys cannot survive when placed directly in harsh acidic and alkaline media, they usually need to be stabilized by hosts (such as carbon materials) or saturated with high electronegative elements. Transition-metal oxides and (oxy)hydroxides have been widely studied, and they exhibit considerable OER catalytic performance and are considered to be a group of promising candidates for OER electrocatalysts. In recent years, transition-metal sulfides and phosphides have attracted increasing research attention as OER electrocatalysts owing to their significantly improved electrocatalytic performance achieved through heteroatom doping. Furthermore, transition-metal selenides and polyanion compounds were also found to be capable of good OER catalytic performance in alkaline media. Notably, the OER operated in a strong oxidation environment containing numerous strong oxidation intermediates (e.g., O, OH, and OOH). Most transition-metal-based OER electrocatalysts, such as oxides, hydroxides, sulfides, phosphides, and selenides, are generally converted into oxyhydroxides on the surface of the catalysts during the OER process²⁰⁹, which is an in-situ surface reconstruction process. Electrocatalyst surface restructuring is induced by irreversible metal-site cation dissolution, resulting in in-situ formation of a TM oxyhydroxide shell on top of the parent electrocatalyst core that serves as the active surface for OER²¹⁰. For instance, Zhou *et al.*²¹¹ reported a simple self-sacrificing strategy to obtain high-performance OER electrocatalysts FeCo-oxyhydroxide. A trimetallic selenide heterostructure (FeCoMo-Se) consisting of FeSe₂, CoSe₂ and MoSe₂ is first one-step synthesized on a carbon cloth substrate. Under OER conditions, FeSe₂ and CoSe₂ are then in situ converted to FeCo-oxyhydroxide with the surface of FeCoMo-Se

reconstructed while retaining the nanosheet morphology of the heterostructure. Interestingly, MoSe₂ is self-sacrificially dissolved and hence leaves considerable space to increase the exposure of FeCo-oxyhydroxide to the electrolyte. Such an advantageous nanostructure endows the FeCoMo-Se-transformed electrocatalyst with excellent OER performance in an alkaline medium. Additionally, among all transition metal-based electrocatalysts, transition metal hydroxides (such as NiFe-based hydroxides) are perhaps the most active, stable, and promising OER electrocatalysts reported thus far. However, the real active centers for OERs are still controversial and need further exploration.

6. Conclusion and future prospects

Benefiting from the strong controllability and versatility of electrochemical synthesis technology, it is especially suitable for the fabrication of catalytic electrodes for water splitting devices. As a synthesis tool, it has unique advantages, challenges, and opportunities. In this review, we have shown that electrodeposition strategies can be employed to synthesize active materials consisting of low-dimensional, 2D and 3D nano/micron materials, including particles, tubes, lines, flowers, sheets, and hierarchical structures. Moreover, the latest progress in transition metal-based OER electrocatalysts is reviewed, including the classification of metals/alloys, oxides, hydroxides, sulfides, phosphides, selenides, and other transition metal compounds.

In summary, we enumerate the advantages of electrochemical synthesis technology in the preparation of nanostructured materials for oxygen evolution electrocatalysis as follows:

(1) The synthesis conditions are usually mild (for example, at room temperature) and do not require high temperature or ultrahigh pressure, which may destroy the structural integrity or change the composition of deposits and substrates. Moreover, electrochemical synthesis does not require advanced instruments and complex operations, making it highly attainable and readily achievable.

(2) Electrodeposition combines the active material directly and seamlessly with the current collector, which eliminates the need for polymer binders and conductive additives and simplifies electrode preparation.

(3) The composition and morphology of the deposited materials can be easily adjusted via electrodeposition by changing the deposition conditions, electrolyte composition, current density, voltage, and temperature.

(4) With electrodeposition, the catalytic active component can grow directly on the preset precursor substrate because it only deposits the material in an electrically conductive region. This deposition selectivity makes the electrodeposition method particularly suitable for the fabrication of hierarchical nanostructure composite electrodes.

(5) Electrochemically synthesized materials are usually poorly crystallized or completely amorphous. Amorphous and rich defects are beneficial for improving OER catalysis.

Despite the above advantages, electrochemical technology still faces many challenges and difficulties, including the following:

(1) Electrodeposition is divided into cathodic electrodeposition and anodic electrodeposition. During anodic electrodeposition, the surface of the substrate is oxidized due to strong electrochemical oxidation, and the subsequent active materials are attached to the substrate oxides under the action of an electric field force; thus, increasing the internal resistance of the electrode weakens the oxygen evolution catalytic activity.

(2) It is challenging to deposit multi-metal components using electrochemical preparation, as the reduction potentials of the metals are different. Some deposition that gravitates toward thermodynamically stable structures like layered double hydroxides or (some) perovskites are still possible. However, it is probably more difficult to get alloy or solid solution-like structure, unless post-treatment is done. Even so, it may be challenging because the island type growth makes long diffusion pathway required.

(3) Some active materials, such as metal sulfurs/phosphides, have not been widely synthesized by direct electrodeposition. A possible strategy is to convert metal oxides to the corresponding sulfurs/phosphides by sulfurization/phosphorization. However, this conversion usually involves high temperatures, and problems with thermally unstable compounds may occur.

(4) Controlling the uniformity of depositions is still a major obstacle for electrodeposition since a strong local electric field will lead to preferential deposition at the edge of the substrate.

Looking forward to the future, we believe that if the following problems are adequately addressed, the electrochemical performance and practicability of electrodeposited materials can be greatly enhanced:

(1) The reasonable design and realization of hierarchical structures with a one-step electrodeposition method are attractive for the preparation of oxygen evolution catalytic electrodes with high specific surface areas and high-quality activity. Alternatively, it is possible to explore the combination of electrodeposition strategies

with other established material synthesis methods to achieve more hierarchical structures.

(2) The development of substrates with high specific surface areas and remarkable conductivity is the preferred method to improve the ion diffusion kinetics of catalytic electrodes, but the deposition time and deposition rate must be strictly controlled to avoid pore blockage.

(3) Diversification of electrodeposition synthetic materials. For example, metal sulfurs/phosphides have gained increasing attention as a new generation of oxygen evolution catalytic materials, but unfortunately, without posttreatment, it is difficult to synthesize them by electrochemical methods. In addition to metal sulfurs/phosphides, electrodeposition can also grow 2D materials with electrocatalytic activity in addition to conductive organic materials, such as graphene, nitrogen-doped graphene, and porous polymers. There is no doubt that there is much room for the development of electrochemical synthesis technology.

(4) A deep understanding of the electrodeposition mechanism (including electrochemical nucleation and growth) will be of great benefit to promote the development of electrochemical synthesis. For example, understanding microscopic, complex and transient nucleation processes is essential to control the morphology and uniformity of sediments. Studies on the mechanism of electrodeposition, especially the recently developed electrodeposition mechanisms, are still very limited.

Finally, we would like to emphasize that electrochemical synthesis technology can never replace the existing material synthesis methods. In contrast, electrochemical strategies need to be combined with other technologies to promote the exploration and development of high oxygen evolution catalytic active electrodes.

Conflicts of interest

There are no conflicts to declare.

Acknowledgements

This work was supported by the Key Research and Development Program of Hubei, China (2020BHB013) and the JST-ERATO Yamauchi Materials Space-Tectonics Project (JPMJER2003). This work was also performed in part at the Queensland node of the Australian National Fabrication Facility (ANFF-Q), a company established under the National Collaborative Research Infrastructure Strategy to provide nano and microfabrication facilities for Australian researchers.

References

1. M. P. Suryawanshi, U. V. Ghorpade, S. W. Shin, U. P. Suryawanshi, E. Jo and J. H. Kim, *ACS Catal.*, 2019, **9**, 5025-5034.
2. L. Hu, M. Li, X. Wei, H. Wang, Y. Wu, J. Wen, W. Gu and C. Zhu, *Chem. Eng. J.*, 2020, **398**, 125605.
3. L. Han, S. Dong and E. Wang, *Adv. Mater.*, 2016, **28**, 9266-9291.
4. M. A. Khan, H. Zhao, W. Zou, Z. Chen, W. Cao, J. Fang, J. Xu,

- L. Zhang and J. Zhang, *Electrochem. Energy Rev.*, 2018, **1**, 483-530.
5. S. Ye, C. Ding, R. Chen, F. Fan, P. Fu, H. Yin, X. Wang, Z. Wang, P. Du and C. Li, *J. Am. Chem. Soc.*, 2018, **140**, 3250-3256.
6. Z. Cai, X. Bu, P. Wang, J. C. Ho, J. Yang and X. Wang, *J. Mater. Chem. A*, 2019, **7**, 5069-5089.
7. A. M. P. Sakita, R. D. Noce, E. Vallés and A. V. Benedetti, *Appl. Surf. Sci.*, 2018, **434**, 1153-1160.
8. C. Feng, M. B. Faheem, J. Fu, Y. Xiao, C. Li and Y. Li, *ACS Catal.*, 2020, **10**, 4019-4047.
9. Y. Liu, X. Liang, L. Gu, Y. Zhang, G. Li, X. Zou and J. Chen, *Nat. Commun.*, 2018, **9**, 2609.
10. H. Sun, Z. Yan, F. Liu, W. Xu, F. Cheng and J. Chen, *Adv. Mater.*, 2020, **32**, 1806326.
11. X. Lu and C. Zhao, *Nat. Commun.*, 2015, **6**, 6616.
12. Z. Yan, H. Sun, X. Chen, H. Liu, Y. Zhao, H. Li, W. Xie, F. Cheng and J. Chen, *Nat. Commun.*, 2018, **9**, 2373.
13. Z. Yan, H. Liu, Z. Hao, M. Yu, X. Chen and J. Chen, *Chem. Sci.*, 2020, **11**, 10614-10625.
14. M. Tahir, L. Pan, F. Idrees, X. Zhang, L. Wang, J. Zou and Z. L. Wang, *Nano Energy*, 2017, **37**, 136-157.
15. Q. Xiang, F. Li, W. Chen, Y. Ma, Y. Wu, X. Gu, Y. Qin, P. Tao, C. Song, W. Shang, H. Zhu, T. Deng and J. Wu, *ACS Energy Lett.*, 2018, **3**, 2357-2365.
16. I. Roger and M. D. Symes, *J. Mater. Chem. A*, 2016, **4**, 6724-6741.
17. J. Dong, Y. Lu, X. Tian, F. Q. Zhang, S. Chen, W. Yan, H. L. He, Y. Wang, Y. B. Zhang, Y. Qin, M. Sui, X. M. Zhang and X. Fan, *Small*, 2020, **16**, e2003824.
18. X. Han, C. Yu, S. Zhou, C. Zhao, H. Huang, J. Yang, Z. Liu, J. Zhao and J. Qiu, *Adv. Energy Mater.*, 2017, **7**, 1602148.
19. M. Khodabakhshi, S. Chen, T. Ye, H. Wu, L. Yang, W. Zhang and H. Chang, *ACS Appl. Mater. Interfaces*, 2020, **12**, 36268-36276.
20. P. Babar, A. Lokhande, H. H. Shin, B. Pawar, M. G. Gang, S. Pawar and J. H. Kim, *Small*, 2018, **14**, 1702568.
21. F. Song, L. Bai, A. Moysiadou, S. Lee, C. Hu, L. Liardet and X. Hu, *J. Am. Chem. Soc.*, 2018, **140**, 7748-7759.
22. K. Fan, H. Chen, Y. Ji, H. Huang, P. M. Claesson, Q. Daniel, B. Philippe, H. Rensmo, F. Li, Y. Luo and L. Sun, *Nat. Commun.*, 2016, **7**, 11981.
23. M. Qian, S. Cui, D. Jiang, L. Zhang and P. Du, *Adv. Mater.*, 2017, **29**, 1704075.
24. G. Jia, Y. Hu, Q. Qian, Y. Yao, S. Zhang, Z. Li and Z. Zou, *ACS Appl. Mater. Interfaces*, 2016, **8**, 14527-14534.
25. Z. Yang, J.-Y. Zhang, Z. Liu, Z. Li, L. Lv, X. Ao, Y. Tian, Y. Zhang, J. Jiang and C. Wang, *ACS Appl. Mater. Interfaces*, 2017, **9**, 40351-40359.
26. Q. Zhao, Z. Yan, C. Chen and J. Chen, *Chem. Rev.*, 2017, **117**, 10121-10211.
27. C. Li, X. Han, F. Cheng, Y. Hu, C. Chen and J. Chen, *Nat. Commun.*, 2015, **6**, 7345.
28. Y. L. Zhu, H. A. Tahini, Z. W. Hu, Z. G. Chen, W. Zhou, A. C. Komarek, Q. Lin, H. J. Lin, C. T. Chen, Y. J. Zhong, M. T. Fernandez-Diaz, S. C. Smith, H. T. Wang, M. L. Liu and Z. P. Shao, *Adv. Mater.*, 2020, **32**, 1905025.
29. J. Ji, L. L. Zhang, H. Ji, L. Yang and R. S. J. A. N. Ruoff, *ACS Nano*, 2013, **7**, 6237-6243.
30. D. Kang, T. W. Kim, S. R. Kubota, A. C. Cardiel, H. G. Cha and K. S. Choi, *Chem. Rev.*, 2015, **115**, 12839-12887.
31. G. H. A. Therese and P. V. Kamath, *Chem. Mater.*, 2000, **12**, 1195-1204.
- H. Lv, Q. Pan, Y. Song, X.-X. Liu and T. Liu, *Nano-Micro Lett.*, 2020, **12**, 118.
33. K. Zhang, Z. H. Yan and J. Chen, *Joule*, 2020, **4**, 10-11.
34. G. Barati Darband, M. Aliofkhaeizadeh, S. Hyun, A. Sabour Rouhaghdam and S. Shanmugam, *Nanoscale*, 2019, **11**, 16621-16634.
35. H. S. Jadhav, A. Roy, B. Z. Desalegan and J. G. Seo, *Sustain. Energy Fuels*, 2020, **4**, 312-323.
36. G. R. Li, H. Xu, X. F. Lu, J. X. Feng, Y. X. Tong and C. Y. Su, *Nanoscale*, 2013, **5**, 4056-4069.
37. J. Zhang, Q. Zhang and X. Feng, *Adv. Mater.*, 2019, **31**, e1808167.
38. Z. W. Seh, J. Kibsgaard, C. F. Dickens, I. B. Chorkendorff, J. K. Nørskov and T. F. Jaramillo, *Science*, 2017, **355**, eaad4998.
39. C. Hu, L. Zhang and J. Gong, *Energy Environ. Sci.*, 2019, **12**, 2620-2645.
40. N.-T. Suen, S.-F. Hung, Q. Quan, N. Zhang, Y.-J. Xu and H. M. Chen, *Chem. Soc. Rev.*, 2017, **46**, 337-365.
41. Z.-F. Huang, J. Song, Y. Du, S. Xi, S. Dou, J. M. V. Nsanzimana, C. Wang, Z. J. Xu and X. Wang, *Nat. Energy*, 2019, **4**, 329-338.
42. Y. Pan, X. Xu, Y. Zhong, L. Ge, Y. Chen, J.-P. M. Veder, D. Guan, R. O'Hayre, M. Li, G. Wang, H. Wang, W. Zhou and Z. Shao, *Nat. Commun.*, 2020, **11**, 2002.
43. R. A. Marcus, *Rev. Mod. Phys.*, 1993, **65**, 599-610.
44. R. A. Marcus, *J. Phys. Chem.*, 1968, **72**, 891-899.
45. Z. W. Seh, J. Kibsgaard, C. F. Dickens, I. Chorkendorff, J. K. Nørskov and T. F. Jaramillo, *Science*, 2017, **355**, eaad4998.
46. H. N. Nong, T. Reier, H.-S. Oh, M. Glieth, P. Paciok, T. H. T. Vu, D. Teschner, M. Heggen, V. Petkov, R. Schlögl, T. Jones and P. Strasser, *Nat. Catal.*, 2018, **1**, 841-851.
47. M. E. G. Lyons and M. P. Brandon, *J. Electroanal. Chem.*, 2010, **641**, 119-130.
48. J. T. Mefford, Z. Zhao, M. Bajdich and W. C. Chueh, *Energy Environ. Sci.*, 2020, **13**, 622-634.
49. P. E. Pearce, C. Yang, A. Iadecola, J. Rodriguez-Carvajal, G. Rousse, R. Dedryvère, A. M. Abakumov, D. Giaume, M. Deschamps, J.-M. Tarascon and A. Grimaud, *Chem. Mater.*, 2019, **31**, 5845-5855.
50. A. Grimaud, A. Demortière, M. Saubanière, W. Dachraoui, M. Duchamp, M.-L. Doublet and J.-M. Tarascon, *Nat. Energy*, 2016, **2**, 16189.
51. H. N. Nong, L. J. Falling, A. Bergmann, M. Klingenhof, H. P. Tran, C. Spöri, R. Mom, J. Timoshenko, G. Zichittella, A. Knop-Gericke, S. Piccinin, J. Pérez-Ramírez, B. R. Cuenya, R. Schlögl, P. Strasser, D. Teschner and T. E. Jones, *Nature*, 2020, **587**, 408-413.
52. T. Shinagawa, A. T. Garcia-Esparza and K. Takane, *Sci. Rep.*, 2015, **5**, 13801.
53. N. Yao, Z. Fan, R. Meng, H. Jia and W. Luo, *Chem. Eng. J.*, 2020, **408**, 127319.
54. J. O. Bockris and A. Reddy, *Modern Electrochemistry*, Plenum, New York, 1970.
55. R. Guidelli, R. G. Compton, J. M. Feliu, E. Gileadi, J. Lipkowski, W. Schmickler and S. Trasatti, *Pure and Applied Chemistry*, 2014, **86**, 245-258.
56. B. M. Jović, U. Č. Lačnjevac, V. D. Jović and N. V. Krstajić, *J. Electroanal. Chem.*, 2015, **754**, 100-108.
57. I. C. Man, H.-Y. Su, F. Calle-Vallejo, H. A. Hansen, J. I. Martínez, N. G. Inoglu, J. Kitchin, T. F. Jaramillo, J. K. Nørskov and J. Rossmeisl, *Chemcatchem.*, 2011, **3**, 1159-1165.
58. M. B. Kale, R. A. Borse, A. Goma Abdelkader Mohamed

- and Y. Wang, *Adv. Funct. Mater.*, 2021, **31**, 2101313.
59. Y. Chen, Z. Sun, J.-M. Wu, R. Jiang, P. Yang, Y. Gu, W. Liu, J. Wu and W. Wen, *Chem. Phys. Lett.*, 2020, **754**, 137734.
60. M. Xiong and D. G. Ivey, *Electrochim. Acta*, 2018, **260**, 872-881.
61. N. Elgrishi, K. J. Rountree, B. D. McCarthy, E. S. Rountree, T. T. Eisenhart and J. L. Dempsey, *J. Chem. Educ.*, 2017, **95**, 197-206.
62. E. Herrero, L. J. Buller and H. D. Abrun˜a, *Chem. Rev.*, 2001, **101**, 1897-1930.
63. M. Palomar-Pardavé, I. González and N. Batina, *J. Phys. Chem. B*, 2000, **104**, 3545-3555.
64. R. Salazar, C. Lévy-Clément and V. Ivanova, *Electrochim. Acta*, 2012, **78**, 547-556.
65. E. J. Podlaha, *Nano Lett.*, 2001, **1**, 413-416.
66. M. Ghaemi and L. Binder, *J. Power Sources*, 2002, **111**, 248-254.
67. L. Besra and M. Liu, *Prog. Mater. Sci.*, 2007, **52**, 1-61.
68. P. Sarkar and P. S. Nicholson, *J. Am. Ceram. Soc.*, 1996, **79**, 1987-2002.
69. Y. Liu, Y. Bai, Y. Han, Z. Yu, S. Zhang, G. Wang, J. Wei, Q. Wu and K. Sun, *ACS Appl. Mater. Interfaces*, 2017, **9**, 36917-36926.
70. X. Shang, Z. Z. Liu, J. Q. Zhang, B. Dong, Y. L. Zhou, J. F. Qin, L. Wang, Y. M. Chai and C. G. Liu, *ACS Appl. Mater. Interfaces*, 2018, **10**, 42217-42224.
71. L. Yu, H. Zhou, J. Sun, F. Qin, D. Luo, L. Xie, F. Yu, J. Bao, Y. Li, Y. Yu, S. Chen and Z. Ren, *Nano Energy*, 2017, **41**, 327-336.
72. P. C. Wang, L. Wan, Y. Q. Lin and B. G. Wang, *ChemSusChem*, 2019, **12**, 4038-4045.
73. X. Teng, J. Wang, L. Ji, W. Tang and Z. Chen, *ACS Sustainable Chem. Eng.*, 2017, **6**, 2069-2077.
74. X. Li, X. Du, X. Ma, Z. Wang, X. Hao, A. Abudula, A. Yoshida and G. Guan, *Electrochim. Acta*, 2017, **250**, 77-83.
75. R. Ji, F. Zhang, Y. Liu, Y. Pan, Z. Li, Z. Liu, S. Lu, Y. Wang, H. Dong, P. Liu, X. Wu and H. Jin, *Nanoscale*, 2019, **11**, 22734-22742.
76. Z. Zhao, H. Wu, H. He, X. Xu and Y. Jin, *Adv. Funct. Mater.*, 2014, **24**, 4698-4705.
77. X. Li, Y. Wang, J. Wang, Y. Da, J. Zhang, L. Li, C. Zhong, Y. Deng, X. Han and W. Hu, *Adv. Mater.*, 2020, **32**, e2003414.
78. X. Li, C. Li, A. Yoshida, X. Hao, Z. Zuo, Z. Wang, A. Abudula and G. Guan, *J. Mater. Chem. A*, 2017, **5**, 21740-21749.
79. B. Liu, S. Qu, Y. Kou, Z. Liu, X. Chen, Y. Wu, X. Han, Y. Deng, W. Hu and C. Zhong, *ACS Appl. Mater. Interfaces*, 2018, **10**, 30433-30440.
82. W. Yang, Q. Zhang, S. S. Siwal, Y. Hua and C. Xu, *Electrochim. Acta*, 2020, **361**, 137038.
81. Y. Wu, Y. Gao, H. He and P. Zhang, *Electrochim. Acta*, 2019, **301**, 39-46.
82. V. Torabinejad, M. Aliofkhaezraei, S. Assareh, M. H. Allahyarzadeh and A. S. Rouhaghdam, *J. Alloy. Compd.*, 2017, **691**, 841-859.
83. V. C. Kieling, *Surf. Coat. Tech.*, 1997, **96**, 135-139.
84. B. K. Kim, S.-K. Kim, S. K. Cho and J. J. Kim, *Appl. Catal. B-Environ.*, 2018, **237**, 409-415.
85. J. Vaes, J. Fransaer and J. P. Celis, *J. Electrochem. Soc.*, 2000, **147**, 3718-3724.
86. P. E. d. Jongh, D. Vanmaekelbergh and J. J. Kelly, *Chem. Mater.*, 1999, **11**, 3512-3517.
87. A. B. Velichenko, R. Amadelli, E. V. Gruzdeva, T. V. Luk'yanenko and F. I. Danilov, *J. Power Sources*, 2009, **191**, 103-110.
88. J. A. M. Oliveira, A. F. de Almeida, A. R. N. Campos, S. Prasad, J. J. N. Alves and R. A. C. de Santana, *J. Alloy. Compd.*, 2021, **853**, 157104.
89. S. Mitra, P. Poizot, A. Finke and J. M. Tarascon, *Adv. Funct. Mater.*, 2006, **16**, 2281-2287.
90. R. Yang, Y. Zhou, Y. Xing, D. Li, D. Jiang, M. Chen, W. Shi and S. Yuan, *Appl. Catal. B-Environ.*, 2019, **253**, 131-139.
91. H. Li, L. Zhang, S. Wang and J. Yu, *Int. J. Hydrogen Energy*, 2019, **44**, 28556-28565.
92. C. L. Huang, X. F. Chuah, C. T. Hsieh and S. Y. Lu, *ACS Appl. Mater. Interfaces*, 2019, **11**, 24096-24106.
93. M.-J. Deng, P.-J. Ho, C.-Z. Song, S.-A. Chen, J.-F. Lee, J.-M. Chen and K.-T. Lu, *Energy Environ. Sci.*, 2013, **6**, 2178-2185.
94. Y. S. Jeon, S. H. Kim, B. C. Park, D. Y. Nam and Y. K. Kim, *Chem. Commun.*, 2017, **53**, 1825-1828.
95. C. Xiao, Y. Li, X. Lu and C. Zhao, *Adv. Funct. Mater.*, 2016, **26**, 3515-3523.
96. C. Yuan, J. Li, L. Hou, X. Zhang, L. Shen and X. W. D. Lou, *Adv. Funct. Mater.*, 2012, **22**, 4592-4597.
97. L. Fan, P. Zhang, B. Zhang, Q. Daniel, B. J. J. Timmer, F. Zhang and L. Sun, *ACS Energy Lett.*, 2018, **3**, 2865-2874.
98. L. Yu, H. Zhou, J. Sun, F. Qin, F. Yu, J. Bao, Y. Yu, S. Chen and Z. Ren, *Energy Environ. Sci.*, 2017, **10**, 1820-1827.
99. M. Yao, H. Hu, B. Sun, N. Wang, W. Hu and S. Komarneni, *Small*, 2019, **15**, e1905201.
100. M. Yao, B. Sun, L. He, N. Wang, W. Hu and S. Komarneni, *ACS Sustainable Chem. Eng.*, 2019, **7**, 5430-5439.
101. M. Yao, N. Wang, W. Hu and S. Komarneni, *Appl. Catal. B-Environ.*, 2018, **233**, 226-233.
102. J. Duay, S. A. Sherrill, Z. Gui, E. Gillette and S. B. Lee, *ACS Nano*, 2013, **7**, 1200-1214.
103. W. Zhang, Y. Wu, J. Qi, M. Chen and R. Cao, *Adv. Energy Mater.*, 2017, **7**, 1602547.
104. Y. Liu, S. X. Guo, L. Ding, C. A. Ohlin, A. M. Bond and J. Zhang, *ACS Appl. Mater. Interfaces*, 2015, **7**, 16632-16644.
105. L.-A. Stern, L. Feng, F. Song and X. Hu, *Energy Environ. Sci.*, 2015, **8**, 2347-2351.
106. X. Cao, E. Johnson and M. Nath, *J. Mater. Chem. A*, 2019, **7**, 9877-9889.
107. M. Chen, S. Lu, X. Z. Fu and J. L. Luo, *Adv. Sci.*, 2020, **7**, 1903777.
108. L. Li, W. Huang, J. Lei, B. Shang, N. Li and F. Pan, *Appl. Surf. Sci.*, 2019, **479**, 540-547.
109. A. Renjith and V. Lakshminarayanan, *ACS Appl. Nano Mater.*, 2020, **3**, 2705-2712.
110. S. Yang, R. Du, Y. Yu, Z. Zhang and F. Wang, *Nano Energy*, 2020, **77**, 105057.
111. Y. Liu, D. Gokcen, U. Bertocci and T. P. Moffat, *Science*, 2012, **338**, 1327-1330.
112. P. Babar, A. Lokhande, V. Karade, B. Pawar, M. G. Gang, S. Pawar and J. H. Kim, *ACS Sustainable Chem. Eng.*, 2019, **7**, 10035-10043.
113. S. Cobo, J. Heidkamp, P.-A. Jacques, J. Fize, V. Fourmond, L. Guetaz, B. Jusselme, V. Ivanova, H. Dau, S. Palacin, M. Fontecave and V. Artero, *Nat. Mater.*, 2012, **11**, 802-807.
114. T. T. H. Hoang and A. A. Gewirth, *ACS Catal.*, 2016, **6**, 1159-1164.
115. T. Wang, X. Liu, Z. Yan, Y. Teng, R. Li, J. Zhang and T. Peng, *ACS Sustainable Chem. Eng.*, 2019, **8**, 1240-1251.
116. R. C. Rohit, A. D. Jagadale, S. K. Shinde, D. Y. Kim, V. S. Kumbhar and M. Nakayama, *J. Alloy. Compd.*, 2021, **863**,

- 158081.
117. D. Li, S. Liu, G. Ye, W. Zhu, K. Zhao, M. Luo and Z. He, *Green Chem.*, 2020, **22**, 1710-1719.
118. S. Li, S. Sirisomboonchai, A. Yoshida, X. An, X. Hao, A. Abudula and G. Guan, *J. Mater. Chem. A*, 2018, **6**, 19221-19230.
119. S. Shit, S. Bolar, N. C. Murmu and T. Kuila, *ACS Sustainable Chem. Eng.*, 2019, **7**, 18015-18026.
120. X. Yan, Y. Zhao, J. Biemolt, K. Zhao, P. C. M. Laan, X. Cao and N. Yan, *J. Mater. Chem. A*, 2020, **8**, 7626-7632.
121. S. Kim, C. Ahn, Y. Cho, G. Hyun, S. Jeon and J. H. Park, *Nano Energy*, 2018, **54**, 184-191.
122. K. Zhang, S. Deng, Y. Zhong, Y. Wang, J. Wu, X. Wang, X. Xia and J. Tu, *Chinese J. Catal.*, 2019, **40**, 1063-1069.
123. H. Zhang, X. Li, A. Haehnel, V. Naumann, C. Lin, S. Azimi, S. L. Schweizer, A. W. Maijenburg and R. B. Wehrspohn, *Adv. Funct. Mater.*, 2018, **28**, 1706847.
124. X.-D. Wang, H.-Y. Chen, Y.-F. Xu, J.-F. Liao, B.-X. Chen, H.-S. Rao, D.-B. Kuang and C.-Y. Su, *J. Mater. Chem. A*, 2017, **5**, 7191-7199.
125. C. T. Hsieh, X. F. Chuah, C. L. Huang, H. W. Lin, Y. A. Chen and S. Y. Lu, *Small Methods*, 2019, **3**, 1900234.
126. G. Wu, W. Chen, X. Zheng, D. He, Y. Luo, X. Wang, J. Yang, Y. Wu, W. Yan, Z. Zhuang, X. Hong and Y. Li, *Nano Energy*, 2017, **38**, 167-174.
127. M. S. Sander and H. Gao, *J. Am. Chem. Soc.*, 2005, **127**, 12158-12159.
128. R. Chen, H.-Y. Wang, J. Miao, H. Yang and B. Liu, *Nano Energy*, 2015, **11**, 333-340.
129. L.-K. Wu, W.-Y. Wu, J. Xia, H.-Z. Cao, G.-Y. Hou, Y.-P. Tang and G.-Q. Zheng, *Electrochim. Acta*, 2017, **254**, 337-347.
130. Y. Li, K. Dastafkan, Q. Sun, Y. Ma, X. Wang, X. Yang, Z. Wang and C. Zhao, *Electrochim. Acta*, 2021, **379**, 138042.
131. J. Jin, J. Xia, X. Qian, T. Wu, H. Ling, A. Hu, M. Li and T. Hang, *Electrochim. Acta*, 2019, **299**, 567-574.
132. C. Cheng, F. Zheng, C. Zhang, C. Du, Z. Fang, Z. Zhang and W. Chen, *J. Power Sources*, 2019, **427**, 184-193.
133. J. Zhou, L. Yu, Q. Zhou, C. Huang, Y. Zhang, B. Yu and Y. Yu, *Appl. Catal. B-Environ.*, 2021, **288**, 120002.
134. J. S. Kim, B. Kim, H. Kim and K. Kang, *Adv. Energy Mater.*, 2018, **8**, 1702774.
135. W. T. Hong, M. Risch, K. A. Stoerzinger, A. Grimaud, J. Suntivich and Y. Shao-Horn, *Energy Environ. Sci.*, 2015, **8**, 1404-1427.
136. R. Rajendiran, D. Chinnadurai, K. Chen, A. R. Selvaraj, K. Prabakar and O. L. Li, *ChemSusChem*, 2021, **14**, 1324-1335.
137. J. A. Koza, Z. He, A. S. Miller and J. A. Switzer, *Chem. Mater.*, 2012, **24**, 3567-3573.
138. M. Tortosa, F. J. Manjón, M. Mollar and B. Marí, *J. Phys. Chem Solids*, 2012, **73**, 1111-1115.
139. H. Li, Z. Chen, Q. Yu, W. Zhu and W. Cui, *J. Electrochem. Soc.*, 2017, **164**, H1064-H1071.
140. Z. L. Wang, R. Guo, L. X. Ding, Y. X. Tong and G. R. Li, *Sci. Rep.*, 2013, **3**, 1204.
141. Y. Wang, K. Takahashi, H. Shang and G. Cao, *J. Phys. Chem. B*, 2005, **109**, 3085-3088.
142. M.-I. Jamesh and X. Sun, *J. Power Sources*, 2018, **400**, 31-68.
143. Y. P. Zhu, C. Guo, Y. Zheng and S. Z. Qiao, *Acc. Chem. Res.*, 2017, **50**, 915-923.
144. Z. Ye, T. Li, G. Ma, Y. Dong and X. Zhou, *Adv. Funct. Mater.*, 2017, **27**, 1704083.
145. B. Chi, J. Li, X. Yang, H. Lin and N. Wang, *Electrochim. Acta*, 2005, **50**, 2059-2064.
146. L.-K. Wu, J. Xia, H.-Z. Cao, Y.-P. Tang, G.-Y. Hou and G.-Q. Zheng, *Int. J. Hydrogen Energy*, 2017, **42**, 10813-10825.
147. C. Zhang, S. Bhojate, C. Zhao, P. Kahol, N. Kostoglou, C. Mitterer, S. Hinder, M. Baker, G. Constantinides, K. Polychronopoulou, C. Rebholz and R. Gupta, *Catalysts*, 2019, **9**, 176.
148. G. Chen, W. Zhou, D. Guan, J. Sunarso, Y. Zhu, X. Hu, W. Zhang and Z. Shao, *Sci. Adv.*, 2017, **3**, e1603206.
149. Y. Zhu, W. Zhou and Z. Shao, *Small*, 2017, **13**, 1603793.
150. X. Zhang, P. You, M. Luo and C. Zeng, *J. Electrochem. Soc.*, 2016, **163**, D821-D828.
151. B. Q. Li, C. Tang, H. F. Wang, X. L. Zhu and Q. Zhang, *Sci. Adv.*, 2016, **2**, e1600495(140).
152. J. Jiang, F. Sun, S. Zhou, W. Hu, H. Zhang, J. Dong, Z. Jiang, J. Zhao, J. Li, W. Yan and M. Wang, *Nat. Commun.*, 2018, **9**, 2885.
153. F. Dionigi and P. Strasser, *Adv. Energy Mater.*, 2016, **6**, 1600621.
154. S. Zhu, G. Duan, C. Chang, Y. Chen, Y. Sun, Y. Tang, P. Wan and J. Pan, *ACS Sustainable Chem. Eng.*, 2020, **8**, 9885-9895.
155. P. Guo, J. Wu, X.-B. Li, J. Luo, W.-M. Lau, H. Liu, X.-L. Sun and L.-M. Liu, *Nano Energy*, 2018, **47**, 96-104.
156. G. Fang, J. Cai, Z. Huang and C. Zhang, *RSC Adv.*, 2019, **9**, 17891-17896.
157. L. Lv, Z. Yang, K. Chen, C. Wang and Y. Xiong, *Adv. Energy Mater.*, 2019, **9**, 1803358.
158. Y. Wang, D. Yan, S. El Hankari, Y. Zou and S. Wang, *Adv. Sci.*, 2018, **5**, 1800064.
159. P. Zhang, L. Li, D. Nordlund, H. Chen, L. Fan, B. Zhang, X. Sheng, Q. Daniel and L. Sun, *Nat. Commun.*, 2018, **9**, 381.
160. X. Bo, Y. Li, R. K. Hocking and C. Zhao, *ACS Appl. Mater. Interfaces*, 2017, **9**, 41239-41245.
161. M. S. Burke, L. J. Enman, A. S. Batchellor, S. Zou and S. W. Boettcher, *Chem. Mater.*, 2015, **27**, 7549-7558.
162. X. Bo, R. K. Hocking, S. Zhou, Y. Li, X. Chen, J. Zhuang, Y. Du and C. Zhao, *Energy Environ. Sci.*, 2020, **13**, 4225-4237.
163. Y.-J. Ye, N. Zhang and X.-X. Liu, *J. Mater. Chem. A*, 2017, **5**, 24208-24216.
164. S. Niu, Y. Sun, G. Sun, D. Rakov, Y. Li, Y. Ma, J. Chu and P. Xu, *ACS Appl. Energy Mater.*, 2019, **2**, 3927-3935.
165. M. Asnavandi and C. Zhao, *Mater. Chem. Front.*, 2017, **1**, 2541-2546.
166. X. Zhao, X. Shang, Y. Quan, B. Dong, G.-Q. Han, X. Li, Y.-R. Liu, Q. Chen, Y.-M. Chai and C.-G. Liu, *Electrochim. Acta*, 2017, **230**, 151-159.
167. Y. Luo, J. Qin, G. Yang, S. Luo, Z. Zhao, M. Chen and J. Ma, *Chem. Eng. J.*, 2021, **410**, 128394.
168. Z. Zang, X. Wang, X. Li, Q. Zhao, L. Li, X. Yang, X. Yu, X. Zhang and Z. Lu, *ACS Appl. Mater. Interfaces*, 2021, **13**, 9865-9874.
169. Y. Tang, T. Chen and S. Yu, *Chem. Commun.*, 2015, **51**, 9018-9021.
170. N. Cheng, Q. Liu, A. M. Asiri, W. Xing and X. Sun, *J. Mater. Chem. A*, 2015, **3**, 23207-23212.
171. J. Xing, H. Li, M. M.-C. Cheng, S. M. Geyer and K. Y. S. Ng, *J. Mater. Chem. A*, 2016, **4**, 13866-13873.
172. X. Li, X. Qian, Y. Xu, F. Duan, Q. Yu, J. Wang, L. Chen, Y. Dan and X. Cheng, *J. Alloy. Compd.*, 2020, **829**, 154535.
173. T. L. Wu, M. Y. Pi, D. K. Zhang and S. J. Chen, *J. Mater. Chem. A*, 2016, **4**, 14539-14544.
174. S. Jin, *ACS Energy Lett.*, 2017, **2**, 1937-1938.

175. X. Bai, Z. Ren, S. Du, H. Meng, J. Wu, Y. Xue, X. Zhao and H. Fu, *Sci. Bull.*, 2017, **62**, 1510-1518.
176. A. Zare, A. Bayat, E. Saievar-Iranizad and H. Naffakh-Moosavy, *J. Electroanal. Chem.*, 2020, **878**, 114595.
177. X. Xu, P. Du, Z. Chen and M. Huang, *J. Mater. Chem. A*, 2016, **4**, 10933-10939.
178. S. Esmailzadeh, T. Shahrabi, G. Barati Darband and Y. Yaghoubinezhad, *Electrochim. Acta*, 2020, **334**, 135549.
179. K. Akbar, J. H. Jeon, M. Kim, J. Jeong, Y. Yi and S.-H. Chun, *ACS Sustainable Chem. Eng.*, 2018, **6**, 7735-7742.
180. X. Cao, Y. Hong, N. Zhang, Q. Chen, J. Masud, M. A. Zaeem and M. Nath, *ACS Catal.*, 2018, **8**, 8273-8289.
181. F. Du, Y. Zhang, H. He, T. Li, G. Wen, Y. Zhou and Z. Zou, *J. Power Sources*, 2019, **431**, 182-188.
182. P. T. Babar, A. C. Lokhande, E. Jo, B. S. Pawar, M. G. Gang, S. M. Pawar and J. H. Kim, *J. Ind. Eng. Chem.*, 2019, **70**, 116-123.
183. W. Li, F. Li, H. Yang, X. Wu, P. Zhang, Y. Shan and L. Sun, *Nat. Commun.*, 2019, **10**, 5074.
184. J. Chen, H. Li, Z. Yu, C. Liu, Z. Yuan, C. Wang, S. Zhao, G. Henkelman, S. Li, L. Wei and Y. Chen, *Adv. Energy Mater.*, 2020, **10**, 2002593.
185. C. Yu, J. Lu, L. Luo, F. Xu, P. K. Shen, P. Tsiakaras and S. Yin, *Electrochim. Acta*, 2019, **301**, 449-457.
186. D. Song, D. Hong, Y. Kwon, H. Kim, J. Shin, H. M. Lee and E. Cho, *J. Mater. Chem. A*, 2020, **8**, 12069-12079.
187. Q. Zhou, T. Li, F. Guo and Y. Zheng, *ACS Sustainable Chem. Eng.*, 2018, **6**, 11303-11312.
188. J. Lv, L. Wang, R. Li, K. Zhang, D. Zhao, Y. Li, X. Li, X. Huang and G. Wang, *ACS Catal.*, 2021, **11**, 14338-14351.
189. J. E. Park, S. Park, M.-J. Kim, H. Shin, S. Y. Kang, Y.-H. Cho and Y.-E. Sung, *ACS Catal.*, 2022, **12**, 135-145.
190. S. Ye, J. Wang, J. Hu, Z. Chen, L. Zheng, Y. Fu, Y. Lei, X. Ren, C. He, Q. Zhang and J. Liu, *ACS Catal.*, 2021, **11**, 6104-6112.
191. T. Kou, S. Wang, J. L. Hauser, M. Chen, S. R. J. Oliver, Y. Ye, J. Guo and Y. Li, *ACS Energy Lett.*, 2019, **4**, 622-628.
192. S. Riyajuddin, K. Azmi, M. Pahuja, S. Kumar, T. Maruyama, C. Bera and K. Ghosh, *ACS Nano*, 2021, **15**, 5586-5599.
193. S. Chang, Y. Zhang, B. Zhang, X. Cao, L. Zhang, X. Huang, W. Lu, C. Y. A. Ong, S. Yuan, C. Li, Y. Huang, K. Zeng, L. Li, W. Yan and J. Ding, *Adv. Energy Mater.*, 2021, **11**, 2100968.
194. Q. Wen, K. Yang, D. Huang, G. Cheng, X. Ai, Y. Liu, J. Fang, H. Li, L. Yu and T. Zhai, *Adv. Energy Mater.*, 2021, **11**, 2102353.
195. S. F. Zai, X. Y. Gao, C. C. Yang and Q. Jiang, *Adv. Energy Mater.*, 2021, **11**, 2101266.
196. H. Shi, T.-Y. Dai, W.-B. Wan, Z. Wen, X.-Y. Lang and Q. Jiang, *Adv. Funct. Mater.*, 2021, **31**, 2102285.
197. H. Sun, C. Tian, G. Fan, J. Qi, Z. Liu, Z. Yan, F. Cheng, J. Chen, C.-P. Li and M. Du, *Adv. Funct. Mater.*, 2020, **30**, 1910596.
198. L. Yang, R. Liu and L. Jiao, *Adv. Funct. Mater.*, 2020, **30**, 1909618.
199. X. Yu, J. Zhao and M. Johnsson, *Adv. Funct. Mater.*, 2021, **31**, 2101578.
200. Q. Zhang, W. Xiao, W. H. Guo, Y. X. Yang, J. L. Lei, H. Q. Luo and N. B. Li, *Adv. Funct. Mater.*, 2021, **31**, 2102117.
201. T. Zhao, X. Shen, Y. Wang, R. K. Hocking, Y. Li, C. Rong, K. Dastafkan, Z. Su and C. Zhao, *Adv. Funct. Mater.*, 2021, **31**, 2100614.
202. L. Zhang, W. Cai and N. Bao, *Adv. Mater.*, 2021, **33**, 2100745.
203. K. He, T. T. Tsega, X. Liu, J. Zai, X.-H. Li, X. Liu, W. Li, N. Ali and X. Qian, *Angew. Chem. Int. Ed.*, 2019, **58**, 11903-11909.
204. G. Liu, M. Wang, Y. Wu, N. Li, F. Zhao, Q. Zhao and J. Li, *Appl. Catal. B-Environ.*, 2020, **260**, 118199.
205. N. S. Gultom, H. Abdullah, C.-N. Hsu and D.-H. Kuo, *Chem. Eng. J.*, 2021, **419**, 129608.
206. Z. Cai, X. Bu, P. Wang, W. Su, R. Wei, J. C. Ho, J. Yang and X. Wang, *J. Mater. Chem. A*, 2019, **7**, 21722-21729.
207. X. Ji, C. Cheng, Z. Zang, L. Li, X. Li, Y. Cheng, X. Yang, X. Yu, Z. Lu, X. Zhang and H. Liu, *J. Mater. Chem. A*, 2020, **8**, 21199-21207.
208. X. Xu, A. Cao, W. You, Z. Tao, L. Kang and J. Liu, *Small*, 2021, **17**, 2101725.
209. R. A. Marquez-Montes, K. Kawashima, Y. J. Son, J. A. Weeks, H. H. Sun, H. Celio, V. H. Ramos-Sánchez and C. B. Mullins, *J. Mater. Chem. A*, 2021, **9**, 7736-7749.
210. S. Samira, J. Hong, J. C. A. Camayang, K. Sun, A. S. Hoffman, S. R. Bare and E. Nikolla, *JACS Au*, 2021, **1**, 2224-2241.
211. Y.-J. Tang, Y. Wang and K. Zhou, *J. Mater. Chem. A*, 2020, **8**, 7925-7934.